Ollscoil na hEireann

National University of Ireland

Synthesis, Characterisation and Applications of Group IV Nanocrystals

A Thesis Presented to
The National University of Ireland
for the degree of
Doctor of Philosophy

by

Keith Linehan, B.Sc. M.Sc.

Supervised by Dr. Hugh Doyle

Tyndall National Institute

Tyndall National Institute
University College Cork
September 2014

Table of Contents

Declaration by Candidate:

I hereby certify that the work on this, my thesis is based on my own independent work, except where I have received help as stated in the acknowledgements and text.

All quotations and summary of the work of others have been acknowledged where appropriate.

Signature of candidate: _____

Date: _____

Abstract

Group IV materials such as silicon nanocrystals (Si NCs) and carbon quantum dots (CQDs) have received great attention as new functional materials with unique physical/chemical properties that are not found in the bulk material. This thesis reports the synthesis and characterisation of both types of nanocrystal and their application as fluorescence probes for the detection of metal ions.

In chapter 2, a simple method is described for the size controlled synthesis of Si NCs within inverse micelles having well defined core diameters ranging from 2 to 6 nm using inert atmospheric synthetic methods. In addition, ligands with different molecular structures were utilised to reduce inter-nanocrystal attraction forces and improve the stability of the NC dispersions in water and a variety of organic solvents. Regulation of the Si NCs size is achieved by variation of the surfactants and addition rates, resulting high quality NCs with standard deviations ($\sigma = \Delta d/d$) of less than 10 %. Large scale production of highly mondisperse Si NC was also successfully demonstrated.

In chapter 3, a simple solution phase synthesis of size monodisperse carbon quantum dots (CQDs) using a room temperature microemulsion strategy is demonstrated. The CQDs are synthesized in reverse micelles via the reduction of carbon tetrachloride using a hydride reducing agent. CQDs may be functionalised with covalently attached alkyl or amine monolayers, rendering the CQDs dispersible in wide range of polar or non-polar solvents. Regulation of the CQDs size was achieved by utilizing hydride reducing agents of different strengths. The CQDs possess a high photoluminescence quantum yield in the visible region and exhibit excellent photostability.

In chapter 4, a simple and rapid assay for detection of Fe^{3+} ions was developed, based on quenching of the strong blue-green Si NC photoluminescence. The detection method showed a high selectivity, with only Fe^{3+} resulting in strong quenching of the fluorescence signal. No quenching of the fluorescence signal was induced by Fe^{2+} ions, allowing for solution phase discrimination between the same ion in different charge states. The optimised sensor system showed a sensitive detection range from 25- 900 µM and a limit of detection of 20.8 µM.

Acknowledgements

First and foremost, I would like to express my sincere gratitude to my supervisor Dr. Hugh Doyle for giving me the opportunity to pursue a doctorate in Chemistry. I will be forever grateful for his expert supervision, support, guidance and encouragement throughout my PhD. I would like to thank the other members of the nanotechnology group Dr. Aidan Quinn, Dr. Alan O'Riordan, Dr Daniela lacopino, Dr. Mary Manning, Dr. Karen Dawson, Dr. Pierre Lovera and Dr. Michael Burke for their advice and suggestions during the preparation of this thesis.

I would also like to acknowledge my thesis committee members Prof Martyn Pemble, Dr. Georgios Fagas and Dr Michael Nolan for their advice, direction and suggestions during the thesis progress review meetings. Many thanks are also due to the past and present postgrads of the nanotechnology group, those whom I had the pleasure of working with and who provided advice (both technical and personal) as well as the frequent distractions from work. So thanks to; Darragh, John, Micki, Amelie, Ethel, Nicolas, Andrea, Daniel, Brenda, Brendan, Armelle, Seán, Colm, Alfonso, Alessio, Carola, Niamh, and Daniel Lordan. In particular, I would like to say a special thanks to Darragh Carolan for his great help, assistance and advice during my PhD.

I would like to thank Dr Shane O'Brien and Dr Sibu Padmanabhan for their collaborative assistance, Dr. Fathima Laffir (MSSI) for carrying out XPS measurements and Dr. Stephen Richards for carrying out TGA and DSC measurements.

As for my friends outside of Tyndall, I would like to say a special thanks to Graham, Richard and Mark for their fantastic company and fun throughout the course of my PhD. Finally, a special thank-you to my parents, family and girlfriend Denise for their continued support and encouragement throughout my PhD.

To Denise

“*To give anything less than your best, is to sacrifice the gift”*

Steve Prefontaine

Chapter 1

Introduction

1.1 General Introduction

In the last 20 years, the synthesis of quantum dots with sizes ranging from 2-20 nm has been intensively pursued, not only for their fundamental scientific interest, but also for their many electronic applications. Since the first reports in the late 1980s,[1] a wide range of semiconductor materials have been prepared in nanocrystal form. To date semiconductor quantum dots (QDs) such as II-VI, III-V, and IV-VI compounds have attracted a lot of attention because of their unique optoelectronic properties. These compounds possess strong absorption, size tunable photo-luminescence (PL) emission, high quantum yield (QY) and stability against photo bleaching.[2, 3] The methods of preparation, surface properties and fundamental physics of compound semiconductor quantum dots have extensively been explored.

More recently their application in solar cells,[4, 5] optoelectronics devices[6, 7] and as fluorescent labelling agents[8, 9] have been recognised and studied extensively, suggesting enormous potential for this class of material for a number of applications. Despite the numerous QD applications, one problem associated with traditional quantum dots is the use of heavy metals such as cadmium which is known to be toxic to biological systems.[10, 11] Safety issues have therefore hampered their development to some extent due to the current regulation on the use of heavy metals for commercial applications.[12] As a result, researchers have focused on searching for nanoparticles that have the outstanding properties of QDs and at the same time to not represent a toxicological issue.

Group IV materials such as silicon nanocrystals (Si NCs) and carbon quantum dots (CQDs) are one solution to this problem as they possess key features of traditional semiconductor with the additional benefit of their low toxicity. In recent years these materials have received a great deal of attention as a new functional material with unique physical/chemical properties that are not found in the bulk material. For instance, while bulk silicon is known to be a poor light emitter due to its indirect band gap, silicon nanocrystals have exhibited enhanced photo- and electro-luminescence properties due to quantum confinement effects. [9, 13-17] These properties can be readily tuned by manipulating the NC diameter and surface functionalisation. The level of control over the materials photophysical and optoelectronic properties that is possible

using solution-phase chemical synthetic routes allows for applications in chemical and biological sensors,[18, 19] and also to be fully exploited as effective building blocks for the fabrication of novel functional devices, such as light-emitting devices. [20-24] Silicon nanocrystals are also attractive for their lower toxicity and their compatibility with existing silicon based microelectronics.

1.2 Quantum Confinement in Semiconductor Nanocrystals

One of the characteristic properties of fluorescent quantum dots, in contrast with bulk materials, is the size dependence of the photophysical properties of the nanomaterial, which allows nanomaterial characteristics to be tuned simply by nanocrystal growth, according to the desirable end application. The mechanism of the size dependence of the luminescence properties of semiconductor QDs is well established. Quantum dots have dimensions of 1–100 nm and show distribution of electronic energy states between those of a discrete molecule and those of the bulk semiconductor, see Figure 1.1. Bulk semiconductors are characterized by band-gap energy, which corresponds to the minimum energy required to excite an electron from the ground-state-valence energy band into the vacant conduction energy band.

When a photon of sufficient energy is absorbed by the material, an electron is promoted from the valence band to the conductive band. As a result a hole in the valence band will form. The resulting positive hole will form a bound state with the excited negative electron by coulomb interaction and can be described in a similar way to the hydrogen-like bound state between the proton and the electron of the hydrogen atom. The annihilation of the exciton (e.g., by emission of a photon) is known as radiative recombination. The exciton has a finite nanometre size defined by the Bohr exciton diameter. If the size of the nanometre crystal is smaller than the size of the exciton, the charge carriers become spatially confined, and that raises their energy.[25] Under this condition, known as the quantum-confinement regime, the optical and electronic properties depend on the nanocrystal size.

Usually, the luminescence mechanism of QDs and the corresponding theoretical calculations assume that interior-to-interior transitions dominate the optical properties and neglect surface effects. However, optical properties of semiconductor QDs can only

be completely understood by considering surface effects.

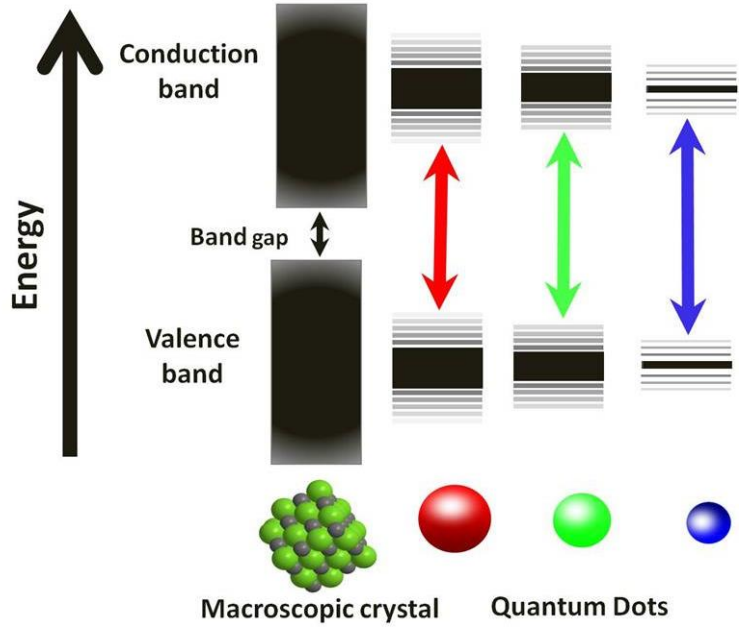

Figure 1.1: Schematic of the semiconductor levels

Silicon is a semiconductor that is electronically very stable and in contrast to all II-VI nanoparticles, exhibits a low inherent toxicity. As a semiconductor material, it would be more natural to also name Si nanoparticles "quantum dots" but in the wide body of literature they are named silicon nanocrystals (Si NCs) and this will be how they are referred to in this thesis. Si NCs are one type of semiconductor nanomaterial where surface defects may play an important role besides quantum-confined effects.[26-28] Bulk silicon has $E_g = 1.14$ eV, but shows no significant optical performance due to the indirect character of its band-gap and displays weak emission in the near infrared.[26] In this case the transition from the bottom of the conduction to the top of the valence band violates conservation of momentum and is electronically forbidden, see Figure 1.2.[29]

The discovery of red photoluminescence from porous silicon opened the research into Si-NCs.[30] The exciton Bohr radius of silicon is 4 nm and, under a strong quantum-confinement regime, the probability of radiative recombination through direct band-gap transitions increases and through phonon-assisted indirect bandgap transitions, reduces.[28] Si-NCs are highly luminescent and show quantum-confinement size-dependent properties resulting in the widening of the band-gap from 1.14 eV of the bulk to about 3.26 eV (380 nm).[30, 31] Also, if a large number of atoms are located at or near

the surface of the NCs, leading to a preponderance of dangling bonds and defects, besides adsorbed impurities, this results in surface states which can act as traps or recombination sites generating quite complex light-emission profiles. [26, 28] For carbon quantum dots the fluorescence mechanism is not clearly defined, however it seems to be dependent of two factors: the surface defects and the quantum confinement effect.

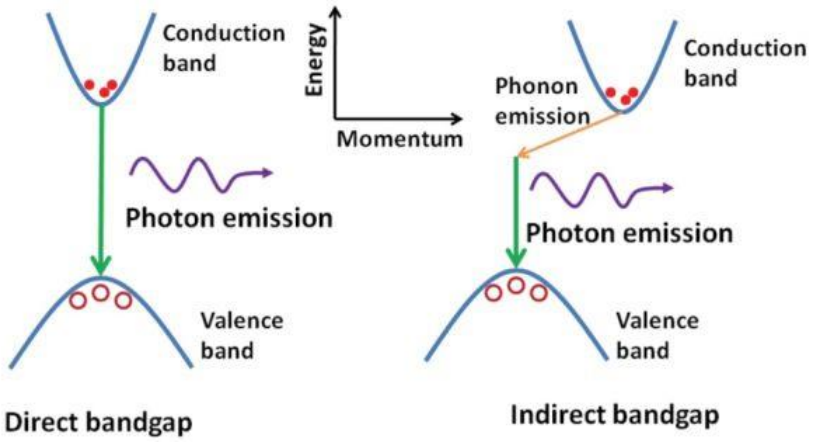

Figure 1.2: Illustration of a photon emission process in (a) the direct and (b) the indirect bandgap semiconductors.[29]

1.3 Methods of Preparing Silicon Nanocrystals

In recent times the synthesis of Si NCs in the range of 1-5 nm have been explored due to their unique optical and photo physical properties that are not found in the bulk. A wide variety of methods have been developed for the preparation of colloidal Si NCs. Considerable efforts have focused on producing well defined, stable and size monodisperse Si NCs, whilst effectively controlling the optical properties, shapes and surface chemistry. The ideal method of producing Si NCs would involve addressing all of the above issues while also producing large quantities of NCs at a low cost. At the moment Si NCs are produced from a variety of physical approaches, *i.e.* breaking down larger pieces of Si to smaller nanoscale pieces, or chemical approaches that primarily rely on self-assembly processes using molecular Si precursor species.

1.3.1 Physical Methods

1.3.1.1 Etching and Sonication of Bulk Silicon

Leigh Canham was the first person to show that certain porous Si materials can have large photoluminescence efficiency at room temperature in the visible region. He demonstrated that free-standing Si quantum wires could be fabricated without the use of epitaxial deposition or lithography. His approach used electrochemical and chemical dissolution steps to define networks of isolated wires out of bulk wafers. [32]

Wolkin *et al.* prepared porous Si quantum dot samples by electrochemical etching followed by photo assisted stain etching of p-type Si wafers at current densities of 8 – 50 mA cm^{-2} using 10 – 25% mixture of hydrofluoric acid (HF):ethanol (EtOH) solutions. They demonstrated that the photoluminescence (PL) of Si NCs present in porous Si could be tuned from the near infrared to the ultraviolet when the surface was passivated with silicon-hydrogen (Si-H) bonds. They found that once the samples were exposed to oxygen, the PL red shifted and the intensity also changed. They also developed a theoretical model, in which new electronic states appear in the bandgap of the smaller NCs when a silicon-oxygen (Si-O) bond is formed, which was in good agreement with the experimental results. They concluded that both quantum confinement and surface passivation determined the electronic states of Si NCs. [33]

Kang *et al.* prepared size tunable Si NCs using an etching method whereby the colour varied from blue to red. In this approach, a graphite rod was used as the anode and Si wafer as the cathode. Kang *et al.* found that the use of polyoxometalates was important due to their unique ability to act as an electron donor and acceptor simultaneously. Altering the current density was used to adjust the size of particles upon HF: H_2O_2 etching, producing shape and size controlled hydrogen terminated Si NCs with size ranging from 1 – 4 nm and emission peak between 450 – 700 nm. Kang *et al.* also found that the etching mixture could be further modified to provide control over the oxidizing environment using a mixture of H_2O_2 and ethanol. As a result, the larger particles were partially oxidized to yield small crystalline Si cores in an oxide shell, resulting in a wide spectrum of colours, see Figure 1.3.[34]

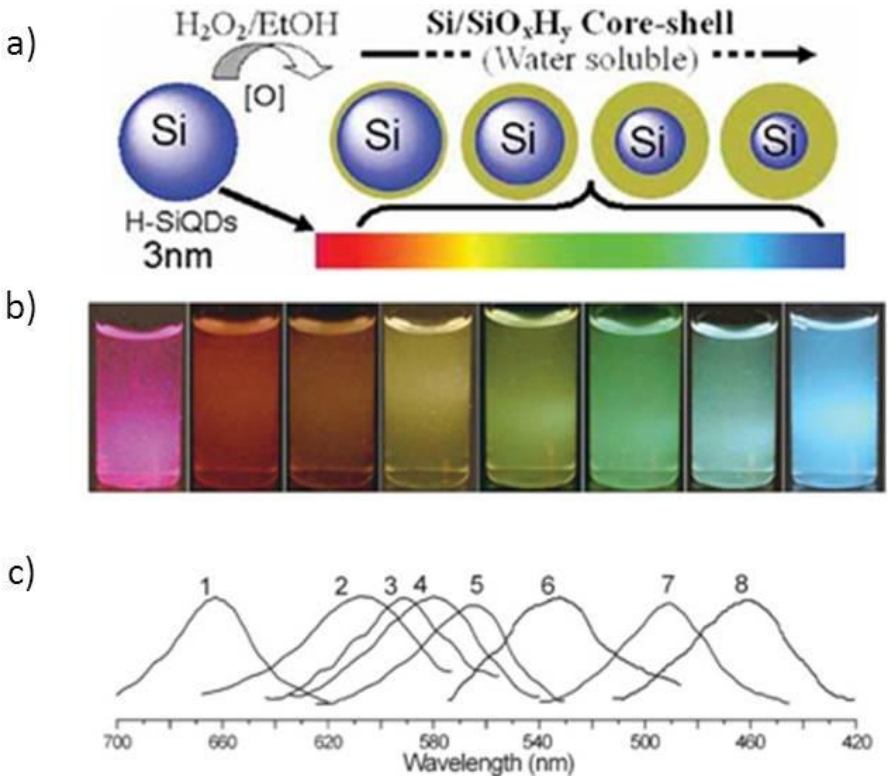

Figure 1.3: a) Etching procedure used to form Si NCs. b) Photograph (under UV light) of H-Si NCs (left, red emission) and seven water soluble Si NCs (yielding seven distinct emission colours). c) PL spectra of H-Si NCs (curve 1) and Si NCs after 0.5, 1.5, 3.5, 6, 9, 14, and 24 h oxidization (curves 2 to 8), respectively (excitation wavelength: 360 nm).[34]

Belomoin and co-workers demonstrated that electrochemically etched hydrogen-capped Si_aH_b clusters with *a* larger than 20 are obtained as a family of discrete sizes. These sizes are 1.0 (Si_{29}), 1.67 (Si_{123}), 2.15, 2.9, and 3.7 nm in diameter. The bandgaps and emission bands were measured. The smallest four were ultrabright blue, green, yellow and red luminescent particles. The blue particles were obtained by brief treatment of the wafer in an ultrasonic bath, where the film crumbled into a colloidal suspension of ultrasmall blue particles.[35]

Heinrich *et al.* demonstrated that colloidal Si NCs can be prepared *via* etching of bulk silicon. Heinrich demonstrated this process with a mixture of HF and H_2O_2 to electrochemically etch porous Si with the aid of ultrasound, and created a luminescent colloidal suspension. The suspension contained small crystalline Si NCs with a broad size distribution, and exhibited bright orange emission. [36] Due to its simplicity, this approach gained rapid attention, and has been widely used ever since. For instance, it was recently shown that etching of Si powder with the assistance of ultrasound and a combination of nitric acid (HNO_3) and hydrofluoric acid produced Si NCs with controlled emission.[37]

Cichos and co-workers [38] and Valenta *et al.* [39] prepared colloidal suspensions of Si NCs from light-emitting porous Si grains. Valenta *et al.* obtained NCs by mechanical pulverization of electrochemically etched layers. Sedimented and/or filtered Si NCs solutions revealed a green PL band around 530 nm, which was interpreted as radiative recombination of electron – hole pairs inside Si NCs with diameter about 2 nm. On the other hand, their preparation of concentrated suspensions enabled Valenta *et al.* to fabricate bulk samples with embedded Si NCs or to prepare self-organized nanostructures on surfaces.

1.3.1.2 Reactive Sputtering and Ion Implantation

Furukawa and Miyasato succeeded in fabricating mostly crystalline Si-H materials, using a reactive sputtering technique with a low substrate temperature of ~100 K. The structural analysis showed that the materials consisted of crystalline Si NPs surrounded by hydrogen atoms, whose diameters were 2-3 nm. They explained the widening of the optical bandgap by a three dimensional quantum-size effect in the particles. [40]

1.3.1.3 Thermal Annealing

Schoenfeld and co-workers formed Si NCs by crystallizing amorphous Si thin films, deposited on Si (110) substrates, using a rapid thermal annealing technique. Room temperature PL using a 338 nm line of an N_2 laser for excitation showed intense blue light emission from the Si NCs in the nanocrystalline thin films. The luminescence band between 2.6 and 3.2 eV consisted of distinct peaks. [41]

Liu and colleagues successfully prepared Si NCs through annealing and subsequent etching with HF from amorphous SiO_x powders. They obtained NCs with a narrow size distribution using a slow etching process. They observed photoluminescence, from the ultraviolet to the visible region. Liu *et al.* TEM micrographs showed the different morphology of the Si particles when dispersed in different solvents. At low concentrations, the NCs were observed to be distributed randomly in methanol, scattered in an isolated fashion with very large distance in octanol, and arranged themselves densely in toluene. When suspended in octanol at high concentrations, they observed the Si particles tended to self-assemble into large aggregates. [42]

Kapaklis *et al.* produced Si NCs by the simple disproportionation reaction of SiO at annealing temperatures of 900 – 950 °C. The NCs were spherical in shape, and exhibited a broad size distribution. All samples exhibited strong PL even at room temperature with three emission bands at 1.33, 1.52, and 1.67 eV. The authors claim that the first band originates from excitonic recombination in the Si NCs. They attributed the bands at higher energy to the presence of Si clusters in the samples and the gradual transition of these clusters to the crystalline state, since the annealing temperatures were not enough to fully disproportionate and crystallize SiO and, for a given cluster size, the bandgap in Si is smaller than in crystalline Si. [43]

1.3.1.4 Decomposition of Silanes

Littau and colleagues employed a high-temperature aerosol apparatus for the synthesis of 3 – 8 nm, surface-oxidized Si crystallites. The particles were made by homogeneous gas-phase nucleation following pyrolysis of dilute disilane in helium. The particles were collected as a robust ethylene glycol colloid. The particles exhibited a shell structure, with a crystalline Si core. After reflux, they noted that luminescence was observed from the nanocrystals. [44]

Fojtik and Henglein prepared crystalline Si particles by combustion of silane. The nanoparticles were etched in a cyclohexane/propan-2-ol suspension by aqueous HF in the presence of air to give red or orange luminescence nanoparticles. They observed that when a suspension of luminescent particles in cyclohexane was mixed with polar solvents such as alcohol, ether, and chloroform, the luminescence was quenched. They also observed that the particles migrated in an electric field in different directions depending on the chemical surface treatment. Fojtik and Henglein concluded that luminescence occurs when the particles carry only a few oxidized centres on the surface, and that the protonation state of these centres strongly affects the luminescence. [45]

Holmes *et al.* produced highly crystalline organic-monolayer passivated Si NCs in a supercritical fluid by thermally degrading diphenylsilane in the presence of octanol at 500 °C (above 80 bar). They reported size-monodisperse Si NCs ranging from 1.5 to 4 nm in diameter, could be obtained in significant quantities. The absorbance and PL excitation spectra of the passivated NCs exhibited a significant blue shift from the bulk bandgap energy of 1.2 eV due to quantum confinement effects. The Si clusters also showed efficient blue or green band-edge photoemission with luminescence quantum yields up to 23% at room temperature. [31]

English *et al.* produced sterically stabilized Si NCs by arrested precipitation in solvents, heated and pressurized above their critical points to temperatures ranging from 400 to 500 °C. These temperatures were sufficient to degrade diphenylsilane to Si to promote Si crystallization in the nanocrystal core and to initiate surface binding of organic capping ligands. The Si NCs demonstrated single-step “blinking” behaviour and size-

dependent PL spectra with line widths approximately only three times greater than those measured for cadmium selenide (CdSe) NCs at room temperature. [46]

Hessel *et al.* utilized thermal decomposition of hydrogen silsesquioxane to produce bulk amount of Si rich oxides as thin films under high temperature. This is followed by controlled HF etching to give hydride terminated Si NCs with emission wavelength tuneable in the visible spectrum, see Figure 1.4.[47]

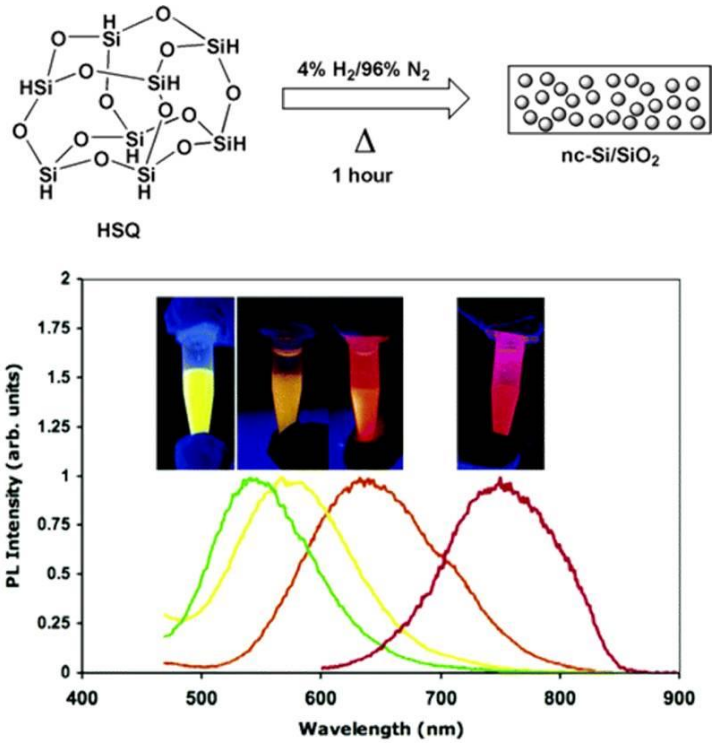

Figure 1.4: Preparation of colloidal Si NCs by decomposition of Si rich oxides containing Si nanocrystal.[47]

1.3.1.5 Thermal vaporization

Dinh *et al.* synthesized Si nanoclusters passivated with oxygen or hydrogen, with an average size of a few nanometers, by thermal vaporization of Si in an argon buffer gas. All their samples showed strong infrared and/or visible PL with varying decay times from nanoseconds to microseconds, depending on synthesis conditions. They noted the visible components of the PL spectra blue shifted and broadened as the size of the Si NCs was reduced. [48] Van Buuren and co-workers prepared Si NCs using the same thermal vaporization technique as Dinh *et al.* [48] and went on to study the changes in the electronic properties of the nanocrystallites as a function of particle size.

They observed shifts in both the conduction band and valence band edges, indicating quantum size effects in the band structure of the nanocrytals, and for the first time were able to correlate these shifts with a known size of nanocrystal. They found the general trend of the bandgap *versus* size curve agreed well with theory, but in all cases the experimental bandgap was smaller than the theoretical prediction. [49] Kovalev *et al.* prepared heavily oxidized Si NCs by Si ion implantation in a silicon dioxide (SiO_2) layer, with subsequent annealing at T = 1100 ºC for 15 minutes. [50]

1.3.1.6 Laser Ablation/ Pyrolysis

Niu and co-workers synthesized Si NCs with a diameter of ~ 4 nm at a rate of 400 – 500 mg/h by pulsed laser ablation of a Si (100) wafer in inert gas. [51] Similarly, Umezu and co-workers[52] prepared Si NPs by laser ablation in He/H_2 gas by pulsing a laser on a Si single crystal. By varying the partial pressure it was found that higher pressures result in higher particle crystallinity. The laser ablation method was rendered into a one-pot synthesis by Shiharata and co-workers,[53] who performed the ablation of a Si wafer in the presence of 1-octene, which effectively capped the NPs resulting in octyl-terminated Si NPs. The diameter of the Si NPs ranges from 1 to 10 nm and the highest fluorescence emission is found around 375 nm.

Hata and co-workers prepared Si NCs by laser ablation. Scanning tunneling microscopy (STM) and atomic force microscopy (AFM) observations, in addition to PL measurements, showed that the Si NCs were spherical in shape and remained stable for at least a couple of months. They were able to change the size of the Si NCs by changing the argon ambient pressure. [54]

Swihart *et al.* have fine-tuned a method in which silane is pyrolyzed by a carbon dioxide laser beam. The size of the NCs is controlled by varying the flow rates and the laser power. After formation the NPs are etched with HF: HNO_3 in water to reduce the NP size. The resulting NPs have an average diameter of 5 nm with a mixture of hydrogen/oxygen-terminated Si atoms at the surface. The PL from these particles is not stable, mainly because of the significant degree of oxidation and the irregularity of the surface. After additional treatment with 5% HF and hydrosilylation, various alkyl and ester-terminated Si NPs can be produced, showing much more stable photoluminescence spectra. [55-57]

1.3.1.7 Plasma Processing

Mangolini *et al.* presented a single-step continuous flow non-thermal plasma process that produced luminescent Si NCs between 2 – 8 nm on time scales of a few milliseconds. Process yields of 14–52 mg/h of luminescent particles were demonstrated, and they suggest the process is easily scalable. [58]

Giesen *et al.* investigated the formation and growth of Si NCs from silane in a microwave reactor. The silane was added to the plasma gases Ar/H_2, resulting in the formation of the Si NCs. A molecular beam technique was used together with a particle mass spectrometer (PMS) for sizing the product particles. They also collected and analyzed particles by Transmission Electron Microscopy (TEM) and X-ray diffraction (XRD). The particles were found to lie in the 5 – 8 nm range and consisted of crystalline Si. They also carried out simulations of the described experiments on an ultra-simple thermal plasma model. [59]

Sankaran and colleagues synthesized blue luminescent Si NCs from a mixture of argon/silane in a continuous flow atmospheric-pressure microdischarge reactor. Particles nucleated and grew to a few nanometers in diameter before their growth was abruptly terminated in the short residence time microreactor. The as-grown Si NCs collected in solution and were found to exhibit room-temperature PL that peaked at 420 nm with a quantum yield of 30%, the emission was found to be stable for months in ambient air. [60]

Mariotti *et al.* used atmospheric-pressure microplasma process to successfully produce Si NCs with stable properties in liquid media. The microplasma treatment induces non-equilibrium liquid chemistry that passivates the silicon nanocrystals surface with oxygen/organic-based terminations. In particular, the microplasma treatment in ethanol drastically enhances the silicon nanocrystals PL intensity and causes a clear red-shift of the PL maximum. The PL properties were found to be stable after several days of storage in either ethanol or water.[61, 62]

1.3.2 Chemicals Methods

1.3.2.1 Synthesis in Reverse Micelles

Wilcoxon *et al.* developed a synthesis method based on using inverse micelles as reaction vessels. In this approach, a Si precursor (SiX_4; X=Cl,Br, or I) is dissolved in the hydrophilic interior of a solution of micelles and nucleation and growth of Si NCs are restricted to the micelle interior. Control of cluster size can be achieved by variation of the micelle size, intermicellar interactions and reaction chemistry. The reaction is performed under inert atmospheric conditions in order to prevent the oxidation of Si NCs. They found that the reaction yielded polydisperse (d = 2 – 10 nm) Si NCs which exhibited a highly structured optical absorption and photoluminescence across the visible range of the spectrum. The optical absorption revealed features associated with both the indirect and direct bandgap transitions, and these transitions exhibited different quantum confinement effects. The indirect bandgap shifted from 1.1 eV in the bulk to ~2.1 eV for NCs (~2 nm in diameter) and the direct transition blue-shifted by 0.4 eV from its 3.4 eV bulk value over the same size range. The most intense PL was in the violet region of the spectrum (~365 nm) and was attributed to direct electron-hole recombination. Other less intense PL peaks were attributed to surface state and to indirect bandgap recombination. [63]

Tilley *et al.* later used a similar method to prepare very small quantities of small size monodisperse free standing Si NCs (d = 1.8 ± 0.2 nm). The Si NCs were capped with 1-heptene, purifed and redispersed into hexane and showed strong PL in the visible regime. Colloidal suspensions of the 1-heptene Si NCs were stable for at least 6 months in air, showing their resistance to photo-oxidization. [64] Rosso Vassic *et al.* also used an adaption of this method to produce highly monodisperse Si NCs (d = 1.57 ± 0.21 nm) which were synthesised with a covalently attached alkyl monolayer on a gram scale. Infrared spectroscopy shows that these Si NCs contain maximally only a few oxygen atoms per nanocrystal. [65] Wang *et al.* formed Si NCs by chemical reduction of Si tetrachloride using hexyltrichlorosilane. The authors noted that hexyltrichlorosilane acts both as both reductant and ligand. The synthesis yields brightly luminescent Si NCs, and enables efficient synthesis of alkyl-functionalised Si NCs in a single step. [66]

Cheng *et al.* formed Si NCs that could be dispersed in a variety of polar and non-polar solvents. The authors utilised hexyl trichlorosilane which acts as both the surfactant and the reactant, self-assembling around halogenated silane precursors. They demonstrated that the Si NCs prepared by this method can be reacted with a variety of thiol bearing molecules, rendering the particles functionalized with a wide choice of distal groups, using the thiol–ene click reaction. By using a range of surface tethered functionalized alkanethiols, they showed that the particles can be dispersed in either aqueous or organic phase, as well as having their emission properties altered, see Figure 1.5.[67]

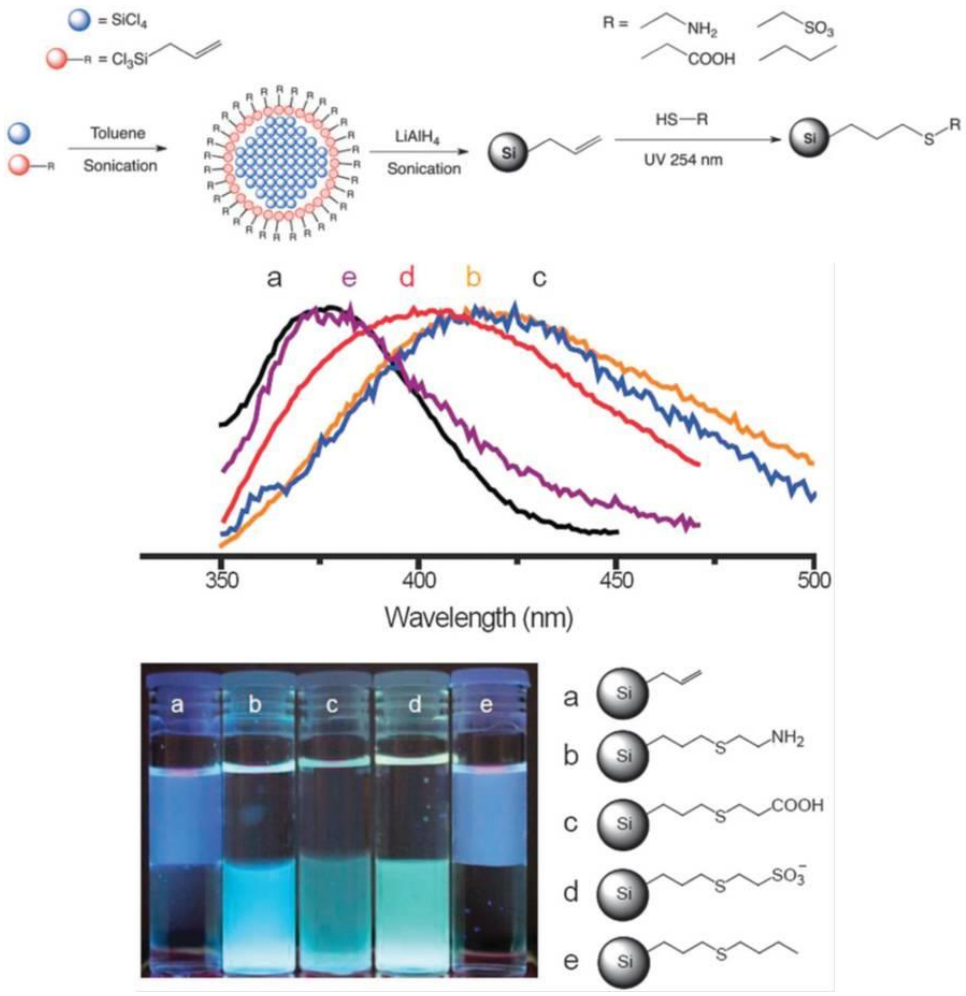

Figure 1.5: One-pot synthesis (upper) of alkene coated Si NCs functionalization via thiol–ene click chemistry. Photoluminescence spectra (middle) showing emission of Si NCs with different surface groups (a–e) excited at 320 nm. The lower picture shows change of fluorescence colour and hydrophobicity of the particles upon introduction of surface molecules. Images are taken with UV excitation (365 nm). Each vial contains hexane (upper layer) and H_2O (lower layer) with a particle concentration of 4 mg/ml.[67]

1.3.2.2 Solution Phase Oxidation-Reduction

Kauzlarich and co-workers have developed various solution phase oxidation-reduction reactions. Precursor Si containing compounds are combined in solution for nanocrystal nucleation and growth under atmospheric conditions. A variety of routes have been investigated such as reduction of $SiCl_4$ with NaSi,[68] oxidation of Mg_2Si with Br_2[69, 70] and reduction of $SiCl_4$ with Na-naphthalenide[71] to produce Si NCs. The main advantage of these methods is definitely their versatility and as a result can also be employed to produce doped Si NCs (with Mn[72] or P[73]) or mixed Silicon or germanium NCs.[74] Si NCs are initially terminated with halogen atoms (Cl or Br) that allow a lot of possible options for further functionalisation/stabilization, for example by using alkyl lithium (R-Li) compounds,[68, 69] alkoxy groups or hydrogen atoms by reduction with lithium aluminium hydride.[70]

Solution phase oxidation-reduction methods are some of the few that can claim to provide partial control over the nanocrystal shape. In particular, sodium naphthalene has been proven useful for preparing free standing Si nanocrystal of various sizes and surface chemistry.[73] The major drawbacks of this synthesis approach are the polydispersity of the obtained material (1 – 20 nm, and in the best case 3 – 6 nm) the labour and time consuming reaction conditions (72 h per reaction) and the requirement of an extensive purification. Fourier Transform Infrared Spectroscopy (FTIR) analysis of the isolated NCs shows besides characteristic C-H bands, also a significant degree of oxidation which subsequently leads to red tailed broad emission features.

Although a wide variety of methods are reported for the preparation of Si NCs, as described in Section 1.3, a number of advantages and drawbacks do exists for both physical and chemical approaches. A major advantage of the physical methods is the good compatibility with studies of flat or porous silicon structures in terms of procedures used and techniques required. The physical methods also offer good control of emission wavelength that cannot be easily achieved by other methods. However a number of disadvantages are also associated with the physical approaches. A lot of the physical methods require expensive processing equipment and clean room facilities to produce Si NCs. In certain cases the physical methods does not provide much control of either the NC's core diameters or their surface coverage, while the large numbers of surface defect sites limits the efficiencies of emissive devices by providing non-

radiative recombination routes. A number of harsh conditions are also used such as the requirements of high concentration of HF, and the heat treatment of silicon rich oxides which are not easily approachable by non-experts.[75, 76] These issues have hampered these methods from progressing towards large scale production or wide applicability, due to the high safety risk involved and specific techniques required.

The advantages of the chemical routes are they are potentially lower cost, and allow for more facile production of stable NC dispersions. A lot of the chemical methods require standard equipment and common reagents that are compatible with bench top chemistry. The Si NCs can also be prepared in good yield with excellent quality when considering scaling up the production of applications. Other benefits of the chemical approaches is that they can readily provide size monodisperse Si NCs, which may be prepared as stable dispersions, with close control of internal structure, surface treatments and doping levels. In contrast one major issue with the chemical approaches is the lack of full colour emission spectrum. The majority of methods produce a blue-green colour, although red emitting Si NCs have been produced, in most cases the use of HF is employed to further etch the NCs. The quantum yield of the solution methods rarely exceed 20% and are much lower in comparison to top down methods.

1.4 Methods of Preparing Carbon Quantum Dots

Carbon quantum dots (CQDs) are a new class of nano-materials with sizes below 10 nm which have attracted a lot of attention from the scientific community in recent years due to their unique photophysical properties. Although the research area is relatively new a vast amount of progress has been achieved. A lot of methods has been established in the literature which can be classified into two main groups: top-down and bottom-up methods.[77,78]Top-down methods consist of arc discharge, laser ablation, and electrochemical oxidation, where the CQDs are formed or "broken off" from a larger carbon structure. Bottom-up approaches consist, for example, of combustion/thermal supported synthetic, or microwave methods during which the CQDs are formed from molecular precursors.

1.4.1 Top Down Approaches

1.4.1.1 Laser Ablation

Sun *et al*. produced bright luminescence CQDs *via* laser ablation. A carbon target was prepared by hot-pressing a mixture of graphite powder and cement, followed by step wise baking, curing, and annealing under an argon flow. A laser was used to ablate the carbon target under a flow of argon gas carrying water vapour at 900 °C and 75 kPa. The sample was refluxed in HNO_3 for up to 12 h and surface passivated by attaching simple polymeric agent (polyethylene glycol or poly(propionylethyleneimine-co-ethyleneimine).[79, 80]

Du *et al*. reported the synthesis of fluorescent CQDs by laser irradiation of a suspension of carbon materials in organic solvent, see Figure 1.6. A pulsed neodymium-doped yttrium aluminium garnet laser was used to irradiate graphite or carbon black dispersed in diamine hydrate, diethanolamine, or polyethylene glycol for 2 h while under ultrasonication. Centrifugation was used to precipitate residual carbon powder fragments while CQDs remained suspended in the supernatant. By selecting organic solvents, the surface states of CQDs could be modified to achieve tunable light emission. Based on control experiments, the origin of the luminescence was attributed to the surface states related to the ligands on the surface of CQDs.[81]

Li *et al.* reported the preparation CQDs using laser ablation. In this approach nano-carbon material was dispersed in a polar solvent (such as ethanol, acetone, or water). After ultrasonication, 4 mL of the suspension was dropped into a glass cell for laser irradiation. An neodymium-doped yttrium aluminium garnet pulsed laser with a second harmonic wavelength of 532 nm was used to irradiate the suspension.[82]

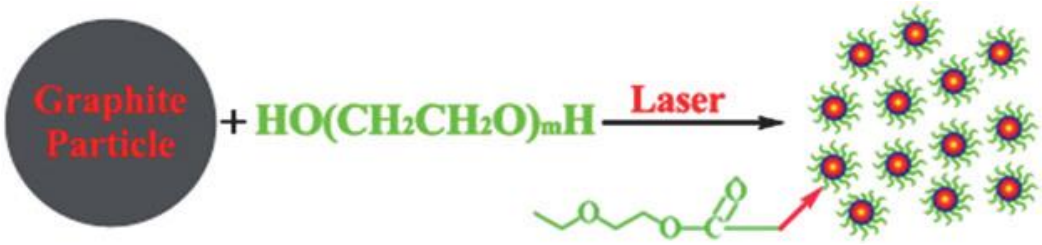

Figure 1.6: One step synthesis of CQDs in PEG200N solvent.[81]

1.4.1.2 Arc Discharge

Xu *et al*. isolated an unknown fluorescent carbon nanomaterial while purifying single-walled carbon nanotubes derived from arc-discharge soot. To improve the hydrophilicity of the material, they oxidized the arc soot with HNO_3 to introduce carboxyl functional groups, which improved the hydrophilicity of the material. The sediment was then extracted with a sodium hydroxide solution which resulted in a stable black suspension. The suspension was separated by gel electrophoresis into single-walled carbon nanotubes, short tubular carbons, and what can now referred to as CQDs. The CQDs were separated into three electrophoretic bands which upon excitation at 366 nm emitted green-blue, yellow, and orange in order of their elution and increasing size.[83]

1.4.1.3 Electrochemical Synthesis

Zhou *et al.* reported the formation of CQDs by electrochemical synthesis. They grew multiwalled carbon nanotubes from scrolled graphene layers on carbon paper by chemical vapour deposition (CVD). Zhao *et al.* produced CQDs electrochemically by oxidizing a graphitic column electrode against a saturated calomel electrode with a Platinum wire counter electrode in monopotasium phosphate aqueous solution. [84]

Chi *et al.* produced CQDs electrochemically from a graphite rod working electrode, a platinum mesh counter electrode, and a Ag/AgCl reference electrode. A variety of carbon based nanoparticles, including CQDs, were generated by ionic liquid assisted

electrooxidation of graphite using the water-soluble ionic liquid 1-butyl-3-methylimidazoliumtetrafluoroborate containing up to 90 wt% water as the electrolyte.[85]

Qu et al. reported the electrochemical synthesis of green luminescent GQDs with a uniform size of 3–5 nm. They prepared GQDs by electrochemical oxidation of a graphene electrode in phosphate buffer solution. The oxygen-containing groups on the surface of GQDs enabled aqueous solubility and facilitated surface functionalization. Such GQDs produced by electrochemical oxidation were made of 1–3 graphene layers due to strong inter graphene attraction.[86]

1.4.1.4 Plasma Treatment

Gokus *et al.* reported that strong PL could be induced in single-layer graphene using oxygen plasma. The PL was spatially uniform across the flakes and connected to elastic scattering spectra distinctly different from those of gapless pristine graphene; Raman spectroscopy and elastic light scattering were used to monitor the structural and optical changes. Interestingly, the graphene oxide nanosheets possessed visible and near-infrared fluorescence. [87]

Jiang *et al.* described a one-step combined synthesis and functionalization of CQDs using an all-in-one small submerged arc plasma reactor. They took advantage of the long-lived free radicals generated by a submerged-arc helium atmosphere plasma resident on the nanoparticle surfaces to supply ethylenediamine to functionalize the CQDs.[88]

1.4.2 Bottom-up Approaches

1.4.2.1 Hydrothermal and Solvothermal Routes

Pan *et al.* reported a hydrothermal route for cutting graphene sheets into blue luminescent CQDs. The obtained CQDs exhibited strong fluorescence with a quantum yield of 6.9%.[89] Fluorescent CQDs with diameter about 2.0 nm were also prepared directly *via* a simple hydrothermal method by using L-ascorbic acid as a carbon source. [90]

Yang *et al.* reported the preparation of CQDs using hydrothermal treatment of glucose in the presence of monopotasium phosphate. They implemented monopotasium phosphate as a fluorescence colour reagent. They noted that when a high concentration of monopotasium phosphate was used the CQDs showed a blue colour. While at low concentration of monopotasium phosphate a green colour was observed. [91]

Zhu *et al.* prepared the synthesis of CQDs by the hydrothermal treatment of citric and ethylenediamine with reported quantum yields of 80 % which are the highest to date.[92] Recently biological materials like pomelo peel,[93] orange juice, [94]strawberry, [95] soy mik[96] and willow bark[97] have been used as carbon sources for hydrothermal preparation of CQDs. Hydrothermal and solvothermal methods are popular techniques for preparing CQDs, and a lot of the methods reported in the literature are summarised in Table 1.

1.4.2.2 Microwave/Ultrasonic synthesis.

Microwave technology is another popular technique that is used in the preparation of CQDs and a lot of work has been reported in the literature using microwave synthesis methods, as shown in Table 2. Zhu *et al.* presented a facile and economical microwave pyrolysis approach to synthesize fluorescent CQDs with electrochemiluminescence properties. In this synthesis, different amounts of polyethylene glycol 200 (PEG200) and saccharide were added to distilled water to form a transparent solution. The solution was heated in a 500 Watt microwave oven for several minutes. With increasing reaction time, the solution changed from colorless to yellow, and finally to dark brown, which implied the formation of CQDs.[98]

Wang *et al.* reported a facile and green one-step microwave synthesis of photoluminescent CQDs. The preparation requires a carbohydrate (glycerol, glycol, glucose, sucrose, etc.) and a tiny amount of an inorganic ion, and can be completed in just a few minutes, requiring no surface passivation reagent.[99] Nitrogen doped CQDs were synthesised by microwave method using a nitrogen source, like nitrogen-containing amine acids,[100] Dimethylformamide[101] and chitosan. [102]

Qu *et al*. reported the microwave synthesis of fluorescence CQDs using citric acid and urea at 700 Watt for ~ 5 min. These synthesised CQDs can emit light in dry and aggregate states and can be applied to coat on commercial gauzes, animal's furs and skins as fluorescence inks.[103]

Table 1. Hydrothermal and Solvothermal synthesis of carbon quantum dots.

T (°C)	Time (hr)	FC	Size (nm)	Reactants	Ref.	QY (%)[a]
300	2	Blue	1-5	APTMS (AEAPTMS, TEOS)	104	42.6
300	2	Blue	2.6-7.9	Glycine (Tris, EDTA, Cadaverine)	105	5-30
250	2	Blue	2	2-(2-aminoethoxy)-ethanol	106	19.2
220	24	Blue-green	3	EDTA.2Na	107	15
210	36	Blue	7-12	CTAB, HCl, $Na_2S_2O_8$	108	9.8
200	15	Blue	5	Soot	109	4.96
200	1,8	Blue, Cyan, Green, Yellow	1-2, 2.5-4	CCl_4, $NaNH_2$	110	22
200	2	Blue	3-5	CCl_4, Quinol, NaOH, Ethanol	111	3.4
200	12	Blue-Green	1.8-3.8	Phosphate (N_2 filled)	91	1-2.4
200	3	Blue	1.7	Gelatin	112	31.6
200	3	Blue	35	Giant Knotweed Rhizome	113	11.5
200	3	Blue	2-4	Pomelo peel	93	6.9

Table 1. (continued) Hydrothermal and Solvothermal synthesis of carbon quantum dots.

T (°C)	Time (hr)	FC	Size (nm)	Reactants	Ref	QY (%)[a]
180	12	Blue	5.2	Strawberry juice	95	6.3
180	12	Blue	6.8	BSA, Ethanol	114	7
180	6	Blue-Green	3-5	Dopamine	115	6.4
180	3	Blue	13-40	Soy Milk	96	2.6
180	4	Blue	2-2.5	L-Ascorbic acid, Ethanol	90	6.79
160	~1.1	Green	5	L-Ascorbic acid, Glycol	116	5.7
150	4	Green	1.5-4.5	Banana Juice, Ethanol	117	8.95
150-300	5	Blue	2-6	Ethylenediamine	92	80
120	2.5	Green	1.5-4.5, 50-60	Orange juice, Ethanol	94	19-25
60	1	Blue	1-5	CCl_4, EDA	118	11

a. Quinoline sulafate as a standard

T. stands for temperature. FC stands for Fluorescence colour. Ref. stands for reference. QY stands for quantum yield. APTMS stands for 3-aminopropyltrimethoxysilane. AEAPTMS stands for 3-(2-Aminoethylamino) propyltrimethoxysilane. TEOS stands for tetraethylorthosilicate. Tris stands for 2-amino-2-hydroxymethyl-propane-1, 3-diol. EDTA stands for ethylene diamine tetraacetic acid. CTAB stands for cetyltrimethylammonium bromide. HCl stands for Hydrochloric acid. $Na_2S_20_8$ stands for sodium persulfate. CCl_4 stands for carbon tetrachloride. $NaNH_2$ stands for sodium amide. NaOH stands for sodium hydroxide. N_2 stands for Nitrogen. BSA stands for bovine serum albumin. EDA stands for 1,2-ethlenediamine.

Table 2. Microwave synthesis of carbon quantum dots.

Watt	Time (min)	FC	Size (nm)	Reactants	Ref	QY (%)[a]
900	10	Blue	4.5	PEG200	119	16
800	2.5	Violet	3-7	Dextrin, H_2SO_4	120	5-9
800	1	Blue	27	L-arginine	100	25
750	14	Blue	1.1-2.1	Glycerol (Glycol, Glucose, Sucrose), Inorganic Salts	121	3.2,9.5
750	14	Blue	7-12	Glycerol	122	/
750	4-5	Blue	1-5	Citric acid, Urea	103	14
720	2	Blue	/	Citric acid, 1,2-ethylenediamine	123	43.8
700	7	Blue	2.0-3.2	1,2-ethanediamine	124	31.3
700	~2	Blue	2	Histidine, Ortho-phosphoric acid	125	44.9
700	2	Blue	2.2-3.0	(DIA) (EA, TPA), Acid	126	/
700	2/3	Blue	1-6	DMF, Acids	101	9
700	10	Blue	3.5	Glycerol, TTDDA	127	12.0

Table 2. (continued) Microwave synthesis of carbon quantum dots.

Watt	Time (min)	FC	Size (nm)	Reactants	Ref	QY (%)[a]
700	9.5	Blue	4.6	Chitosan	102	6.4
500	2-10	Blue	~2-3	PEG200, Saccharide	98	3.1-6.3
450	5-6	Blue	2-10, 2-4, 1-2	Chitosan, Alginic acid, PEG200	128	/
450	2	Blue	6	OPPF6	129	27
450	4	Blue	5-20	PF-68, O-phosphoric acid	130	7
100	11/3	Green	3-10	Sucrose, Phosphoric acid	131	/

a. Quinoline sulafate as a standard

FC stands for Fluorescence colour. Refstands for reference. QY stands for quantum yield. H_2SO_4 stands for sulphuric acid. DIA stands for dimethylamine. EA stands for ethylamine. TPA stands for tripropylamine. DMF stands for dimethylformamide. TTDDA stands for 4,7,10-trioxa-1,13-tridecanediamine. OPPF6 stands for N-octylpyridinumhexafluorophosphate "/" stands for no information.

1.4.2.3 Supported Synthetic Procedures

Supported synthetic methods have been widely adopted for the synthesis of monodisperse nanomaterials. One such route was employed by *Li et al.*, who used surfactant-modified silica spheres as supports to localize the growth of CQDs by blocking nanoparticle agglomeration during high-temperature treatment.[132] Giannelis and co-workers described the synthesis of supported CQDs (4–6 nm) using thermal oxidation of an appropriately ion-exchanged NaY zeolite. [133]

Zhu *et al.* reported a facile approach for preparing hydrophilic CQDs by using mesoporous silica spheres as nanoreactors in an impregnation method. Without further treatment, the resulting highly photoluminescent CQDs are monodisperse, photostable and of low toxicity, and show excellent luminescence properties. First, mesoporous silica spheres were prepared with N-hexadecylamine as the surfactant and tetraethoxysilane as the precursor using ammonia as a catalyst. Subsequently, mesoporous silica spheres were impregnated with a mixed solution of complex salts and citric acid. Subsequent calcination and removal of mesoporous silica supports generated the nanosized hydrophilic CQDs. The key feature of this method is the employment of mesoporous silica spheres as supports, which not only confines the CQDs to a narrow size distribution in the pores of mesoporous silica spheres, but also prevents the aggregation of the nanosized CQDs.[134]

1.4.2.4 Solution Synthetic Procedures

Rhee and co-workers reported the solution-phase synthesis of CQDs using reverse micelles as nanoscale reactors *via* condensation polymerisation and subsequent carbonization of glucose within sodium di-2-ethylhexyl sulfosuccinate micelles at 160 ºC. Control of the water-surfactant ratio within the micelle allowed the CQD diameter to be tuned from 1.8 to 4.1 nm, but with increasing polydispersity at larger diameters.[135]More recently, Rhee *et al.* reported the synthesis of size tunable CQDs using a soft template method. The size of the CQDs was controlled by regulating the amount of the emulsifier.[136] Jana and co-workers developed a chemical method to synthesis highly fluorescent carbon NPs which exhibited size dependent and tunable emission in the visible region.[137]

1.5 Detection of Metal Ions

Heavy metals are ubiquitous environmental contaminants and their toxicity makes their presence undesirable and a concern to human health. Heavy metals like lead, mercury and cadmium are not biologically essential and harmful to organisms and can cause adverse health effects at low level of exposure. Other metals such as iron, copper, zinc and manganese are nutritionally essential for a healthy life; hence there is ongoing demand to develop sensitive sensing strategies for detecting heavy metal ions in living systems. A variety of analytical methods fulfilling these demands are available. However, only some of them have found applications in routine analysis.

Recommended procedures for the detection of metals ions in water based samples include photometric methods, flame or graphite furnace atomic absorption spectroscopy (AAS), inductively coupled plasma emission or mass spectrometry (ICP-ES, ICP-MS), total reflection X-Ray fluorimetry (TXRF), anodic stripping voltammetry (ASV) and surface plasmon resonance (SPR).[138-141] These methods offer good limits of detection and wide linear ranges, but require high cost analytical instruments developed for the use in the laboratories. The necessary collection, transportation and pre-treatment of a sample is time consuming and a potential source of error.[142] In recent times smaller and portable and less expensive devices have been brought to the market.

The need for convenient and inexpensive approaches for the sensitive and selective detection of metal ions with rapid and easy manipulation are in ever-increasing demand. Although optical sensors have been built using organic dyes, recently a lot of attention has focused on quantum dots as fluorescent probes for metal ions.[143] Quantum dots exhibit unique optical and photophyscial properties that offer significant advantages over organic dyes as optical labels for chemo/bio-sensing, see Table 3.[144] Quantum dots can easily be functionalised allowing them to sense for a specific analayte. Moreover, the use of quantum dots allows the miniaturization of the complex sensing systems; thereby it is possible to produce the so called “lab on a chip”.[145] In 2002 Chen and Rosenzweig were the first to fully recognise the potential of QDs as metal ion probes. They demonstrated that thiol glycerol-capped CdS QDs could be used as a fluorescence probe for Cu^{2+} in the presence of Zn^{2+}. [146] More recently, there has been a number of sensors built using Si NCs and CQDs. Mercury which is known to be one of

Table 3. Comparison between quantum dots and organic dyes. [144]

Property	**Organic dyes**	**QDs**
Absorption profile	Narrow, discrete bands, FWHM ranges from 35 nm to 80-100 nm	Broad, unsymmetrical profile, increase steadily towards UV region
Emission profile	Asymmetric, FWHM 35 nm to 70-100 nm	Gaussian profile, FWHM, 30-90 nm
Stokes shift	Usually less than 50 nm	Usually less than 100 nm
Quantum yield	0.5-1 (visible),.05-0.2 (NIR)	0.1-0.8(visible),0.2-0.7(NIR)
Fluorescent lifetimes	1-5 ns	5- 100ns, up to μs for some red Si QD
Photochemical stability	Sufficient in the visible region, but can be insufficient for NIR dyes	High, sufficient in both the visible and NIR region
Multiple colours	Possible by varying molecular structure	Adjustable by varying size

the most dangerous and ubiquitous pollutants has been successfully detected using Si NCs,[147] see Figure 1.7 and also using CQDs. In particular CQDs has shown great promise in detection of a variety of different elements, see Table 4.

Table 4. Heavy metal detection of Carbon quantum Dots.

Metal Ion	Detection Limit	Linear range	Ref.
Co^{2+}	0.67 nM	1.0 -1000 nm	148
Sn^{2+}	0.36 µM	0.4 mM	149
Pb^{2+}	5.50 µM	0-6.0 mM	150
Fe^{3+}	2 nM	0-1 µM	151
Fe^{3+}	0.32 µM	0-20 µM	115
Cu^{2+}	100 nM	1-60 µM	152
Cu^{2+}	1µM	0.001-0.1 µM	153
Cu^{2+}	13 nM	0.001-0.1 mM	154
Hg^{2+}	0.23 nM	0.5-10 nM	93
Hg^{2+}	4.2 nM	0-3 µM	155
Hg^{2+}	10 nM	0.5µM	156

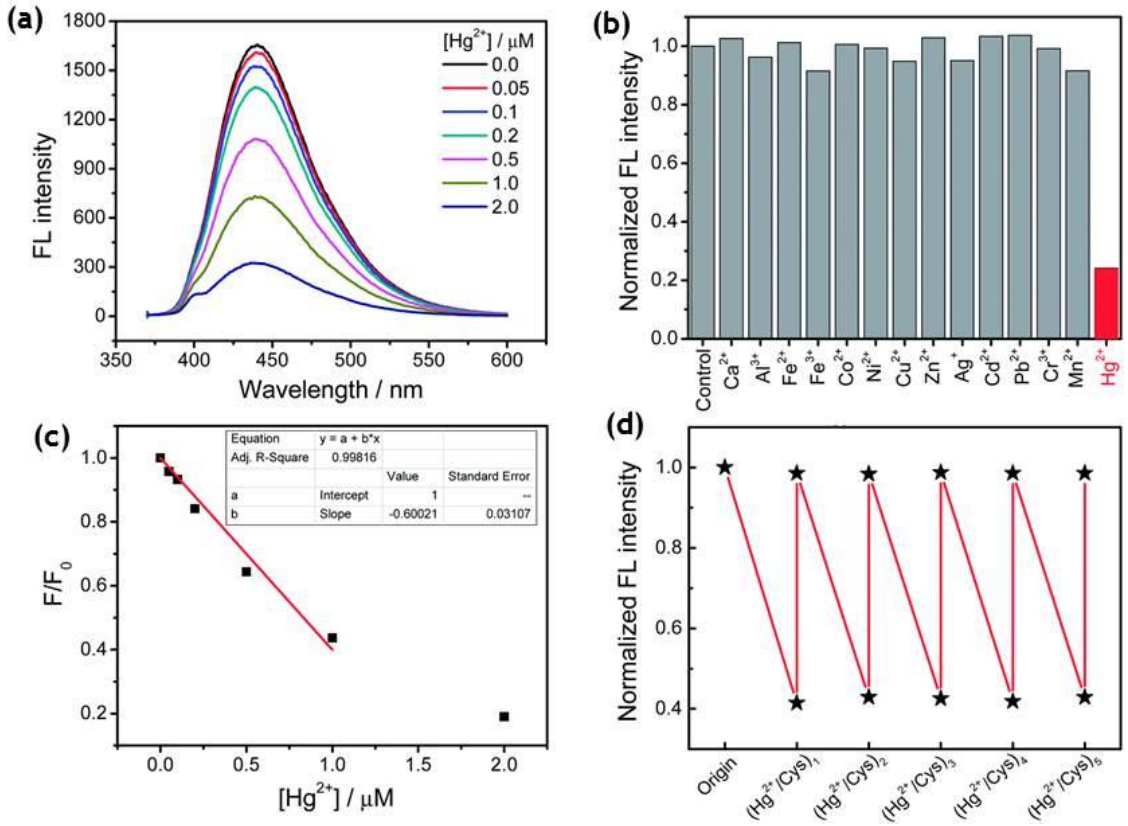

Figure 1.7: (a) The detection of Hg^{2+} by the Si NC probe using 350 nm excitation wavelength.[147]

The interaction of QDs and metal ions is complicated and a number of different interaction pathways can lead to fluorescence quenching outlined in the excellent review by Hou *et al*. see Figure 1.8.[143] The first quenching mechanism involves cationic-exchange between the quantum dot and metal ion. As a result, surface defects are generated, leading to a non-radiative recombination of the excitons and fluorescence quenching, see Figure 1.8 (a). Heavy metals such as Hg^{2+}, Cu^{2+}, Ag^{+}, and Pb^{2+} can compete with ligands on the surface of quantum dots such as thiols because of their high affinity. After detaching the ligands from the QDs, surface traps can be generated which can trap electrons from the conduction band, leading to fluorescence quenching, see Figure 1.8 (b). [157]

The third quenching pathway, as described by Isarov and Chrysochoos, is the reduction of surface adsorbed metal ions to form nonradiative surface channels, see Figure 1.8(c). This case is primarily observed for Cu^{2+} induced quenching metal chaleologenide QDs such as CdS of, in which Cu^{2+} was reduced to diamagnetic Cu^{+} by surface S^{2-} vacancies in the following way: $CdS + Cu^{2+} \rightarrow Cd^{S+} + Cu^{+}$. The resultant CdS^{+}–Cu^{+} has a lower energy level than pure CdS QDs, shifting the fluorescence to longer wavelengths, together with fluorescence quenching by Cu^{+} through a non-radiative recombination of excited electrons in the conduction band and holes in the valence band. Such mechanisms may not be limited to CdS QDs, but also other II-VI QDs since the reduction potential of Se^{2-} or Te^{2-} is higher than that of S^{2-}.[158]

For QDs with high density of surface ligands, the attack of the QD core by metal ions may be hindered. However, metal ions can still be adsorbed by QDs either *via* electrostatic attraction or ligand coordination. Since the metal ions are typically electron-deficient, electron transfer from the conduction band of the QDs to metal ions may occur, leading to fluorescence quenching, see Figure 1.8(d)[159, 160] In this case, the interaction of metal ions with ligands can be in part predicted with the Pearson acid base concept. For example, the borderline acids Co^{2+}, Ni^{2+}, Cu^{2+}, Pb^{2+} and Zn^{2+} prefer binding to ligands containing nitrogen donor atoms, while hard acids such as Ba^{2+}, Al^{3+}, Cr^{3+} and Mn^{2+} are prone to coordinate with oxygen-containing ligands.

The last potential source for fluorescence quenching is a rare case for Fe^{3+}, see Figure 1.8 (e). Chen and Rosenzweig observed the quenching of cysteine capped QDs by Fe^{3+},

which is attributed to an inner filter effect resulting from the strong adsorption by Fe^{3+} at the excitation wavelength.[146] Although diverse mechanisms have been proposed to explain the interactions between metal ions and QDs, many of the responses still cannot be fully predicted and rely on a speculative mechanistic understanding and missing details. Besides, these metal ion probes based on a direct interaction with QDs also have problems of batch-to-batch variations and less selectivity. The demand for more selective metal ion probes is the driving force for the functionalization of QDs with metal ion-selective receptors. The quenching of the fluorescence may occur through energy transfer, charge diverting, and surface absorption. The quenching mechanisms can be classified as dynamic quenching and static quenching.

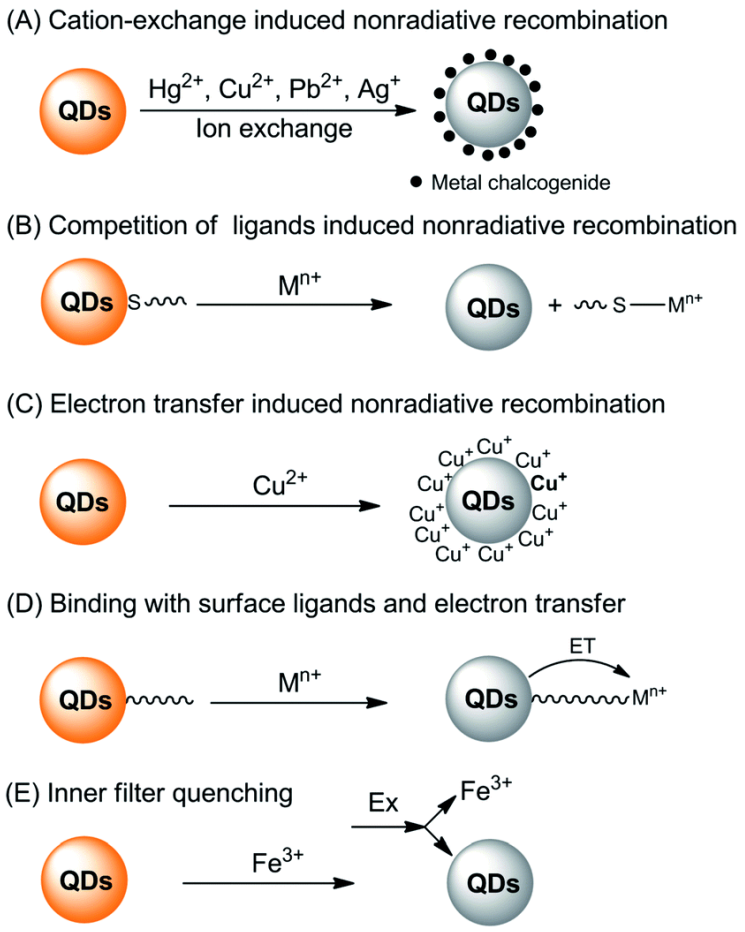

Figure 1.8: Summary of the fluorescence quenching mechanisms for the detection of metal ions based on direct interaction of the metal ions with QDs.[143]

1.5.1. Dynamic Quenching

Dynamic quenching occurs if a fluorophore is deactivated by the collision with a quencher during the lifetime of its excited state. The quenching species must diffuse to the fluorophore and upon contact, the fluorophore returns to the ground state, without emission of a photon. Quenching occurs without any permanent change of the molecule that is without a photochemical reaction. The mechanism for dynamic quenching is described by the Stern-Volmer equation, see equation 1.1:

$$\frac{F_0}{F} = 1 + K_q \tau_0 [Q] = 1 + K_D [Q] \quad (1.1)$$

Where F_0 and F are the fluorescence intensities in the absence and presence of quencher, respectively, K_q is the biomolecular quenching constant. τ_0 is the lifetime of the fluorophore in the absence of quencher, and Q is the concentration of quencher. K_D is the Stern-Volmer quenching constant and is represented by the following equation:

$$K_D = K_q \tau_0 \quad (1.2)$$

Generally F_0/F are plotted against the quencher concentration (Stern-Volmer plot). If the plot is found to be linear, the slope will give the Stern-Volmer constant.[161]

1.5.2 Static Quenching

Static quenching occurs when there is formation of a non-fluorescence complex of the fluorphore with the quencher in the ground state. Once the complex absorbs light it immediately returns to the ground state without emission of a photon, see equation 1.3. The association immediately returns to the ground state without emission of a photon.

$$F + Q \rightleftharpoons F\text{-}Q \quad (1.3)$$

The association constant for the formation of the complex is given by equation 1.4:

$$K_s = \frac{[F-Q]}{[F][Q]} \quad (1.4)$$

where [F-Q] is the concentration of the complex, [F] is the concentration of uncomplexed fluorophores and [Q] the quencher concentration. The total concentration

of fluorophores [F_0] is the sum of complexed and uncomplexed fluorophores (equation 1.5) and replacing [F-Q] yields equation 1.6.

$$[F_0] = [F] + [F - Q] \tag{1.5}$$

$$K_s = \frac{[F_0] - [F]}{[F][Q]} \tag{1.6}$$

Substituting the fluorophore concentration with the fluorescence intensities and rearranging equation 1.6 yields a similar Stern-Volmer equation.[161]

$$\frac{F_0}{F} = 1 + K_{qs}[Q] \tag{1.7}$$

Static and dynamic quenching can be distinguished by lifetime because dynamic quenching reduces the apparent fluorescent lifetime, while static quenching merely reduces the apparent concentration of the fluorophore. Although a number of proposed mechanisms have been put forward to explain the interactions between metal ions and QDs, many of the responses still cannot be fully understood and rely on speculative mechanistic understanding. Other factors such as batch to batch variance can contribute to the problems in the interpretation of the mechanisms.

1.6 Scope of the Thesis

The scope of this thesis is to synthesie and characterise novel group IV nanocrystals, and to demonstrate their ability as fluorescence probes for the detection of metal ions.

In chapter 2, a simple method is described for the size controlled synthesis of Si NCs within inverse micelles having well defined core diameters ranging from 2 to 6 nm using inert atmospheric synthetic methods. Since it is of key importance for opto-electronic applications, efforts focused on the development of routes that produce high quality NCs with standard deviations ($\sigma = \Delta d/d$) of less than 10 %. Regulation of the Si NCs size is achieved by variation of the cationic quaternary ammonium salts, non-ionic surfactants as well as addition rates. In addition, ligands with different molecular structures were utilised to reduce inter-nanocrystal attraction forces and improve the stability of the NC dispersions in water and a variety of organic solvents. A scale up synthesis is also developed for production of highly mondisperse Si NCs. In addition the stability and pH of the Si NCs are also investigated.

In chapter 3, a simple solution phase synthesis of size monodisperse carbon quantum dots (CQDs) using a room temperature microemulsion strategy is demonstrated. The CQDs are synthesized in reverse micelles *via* reduction of carbon tetrachloride using a hydride reducing agent. The hydrogen-terminated CQDs are functionalised using a platinum-catalysed concerted reaction to covalently attach an alkyl or amine monolayer, rendering the CQDs dispersible in wide range of polar or non-polar solvents. The CQDs possess a high photoluminescence quantum yield in the visible region and exhibit excellent photostability. In addition, a method for the size controlled synthesis of CQDs within inverse micelles having well defined core diameters ranging from 2 to 6 nm is also demonstrated. The CQDs are chemically passivated and made water soluble using an allylamine ligand. Regulation of the CQDs size was achieved by utilizing hydride reducing agents of different strengths. Through controlling the size of the CQDs, their resulting photoluminescence properties can be tuned.

In chapter 4, we report the development of a simple and rapid assay for the detection of Fe^{3+} ions. Quenching of the strong blue-green photoluminescence of the silicon nanocrystals is used as the transduction method for highly sensitive and selective detection of Fe^{3+} in aqueous solution. This detection method shows a high degree of selectivity, with only the presence of iron resulting in strong quenching of the fluorescence signal. In addition, the Si NCs show strong affinity toward Fe^{3+} ions, with no quenching of the fluorescence signal induced by Fe^{2+} ions, allowing for solution phase discrimination between ionic species with different charge states. The optimised sensor system shows a sensitive detection range from 25-900 μM and a limit of detection as low as 20.8 μM. To the best of our knowledge, this is the first study carried out on the use of silicon NCs as selective probes for the detection of Fe^{3+}.

In Chapter 5, the thesis concludes with a summary of the key results achieved in this work.

1.7 References:

1. Brus, L. E., Electron‑electron and electron‑hole interactions in small semiconductor crystallites: The size dependence of the lowest excited electronic state. *Journal of Chemical Physics* **1984**, *80*, 4403-4409.

2. Talapin, D. V.; Lee, J. S.; Kovalenko, M. V.; Shevchenko, E. V., Prospects of colloidal nanocrystals for electronic and optoelectronic applications. *Chemical Reviews* **2009**, *110*, 389-458.

3. Resch-Genger, U.; Grabolle, M.; Cavaliere-Jaricot, S.; Nitschke, R.; Nann, T., Quantum dots *versus* organic dyes as fluorescent labels. *Nature Methods* **2008**, *5*, 763-775.

4. Robel, I.; Subramanian, V.; Kuno, M.; Kamat, P. V., Quantum Dot solar cells. harvesting light energy with cdse nanocrystals molecularly linked to mesoscopic tio_2 films. *Journal of the American Chemical Society* **2006**, *128*, 2385-2393.

5. Kamat, P. V., Quantum Dot Solar Cells. Semiconductor nanocrystals as light harvesters. *The Journal of Physical Chemistry C* **2008**, *112*, 18737-18753.

6. Strauf, S.; Hennessy, K.; Rakher, M. T.; Choi, Y. S.; Badolato, A.; Andreani, L. C.; Hu, E. L.; Petroff, P. M.; Bouwmeester, D., Self-Tuned quantum dot gain in photonic crystal lasers. *Physical Review Letters* **2006**, *96*, 127404-1 - 12704-4.

7. Sun, Q.; Wang, Y. A.; Li, L. S.; Wang, D.; Zhu, T.; Xu, J.; Yang, C.; Li, Y., Bright, multicoloured light-emitting diodes based on quantum dots. *Nature Photonics* **2007**, *1*, 717-722.

8. Bruchez, M.; Moronne, M.; Gin, P.; Weiss, S.; Alivisatos, A. P., Semiconductor nanocrystals as fluorescent biological labels. *Science* **1998**, *281*, 2013-2016.

9. Chan, W. C. W.; Nie, S., Quantum Dot bioconjugates for ultrasensitive nonisotopic detection. *Science* **1998**, *281*, 2016-2018.

10. Lewinski, N.; Colvin, V.; Drezek, R., Cytotoxicity of nanoparticles. *Small* **2008**, *4*, 26-49.

11. Derfus, A. M.; Chan, W. C. W.; Bhatia, S. N., Probing the cytotoxicity of semiconductor quantum dots. *Nano Letters* **2003**, *4*, 11-18.

12. Kirchner, C.; Liedl, T.; Kudera, S.; Pellegrino, T.; Muñoz Javier, A.; Gaub, H. E.; Stölzle, S.; Fertig, N.; Parak, W. J., Cytotoxicity of colloidal cdse and cdse/zns nanoparticles. *Nano Letters* **2004**, *5*, 331-338.

13. Larson, D. R.; Zipfel, W. R.; Williams, R. M.; Clark, S. W.; Bruchez, M. P.; Wise, F. W.; Webb, W. W., Water-Soluble quantum dots for multiphoton fluorescence imaging in vivo. *Science* **2003**, *300*, 1434-1436.

14. McDonald, S. A.; Konstantatos, G.; Zhang, S.; Cyr, P. W.; Klem, E. J. D.; Levina, L.; Sargent, E. H., Solution-processed PbS quantum dot infrared photodetectors and photovoltaics. *Nature Materials* **2005**, *4*, 138-142.

15. Coe, S.; Woo, W. K.; Bawendi, M.; Bulovic, V., Electroluminescence from single monolayers of nanocrystals in molecular organic devices. *Nature* **2002**, *420*, 800-803.

16. Ding, Z.; Quinn, B. M.; Haram, S. K.; Pell, L. E.; Korgel, B. A.; Bard, A. J., Electrochemistry and electrogenerated chemiluminescence from silicon nanocrystal quantum dots. *Science* **2002**, *296*, 1293-1297.

17. Pavesi, L.; Dal Negro, L.; Mazzoleni, C.; Franzo, G.; Priolo, F., Optical gain in silicon nanocrystals. *Nature* **2000**, *408*, 440-444.

18. Sailor, M. J.; Lee, E. J., Surface chemistry of Luminescent Silicon Nanocrystallites. *Advanced Materials* **1997**, *9*, 783-793.

19. Holec, T.; Chvojka, T.; Jelínek, I.; Jindřich, J.; Němec, I.; Pelant, I.; Valenta, J.; Dian, J., Determination of sensoric parameters of porous silicon in sensing of organic vapors. *Materials Science and Engineering: C* **2002**, *19*, 251-254.

20. Li, Z. F.; Swihart, M. T.; Ruckenstein, E., Luminescent silicon nanoparticles capped by conductive polyaniline through the self-assembly method. *Langmuir* **2004**, *20*, 1963-1971.

21. Lee, S.; Cho, W. J.; Chin C.S.; Han, I. K.; Choi, W. J.; Park, Y. J.; Song, J. D.; Lee, J., Optical Properties of Silicon Nanoparticles by Ultrasound-Induced Solution Method. *Japan Journal of Applied physics* **2004**, *43*, L784.

22. Cheng, K. Y.; Anthony, R.; Kortshagen, U. R.; Holmes, R. J., High-Efficiency silicon nanocrystal light-emitting devices. *Nano Letters* **2011**, *11*, 1952-1956.

23. Ligman, R. K., Electroluminescence from surface oxidized silicon nanoparticles dispersed within a polymer matrix. *Applied Physics Letters* **2007**, *90*, 061116.

24. Cheng, K.Y.; Anthony, R.; Kortshagen, U. R.; Holmes, R. J., Hybrid silicon nanocrystal−organic light-emitting devices for infrared electroluminescence. *Nano Letters* **2010**, *10*, 1154-1157.

25. Smith, A. M.; Nie, S., Semiconductor nanocrystals: structure, properties, and band gap engineering. *Accounts of Chemical Research* **2009**, *43*, 190-200.

26. Wilcoxon, J. P.; Samara, G. A.; Provencio, P. N., Optical and electronic properties of Si nanoclusters synthesized in inverse micelles. *Physical Review B* **1999**, *60*, 2704.

27. Warner, J. H.; Hoshino, A.; Yamamoto, K.; Tilley, R. D., Water-Soluble photoluminescent silicon quantum dots. *Angewandte Chemie International Edition* **2005**, *44*, 4550-4554.

28. Warner, J. H.; Rubinsztein-Dunlop, H.; Tilley, R. D., Surface morphology dependent photoluminescence from colloidal silicon nanocrystals. *Journal of Physical Chemistry B* **2005**, *109*, 19064-19067.

29. Sun, G., Intersub band approach to silicon based lasers-circumventing the indirect bandgap limitation. *Advances in Optics and Photonics* **2011**, *3*, 53-87.

30. Shirahata, N.; Hasegawa, T.; Sakka, Y.; Tsuruoka, T., Size-Tunable uv-luminescent silicon nanocrystals. *Small* **2010**, *6*, 915-921.

31. Holmes, J. D.; Ziegler, K. J.; Doty, R. C.; Pell, L. E.; Johnston, K. P.; Korgel, B. A., Highly luminescent silicon nanocrystals with discrete optical transitions. *Journal of the American Chemical Society* **2001**, *123*, 3743-3748.

32. Canham, L. T., Silicon quantum wire array fabrication by electrochemical and chemical dissolution of wafers. *Applied Physics Letters* **1990**, *57*, 1046-1048.

33. Wolkin, M. V.; Jorne, J.; Fauchet, P. M.; Allan, G.; Delerue, C., Electronic states and luminescence in porous silicon quantum dots: the role of oxygen. *Physical Review Letters* **1999**, *82*, 197-200.

34. Kang, Z.; Liu, Y.; Tsang, C. H. A.; Ma, D. D. D.; Fan, X.; Wong, N. B.; Lee, S. T., Water-Soluble silicon quantum dots with wavelength-tunable photoluminescence. *Advanced Materials* **2009**, *21*, 661-664.

35. Belomoin, G.; Therrien, J.; Smith, A.; Rao, S.; Twesten, R.; Chaieb, S.; Nayfeh, M. H.; Wagner, L.; Mitas, L., Observation of a magic discrete family of ultrabright Si nanoparticles. *Applied Physics Letters* **2002**, *80*, 841-843.

36. Heinrich JL, C. C., Credo GM, Sailor MJ, Kavanagh KL., Luminescent colloidal silicon suspensions from porous silicon. *Science* **1992**, *255*, 66-68.

37. Sato, K.; Tsuji, H.; Hirakuri, K.; Fukata, N.; Yamauchi, Y., Controlled chemical etching for silicon nanocrystals with wavelength-tunable photoluminescence. *Chemical Communications* **2009**, 3759-3761.

38. Cichos, F.; Martin, J.; von Borczyskowski, C., Emission intermittency in silicon nanocrystals. *Physical Review B* **2004**, *70*, 115314.

39. Valenta, J.; Janda, P.; Dohnalová, K.; Nižňansky, D.; Vácha, F.; Linnros, J., Colloidal suspensions of silicon nanocrystals: from single nanocrystals to photonic structures. *Optical Materials* **2005**, *27*, 1046-1049.

40. Furukawa, S.; Miyasato, T., Quantum size effects on the optical band gap of microcrystalline Si:H. *Physical Review B* **1988**, *38*, 5726-5729.

41. Schoenfeld, O.; Zhao, X.; Christen, J.; Hempel, T.; Nomura, S.; Aoyagi, Y., Formation of Si quantum dots in nanocrystalline silicon. *Solid-State Electronics* **1996**, *40*, 605-608.

42. Liu, S.M.; Sato, S.; Kimura, K., Synthesis of Luminescent Silicon Nanopowders Redispersible to Various Solvents. *Langmuir* **2005**, *21*, 6324-6329.

43. Kapaklis, V.; Politis, C.; Poulopoulos, P.; Schweiss, P., Photoluminescence from silicon nanoparticles prepared from bulk amorphous silicon monoxide by the disproportionation reaction. *Applied Physics Letters* **2005**, *87*, 123114-3.

44. Littau, K. A.; Szajowski, P. J.; Muller, A. J.; Kortan, A. R.; Brus, L. E., A luminescent silicon nanocrystal colloid *via* a high-temperature aerosol reaction. *Journal of Physical Chemistry* **1993**, *97*, 1224-1230.

45. Fojtik, A.; Henglein, A., Luminescent colloidal silicon particles. *Chemical Physics Letters* **1994**, *221*, 363-367.

46. English, D. S.; Pell, L. E.; Yu, Z.; Barbara, P. F.; Korgel, B. A., Size Tunable Visible Luminescence from Individual Organic Monolayer Stabilized Silicon Nanocrystal Quantum Dots. *Nano Letters* **2002**, *2*, 681-685.

47. Hessel, C. M.; Henderson, E. J.; Veinot, J. G. C., Hydrogen silsesquioxane: A molecular precursor for nanocrystalline Si-SiO_2 composites and freestanding hydride-surface-terminated silicon nanoparticles. *Chemistry of Materials* **2006**, *18*, 6139-6146.

48. Dinh, L. N.; Chase, L. L.; Balooch, M.; Siekhaus, W. J.; Wooten, F., Optical properties of passivated Si nanocrystals and SiO_x nanostructures. *Physical Review B* **1996**, *54*, 5029-5037.

49. van Buuren, T.; Dinh, L. N.; Chase, L. L.; Siekhaus, W. J.; Terminello, L. J., Changes in the Electronic Properties of Si Nanocrystals as a Function of Particle Size. *Physical Review Letters* **1998**, *80*, 3803-3806.

50. Kovalev, D.; Heckler, H.; Ben-Chorin, M.; Polisski, G.; Schwartzkopff, M.; Koch, F., Breakdown of the k-Conservation Rule in Si Nanocrystals. *Physical Review Letters* **1998**, *81*, 2803-2806.

51. Niu, H.J.; Zhang, L.; Zhu, J.Y.; Zhang, M.I.; Bai, X. D., High-yield synthesis of silicon nanoparticles *via* the perpendicular pulsed laser ablation in the inert gas. *Optoelectronics Letters* **2010**, *6*, 81-84.

52. Umezu, I.; Kondo, I.; Sugimura, A., Formation of surface stabilized Si nanocrystal by pulsed laser ablation in hydrogen gas. *Applied Physics A: Materials Science & Processing* **2008**, *93*, 717-720.

53. Shirahata, N.; Linford, M. R.; Furumi, S.; Pei, L.; Sakka, Y.; Gates, R. J.; Asplund, M. C., Laser-derived one-pot synthesis of silicon nanocrystals terminated with organic monolayers. *Chemical Communications* **2009**, 4684-4686.

54. Hata, K.; Yoshida, S.; Fujita, M.; Yasuda, S.; Makimura, T.; Murakami, K.; Shigekawa, H., Self-Assembled monolayer as a template to deposit silicon nanoparticles fabricated by laser ablation. *The Journal of Physical Chemistry B* **2001**, *105*, 10842-10846.

55. Li, X.; He, Y.; Talukdar, S. S.; Swihart, M. T., Process for Preparing Macroscopic Quantities of Brightly Photoluminescent Silicon Nanoparticles with Emission Spanning the Visible Spectrum. *Langmuir* **2003**, *19*, 8490-8496.

56. Li, X.; He, Y.; Swihart, M. T., Surface functionalization of silicon nanoparticles produced by laser-driven pyrolysis of silane followed by hf−hno_3 etching. *Langmuir* **2004**, *20*, 4720-4727.

57. Hua, F.; Swihart, M. T.; Ruckenstein, E., Efficient surface grafting of luminescent silicon quantum dots by photoinitiated hydrosilylation. *Langmuir* **2005**, *21*, 6054-6062.

58. Mangolini, L.; Thimsen, E.; Kortshagen, U., High-Yield plasma synthesis of luminescent silicon nanocrystals. *Nano Letters* **2005**, *5*, 655-659.

59. Giesen, B.; Wiggers, H.; Kowalik, A.; Roth, P., Formation of si-nanoparticles in a microwave reactor: Comparison between experiments and modelling. *Journal of Nanoparticle Research* **2005**, *7*, 29-41.

60. Sankaran, R. M.; Holunga, D.; Flagan, R. C.; Giapis, K. P., Synthesis of blue luminescent si nanoparticles using atmospheric-pressure microdischarges. *Nano Letters* **2005**, *5*, 537-541.

61. Mariotti, D.; Švrček, V.; Hamilton, J. W. J.; Schmidt, M.; Kondo, M., Silicon Nanocrystals in Liquid Media: Optical properties and surface stabilization by microplasma-induced non-equilibrium liquid chemistry. *Advanced Functional Materials* **2012**, *22*, 954-964.

62. Švrček, V.; Mariotti, D.; Kondo, M., Microplasma-induced surface engineering of silicon nanocrystals in colloidal dispersion. *Applied Physics Letters* **2010**, *97*,161052.

63. Wilcoxon, J. P.; Samara, G. A., Tailorable, visible light emission from silicon nanocrystals. *Applied Physics Letters* **1999**, *74*, 3164-3166.

64. Tilley, R. D.; Yamamoto, K., The microemulsion synthesis of hydrophobic and hydrophilic silicon nanocrystals. *Advanced Materials* **2006**, *18*, 2053-2056.

65. Rosso-Vasic, M.; Spruijt, E.; van Lagen, B.; De Cola, L.; Zuilhof, H., Alkyl-functionalized oxide-free silicon nanoparticles: synthesis and optical properties. *Small* **2008**, *4*, 1835-1841.

66. Wang, J.; Sun, S.; Peng, F.; Cao, L.; Sun, L., Efficient one-pot synthesis of highly photoluminescent alkyl-functionalised silicon nanocrystals. *Chemical Communications* **2011**, *47*, 4941-4943.

67. Cheng, X.; Gondosiswanto, R.; Ciampi, S.; Reece, P. J.; Gooding, J. J., One-pot synthesis of colloidal silicon quantum dots and surface functionalization *via* thiol-ene click chemistry. *Chemical Communications* **2012**, *48*, 11874-11876.

68. Mayeri, D.; Phillips, B. L.; Augustine, M. P.; Kauzlarich, S. M., nmr study of the synthesis of alkyl-terminated silicon nanoparticles from the reaction of $sicl_4$ with the zintl salt, nasi. *Chemistry of Materials* **2001**, *13*, 765-770.

69. Pettigrew, K. A.; Power, P. P.; Kauzlarich, S. M., Solution synthesis of alkyl-terminated silicon nanocrystals. *Abstracts of Papers of the American Chemical Society* **2003**, *225*, U75-U75.

70. Liu, Q.; Kauzlarich, S. M., A new synthetic route for the synthesis of hydrogen terminated silicon nanoparticles. *Materials Science and Engineering B-Solid State Materials for Advanced Technology* **2002**, *96*, 72-75.

71. Baldwin, R. K.; Pettigrew, K. A.; Ratai, E.; Augustine, M. P.; Kauzlarich, S. M., Solution reduction synthesis of surface stabilized silicon nanoparticles. *Chemical Communications* **2002**, 1822-1823.

72. Zhang, X.; Brynda, M.; Britt, R. D.; Carroll, E. C.; Larsen, D. S.; Louie, A. Y.; Kauzlarich, S. M., Synthesis and Characterization of Manganese-Doped Silicon Nanoparticles: Bifunctional paramagnetic-optical nanomaterial. *Journal of the American Chemical Society* **2007**, *129*, 10668-10669.

73. Baldwin, R. K.; Zou, J.; Pettigrew, K. A.; Yeagle, G. J.; Britt, R. D.; Kauzlarich, S. M., The preparation of a phosphorus doped silicon film from phosphorus containing silicon nanoparticles. *Chemical Communications* **2006**, 658-660.

74. Yang, C. S.; Kauzlarich, S. M.; Wang, Y. C., Synthesis and characterization of germanium/Si-alkyl and germanium/silica core-shell quantum dots. *Chemistry of Materials* **1999**, *11*, 3666-3670.

75. Hessel, C. M.; Henderson, E. J.; Veinot, J. G. C., Hydrogen Silsesquioxane: A molecular precursor for nanocrystalline $si{-}sio_2$ composites and freestanding hydride-surface-terminated silicon nanoparticles. *Chemistry of Materials* **2006**, *18*, 6139-6146.

76. Henderson, E. J.; Veinot, J. G. C., Synthesis of oxide encapsulated and freestanding hydride surface terminated $si_{1-x}ge_x$ nanocrystals. *Chemistry of Materials* **2007**, *19*, 1886-1888.

77. Baker, S. N.; Baker, G. A., Luminescent carbon nanodots: emergent nanolights. *Angewandte Chemie International Edition* **2010,** *49*, 6726-6744.

78. Li, H.; Kang, Z.; Liu, Y.; Lee, S. T., Carbon nanodots: synthesis, properties and applications. *Journal of Materials Chemistry* **2012**, *22*, 24230-24253.

79. Sun, Y. P.; Zhou, B.; Lin, Y.; Wang, W.; Fernando, K. A. S.; Pathak, P.; Meziani, M. J.; Harruff, B. A.; Wang, X.; Wang, H.; Luo, P. G.; Yang, H.; Kose, M. E.; Chen, B.; Veca, L. M.; Xie, S. Y., Quantum-Sized carbon dots for bright and colorful photoluminescence. *Journal of the American Chemical Society* **2006**, *128*, 7756-7757.

80. Yang, S. T.; Wang, X.; Wang, H.; Lu, F.; Luo, P. G.; Cao, L.; Meziani, M. J.; Liu, J. H.; Liu, Y.; Chen, M.; Huang, Y.; Sun, Y. P., Carbon Dots as nontoxic and high-performance fluorescence imaging agents. *The Journal of Physical Chemistry C* **2009**, *113*, 18110-18114.

81. Hu, S. L.; Niu, K. Y.; Sun, J.; Yang, J.; Zhao, N. Q.; Du, X. W., One-step synthesis of fluorescent carbon nanoparticles by laser irradiation. *Journal of Materials Chemistry* **2009**, *19*, 484-488.

82. Li, X.; Wang, H.; Shimizu, Y.; Pyatenko, A.; Kawaguchi, K.; Koshizaki, N., Preparation of carbon quantum dots with tunable photoluminescence by rapid laser passivation in ordinary organic solvents. *Chemical Communications* **2011**, *47*, 932-934.

83. Xu, X.; Ray, R.; Gu, Y.; Ploehn, H. J.; Gearheart, L.; Raker, K.; Scrivens, W. A., Electrophoretic analysis and purification of fluorescent single-walled carbon nanotube fragments. *Journal of the American Chemical Society* 2004, *126*, 12736-12737.

84. Zhou, J.; Booker, C.; Li, R.; Zhou, X.; Sham, T. K.; Sun, X.; Ding, Z., An electrochemical avenue to blue luminescent nanocrystals from multiwalled carbon nanotubes (MWCNTS). *Journal of the American Chemical Society* **2007**, *129*, 744-745.

85. Zheng, L.; Chi, Y.; Dong, Y.; Lin, J.; Wang, B., Electrochemiluminescence of water-soluble carbon nanocrystals released electrochemically from graphite. *Journal of the American Chemical Society* **2009**, *131*, 4564-4565.

86. Li, Y.; Hu, Y.; Zhao, Y.; Shi, G.; Deng, L.; Hou, Y.; Qu, L., An electrochemical avenue to green-luminescent graphene quantum dots as potential electron-acceptors for photovoltaics. *Advanced Materials* **2011**, *23*, 776-780.

87. Gokus, T.; Nair, R. R.; Bonetti, A.; Böhmler, M.; Lombardo, A.; Novoselov, K. S.; Geim, A. K.; Ferrari, A. C.; Hartschuh, A., Making graphene luminescent by oxygen plasma treatment. *ACS Nano* **2009**, *3*, 3963-3968.

88. Jiang, H.; Chen, F.; Lagally, M. G.; Denes, F. S., New strategy for synthesis and functionalization of carbon nanoparticles. *Langmuir* **2009**, *26*, 1991-1995.

89. Pan, D.; Zhang, J.; Li, Z.; Wu, M., Hydrothermal route for cutting graphene sheets into blue-luminescent graphene quantum dots. *Advanced Materials* **2010**, *22*, 734-738.

90. Zhang, B.; Liu, C.Y.; Liu, Y., A Novel one-step approach to synthesize fluorescent carbon nanoparticles. *European Journal of Inorganic Chemistry* **2010**, 4411-4414.

91. Yang, Z. C.; Wang, M.; Yong, A. M.; Wong, S. Y.; Zhang, X. H.; Tan, H.; Chang, A. Y.; Li, X.; Wang, J., Intrinsically fluorescent carbon dots with tunable emission derived from hydrothermal treatment of glucose in the presence of monopotassium phosphate. *Chemical Communications* **2011**, *47*, 11615-11617.

92. Zhu, S.; Meng, Q.; Wang, L.; Zhang, J.; Song, Y.; Jin, H.; Zhang, K.; Sun, H.; Wang, H.; Yang, B., Highly Photoluminescent carbon dots for multicolor patterning, sensors, and bioimaging. *Angewandte Chemie International Edition* **2013**, *52*, 3953-3957.

93. Lu, W.; Qin, X.; Liu, S.; Chang, G.; Zhang, Y.; Luo, Y.; Asiri, A. M.; Al-Youbi, A. O.; Sun, X., Economical, green synthesis of fluorescent carbon nanoparticles and their use as probes for sensitive and selective detection of mercury(ii) ions. *Analytical Chemistry* **2012**, *84*, 5351-5357.

94. Sahu, S.; Behera, B.; Maiti, T. K.; Mohapatra, S., Simple one-step synthesis of highly luminescent carbon dots from orange juice: application as excellent bio-imaging agents. *Chemical Communications* **2012**, *48*, 8835-8837.

95. Huang, H.; Lv, J. J.; Zhou, D. L.; Bao, N.; Xu, Y.; Wang, A. J.; Feng, J. J., One-pot green synthesis of nitrogen-doped carbon nanoparticles as fluorescent probes for mercury ions. *RSC Advances* **2013**, *3*, 21691-21696.

96. Zhu, C.; Zhai, J.; Dong, S., Bifunctional fluorescent carbon nanodots: green synthesis *via* soy milk and application as metal-free electrocatalysts for oxygen reduction. *Chemical Communications* **2012**, *48*, 9367-9369.

97. Qin, X.; Lu, W.; Asiri, A. M.; Al-Youbi, A. O.; Sun, X., Green, low-cost synthesis of photoluminescent carbon dots by hydrothermal treatment of willow bark and their application as an effective photocatalyst for fabricating Au nanoparticles-reduced graphene oxide nanocomposites for glucose detection. *Catalysis Science & Technology* **2013**, *3*, 1027-1035.

98. Zhu, H.; Wang, X.; Li, Y.; Wang, Z.; Yang, F.; Yang, X., Microwave synthesis of fluorescent carbon nanoparticles with electrochemiluminescence properties. *Chemical Communications* **2009**, 5118-5120.

99. Wang, Q.; Zheng, H.; Long, Y.; Zhang, L.; Gao, M.; Bai, W., Microwave–hydrothermal synthesis of fluorescent carbon dots from graphite oxide. *Carbon* **2011**, *49*, 3134-3140.

100. Philippidis, A.; Stefanakis, D.; Anglos, D.; Ghanotakis, D., Microwave heating of arginine yields highly fluorescent nanoparticles. *Journal of Nanoparticle Research* **2013**, *15*, 1-9.

101. Liu, S.; Wang, L.; Tian, J.; Zhai, J.; Luo, Y.; Lu, W.; Sun, X., Acid-driven, microwave-assisted production of photoluminescent carbon nitride dots from N,N-dimethylformamide. *RSC Advances* **2011**, *1*, 951-953.

102. Xiao, D.; Yuan, D.; He, H.; Lu, J., Microwave-assisted one-step green synthesis of amino-functionalized fluorescent carbon nitride dots from chitosan. *Luminescence* **2013**, *28*, 612-615.

103. Qu, S.; Wang, X.; Lu, Q.; Liu, X.; Wang, L., A biocompatible fluorescent ink based on water-soluble luminescent carbon nanodots. *Angewandte Chemie International Edition* **2012**, *51*, 12215-12218.

104. Chen, P. C.; Chen, Y. N.; Hsu, P. C.; Shih, C. C.; Chang, H. T., Photoluminescent organosilane-functionalized carbon dots as temperature probes. *Chemical Communications* **2013**, *49*, 1639-1641.

105. Hsu, P.C.; Chang, H.T., Synthesis of high-quality carbon nanodots from hydrophilic compounds: role of functional groups. *Chemical Communications* **2012**, *48*, 3984-3986.

106. Sun, W.; Du, Y.; Wang, Y., Study on fluorescence properties of carbogenic nanoparticles and their application for the determination of ferrous succinate. *Journal of Luminescence* **2010**, *130*, 1463-1469.

107. Liao, B.; Long, P.; He, B.; Yi, S.; Ou, B.; Shen, S.; Chen, J., Reversible fluorescence modulation of spiropyran-functionalized carbon nanoparticles. *Journal of Materials Chemistry C* **2013**, *1*, 3716-3721.

108. Liu, Y.; Liu, C. Y.; Zhang, Z.Y., Synthesis and surface photochemistry of graphitized carbon quantum dots. *Journal of Colloid and Interface Science* **2011**, *356*, 416-421.

109. Tian, L.; Song, Y.; Chang, X.; Chen, S., Hydrothermally enhanced photoluminescence of carbon nanoparticles. *Scripta Materialia* **2010**, *62*, 883-886.

110. Zhang, Y. Q.; Ma, D. K.; Zhuang, Y.; Zhang, X.; Chen, W.; Hong, L. L.; Yan, Q. X.; Yu, K.; Huang, S. M., One-pot synthesis of N-doped carbon dots with tunable luminescence properties. *Journal of Materials Chemistry* **2012**, *22*, 16714-16718.

111. Zhou, J.; Lin, P.; Ma, J.; Shan, X.; Feng, H.; Chen, C.; Chen, J.; Qian, Z., Facile synthesis of halogenated carbon quantum dots as an important intermediate for surface modification. *RSC Advances* **2013**, *3*, 9625-9628.

112. Liang, Q.; Ma, W.; Shi, Y.; Li, Z.; Yang, X., Easy synthesis of highly fluorescent carbon quantum dots from gelatin and their luminescent properties and applications. *Carbon* **2013**, *60*, 421-428.

113. Wu, D.; Huang, X.; Deng, X.; Wang, K.; Liu, Q., Preparation of photoluminescent carbon nanodots by traditional Chinese medicine and application as a probe for Hg^{2+}. *Analytical Methods* **2013**, *5*, 3023-3027.

114. Wang, Q.; Huang, X.; Long, Y.; Wang, X.; Zhang, H.; Zhu, R.; Liang, L.; Teng, P.; Zheng, H., Hollow luminescent carbon dots for drug delivery. *Carbon* **2013**, *59*, 192-199.

115. Qu, K.; Wang, J.; Ren, J.; Qu, X., Carbon dots prepared by hydrothermal treatment of dopamine as an effective fluorescent sensing platform for the label-free detection of iron(III) ions and dopamine. *Chemistry – A European Journal* **2013**, *19*, 7243-7249.

116. Wu, H.; Mi, C.; Huang, H.; Han, B.; Li, J.; Xu, S., Solvothermal synthesis of green-fluorescent carbon nanoparticles and their application. *Journal of Luminescence* **2012**, *132*, 1603-1607.

117. De, B.; Karak, N., A green and facile approach for the synthesis of water soluble fluorescent carbon dots from banana juice. *RSC Advances* **2013**, *3*, 8286-8290.

118. Liu, S.; Tian, J.; Wang, L.; Luo, Y.; Zhai, J.; Sun, X., Preparation of photoluminescent carbon nitride dots from CCl_4 and 1,2-ethylenediamine: a heat-treatment-based strategy. *Journal of Materials Chemistry* **2011**, *21*, 11726-11729.

119. Jaiswal, A.; Ghosh, S. S.; Chattopadhyay, A., One step synthesis of C-dots by microwave mediated caramelization of poly(ethylene glycol). *Chemical Communications* **2012**, *48*, 407-409.

120. Nagaprasad, P.; Kumar, B. N. P.; Suraj, K.; Himani, K.; Mahitosh, M.; Amita, P., Synthesis of biocompatible multicolor luminescent carbon dots for bioimaging applications. *Science and Technology of Advanced Materials* **2012**, *13*, 045008.

121. Wang, X.; Qu, K.; Xu, B.; Ren, J.; Qu, X., Microwave assisted one-step green synthesis of cell-permeable multicolor photoluminescent carbon dots without surface passivation reagents. *Journal of Materials Chemistry* **2011**, *21*, 2445-2450.

122. Na, N.; Liu, T.; Xu, S.; Zhang, Y.; He, D.; Huang, L.; Ouyang, J., Application of fluorescent carbon nanodots in fluorescence imaging of human serum proteins. *Journal of Materials Chemistry B* **2013**, *1*, 787-792.

123. Du, F.; Zeng, F.; Ming, Y.; Wu, S., Carbon dots-based fluorescent probes for sensitive and selective detection of iodide. *Microchimica Acta* **2013**, *180*, 453-460.

124. Zhang, P.; Li, W.; Zhai, X.; Liu, C.; Dai, L.; Liu, W., A facile and versatile approach to biocompatible fluorescent polymers from polymerizable carbon nanodots. *Chemical Communications* **2012**, *48*, 10431-10433.

125. Jiang, J.; He, Y.; Li, S.; Cui, H., Amino acids as the source for producing carbon nanodots: microwave assisted one-step synthesis, intrinsic photoluminescence property and intense chemiluminescence enhancement. *Chemical Communications* **2012**, *48*, 9634-9636.

126. Liu, S.; Tian, J.; Wang, L.; Luo, Y.; Sun, X., A general strategy for the production of photoluminescent carbon nitride dots from organic amines and their application as novel peroxidase-like catalysts for colorimetric detection of H_2O_2 and glucose. *RSC Advances* **2012**, *2*, 411-413.

127. Liu, C.; Zhang, P.; Tian, F.; Li, W.; Li, F.; Liu, W., One-step synthesis of surface passivated carbon nanodots by microwave assisted pyrolysis for enhanced multicolor photoluminescence and bioimaging. *Journal of Materials Chemistry* **2011**, *21*, 13163-13167.

128. Chandra, S.; Pathan, S. H.; Mitra, S.; Modha, B. H.; Goswami, A.; Pramanik, P., Tuning of photoluminescence on different surface functionalized carbon quantum dots. *RSC Advances* **2012**, *2*, 3602-3606.

129. Safavi, A.; Sedaghati, F.; Shahbaazi, H.; Farjami, E., Facile approach to the synthesis of carbon nanodots and their peroxidase mimetic function in azo dyes degradation. *RSC Advances* **2012**, *2*, 7367-7370.

130. Mitra, S.; Chandra, S.; Kundu, T.; Banerjee, R.; Pramanik, P.; Goswami, A., Rapid microwave synthesis of fluorescent hydrophobic carbon dots. *RSC Advances* **2012**, *2*, 12129-12131.

131. Chandra, S.; Das, P.; Bag, S.; Laha, D.; Pramanik, P., Synthesis, functionalization and bioimaging applications of highly fluorescent carbon nanoparticles. *Nanoscale* **2011**, *3*, 1533-1540.

132. Liu, R.; Wu, D.; Liu, S.; Koynov, K.; Knoll, W.; Li, Q., An aqueous route to multicolor photoluminescent carbon dots using silica spheres as carriers. *Angewandte Chemie International Edition* **2009**, *48*, 4598-4601.

133. Bourlinos, A. B.; Stassinopoulos, A.; Anglos, D.; Zboril, R.; Georgakilas, V.; Giannelis, E. P., Photoluminescent carbogenic dots. *Chemistry of Materials* **2008**, *20*, 4539-4541.

134. Zong, J.; Zhu, Y.; Yang, X.; Shen, J.; Li, C., Synthesis of photoluminescent carbogenic dots using mesoporous silica spheres as nanoreactors. *Chemical Communications* **2011**, *47*, 764-766.

135. Kwon, W.; Rhee, S. W., Facile synthesis of graphitic carbon quantum dots with size tunability and uniformity using reverse micelles. *Chemical Communications* **2012**, *48*, 5256-5258.

136. Kwon, W.; Lee, G.; Do, S.; Joo, T.; Rhee, S.W., Size-Controlled soft-template synthesis of carbon nanodots toward versatile photoactive materials. *Small* **2014**, *10*, 506-513.

137. Bhunia, S. K.; Saha, A.; Maity, A. R.; Ray, S. C.; Jana, N. R., Carbon nanoparticle-based fluorescent bioimaging probes. *Scientific Reports* **2013**, *3*. 01473.

138. Forstner, U.; Wittmann, G.T.W., Metal pollution in the aquatic environment. *Springer* **1981**.

139. Merian, E., Metals and their compounds in the environment. *VCH, Weinheim* **1991**.

140. Fresenius, W.: Quentin. K. E.; Schneider, W., Water analysis. *Springer, Berlin* **1988**.

141. Klockenkämpfer, R., Total-Reflection x-ray fluorescence analysis. *Wiley, New York* **1997**.

142. Spichiger-Keller, U. E.; Chemical Sensors and Biosensors for Medical and Biological Applications. *Wiley-VHC, Weinheim* **1998**.

143. Wu, P.; Zhao, T.; Wang, S.; Hou, X., Semicondutor quantum dots-based metal ion probes. *Nanoscale* **2014**, *6*, 43-64.

144. Cheng, X.; Lowe, S. B.; Reece, P. J.; Gooding, J. J., Colloidal silicon quantum dots: from preparation to the modification of self-assembled monolayers (SAMs) for bio-applications. *Chemical Society Reviews* **2014**, *43*, 2680-2700.

145. Teste, B.; Malloggi, F.; Gassner, A.L.; Georgelin, T.; Siaugue, J.M.; Varenne, A.; Girault, H.; Descroix, S., Magnetic core shell nanoparticles trapping in a

microdevice generating high magnetic gradient. *Lab on a Chip* **2011**, *11*, 833-840.

146. Chen, Y.; Rosenzweig, Z., Luminescent cds quantum dots as selective ion probes. *Analytical Chemistry* **2002**, *74*, 5132-5138.

147. Zhang, J.; Yu, S.H., Highly photoluminescent silicon nanocrystals for rapid, label-free and recyclable detection of mercuric ions. *Nanoscale* **2014**, *6*, 4096-4101.

148. Shi, J.; Lu, C.; Yan, D.; Ma, L., High selectivity sensing of cobalt in HepG2 cells based on necklace model microenvironment-modulated carbon dot-improved chemiluminescence in Fenton-like system. *Biosensors and Bioelectronics* **2013**, *45*, 58-64.

149. Mohd Yazid, S.; Chin, S.; Pang, S.; Ng, S., Detection of Sn(II) ions *via* quenching of the fluorescence of carbon nanodots. *Microchimica* Acta **2013**, *180*, 137-143.

150. Wee, S. S.; Ng, Y. H.; Ng, S. M., Synthesis of fluorescent carbon dots *via* simple acid hydrolysis of bovine serum albumin and its potential as sensitive sensing probe for lead (II) ions. *Talanta* **2013**, *116*, 71-76.

151. Zhang, Y. L.; Wang, L.; Zhang, H. C.; Liu, Y.; Wang, H. Y.; Kang, Z. H.; Lee, S.T., Graphitic carbon quantum dots as a fluorescent sensing platform for highly efficient detection of Fe^{3+} ions. *RSC Advances* **2013**, *3*, 3733-3738.

152. Shao, X.; Gu, H.; Wang, Z.; Chai, X.; Tian, Y.; Shi, G., Highly selective electrochemical strategy for monitoring of cerebral Cu^{2+} based on a carbon dot-tpea hybridized surface. *Analytical Chemistry* **2012**, *85*, 418-425.

153. Zhu, A.; Qu, Q.; Shao, X.; Kong, B.; Tian, Y., Carbon-Dot-based dual-emission nanohybrid produces a ratiometric fluorescent sensor for in vivo imaging of cellular copper ions. *Angewandte Chemie International Edition* **2012**, *51*, 7185-7189.

154. Qu, Q.; Zhu, A.; Shao, X.; Shi, G.; Tian, Y., Development of a carbon quantum dots-based fluorescent Cu^{2+} probe suitable for living cell imaging. *Chemical Communications* **2012**, *48*, 5473-5475.

155. Zhou, L.; Lin, Y.; Huang, Z.; Ren, J.; Qu, X., Carbon nanodots as fluorescence probes for rapid, sensitive, and label-free detection of Hg^{2+} and biothiols in complex matrices. *Chemical Communications* **2012**, *48*, 1147-1149.

156. Guo, Y.; Wang, Z.; Shao, H.; Jiang, X., Hydrothermal synthesis of highly fluorescent carbon nanoparticles from sodium citrate and their use for the detection of mercury ions. *Carbon* **2013**, *52*, 583-589.

157. Mohamed Ali, E.; Zheng, Y.; Yu, H.H.; Ying, J. Y., Ultrasensitive Pb^{2+} detection by glutathione-capped quantum dots. *Analytical Chemistry* **2007**, *79*, 9452-9458.

158. Isarov, A. V.; Chrysochoos, J., Optical and Photochemical properties of nonstoichiometric cadmium sulfide nanoparticles: Surface modification with copper(II) ions. *Langmuir* **1997**, *13*, 3142-3149.

159. Ge, S.; Zhang, C.; Zhu, Y.; Yu, J.; Zhang, S., BSA activated CdTe quantum dot nanosensor for antimony ion detection. *Analyst* **2010**, *135*, 111-115.

160. Sui, C.X.; Liu, Y.F.; Li, P.A.; Zhang, D.; Xia, F., Determination of IO^{4-} and Ni^{2+} ions using l-cysteine-CdTe/ZnS quantum dots as pH-dependent fluorescent probes. *Analytical Methods* **2013**, *5*, 1695-1701.

161. Lakowicz J.R., Principles of fluorescence specroscopy. *Springer* **2006**.

Chapter 2

Synthesis and Characterisation of Silicon Nanocrystals

2.1 Introduction

Semiconductor nanocrystals (NCs) or quantum dots have been extensively studied over the last 25 years since their size-dependent optical and electronic properties make them useful materials in applications ranging from biological imaging to optoelectronic devices.[1-4] Since the first reports in the late 1980s,[5] a wide range of semiconductor materials have been prepared in nanocrystal form. To date much emphasis has focused on exclusively group II-VI, III-V, and IV-VI compounds.[6] In particular, II-VI and IV-VI have been shown to demonstrate tunable electroluminescence across both the visible and infrared section of the electromagnetic spectrum. In recent times, group IV materials such as silicon have received a great deal of attention as new functional material with unique physical/chemical properties that are unseen in the bulk form.

While bulk silicon is known to be a poor light emitter due to its indirect band gap, silicon nanocrystals (Si NCs) have exhibited enhanced photo- and electro-luminescence properties due to quantum confinement effects.[7-10] These properties can be readily tuned by manipulating the nanocrystal diameter and through surface chemical functionalisation. The level of control over the materials photophysical and optoelectronic properties that is possible using solution-phase chemical synthetic routes allows for applications in chemical and biological sensors,[11, 12] and exploited as effective building blocks for the fabrication of novel functional devices, such as light-emitting devices.[13-18] Si NCs exhibit low toxicity, excellent photostability, biocompatibility, strong fluorescence and high quantum yields.

Despite the great potential of these materials, size and shape control is not nearly as well developed for group IV nanocrystals as for binary III-V, II-VI and IV-VI semiconductors. Fine tuning of the nanocrystal size and shape would facilitate advances in the study of the photophysical properties associated with Si NCs. In particular, development of synthetic protocols to reliably control sizes in the 2-6 nm range is necessary to understand their quantum confinement behaviour and evaluate their efficacy in applications ranging from bioimaging to optoelectronic devices. In this chapter[†], Si NCs with well-defined core diameters (d) in the range 1 nm < d < 6 nm have been prepared using inert atmospheric synthetic methods. Since it is of key importance for applications that the nanocrystals are uniform in size, efforts focused on

the development of routes that produced highly quality nanocrystals with standard deviations ($\sigma = \Delta d/d$) of less than 10 %. The diameters of the as-synthesised Si NCs were controlled *via* variation of the ratio of Si precursors to the capping ligands, surfactants, addition rate as well as use of reducing agents of different strengths. As a result a library of size tunable Si NCs were established and ready to be incorporated into a number of different applications as the emissive material. Once the necessary small scale routes had been developed, efforts focused on scaling up the processing steps to achieve large scale (> 100 mg) production of silicon nanocrystals.

† Publications arising from this work are:

(i) "Size Controlled Synthesis of Silicon Nanocrystals using Cationic Surfactant Templates," *Small* 2014, 10, 564-590.

(ii) "Silicon nanocrystals: Novel synthesis routes for photovoltaic applications," *Physica Status Solidi (a)* 2013, 210, 649.

(iii) "Indium tin oxide-silicon nanocrystal nanocomposite grown by aerosol assisted chemical vapour deposition, journal of Sol-Gel Science and Technology 2015, DOI 10.1007/s10971-015-3618-3.

(iv) "Light emission from large area, robust, three-dimensional silicon-silica inverse opals fabricated by colloidal crystal templating," *Journal of Materials Chemistry C* 2014, 2, 1675-1682.

(v) "Size Controlled Synthesis of Silicon Nanocrystals within Inverse Micelles Templates," *Material Research Society Symposium Proceedings* 2013, 1546, mrss13-1546-11506-1548.

(vi) "Synthesis and Compositional Control of Size Monodisperse Si_xGe_{1-x} Nanocrystals for Optoelectronic Applications," *Material Research Society Symposium Proceedings* 2013, 1551, mrss13-1551-r02-03.

2.2 Experimental

2.2.1 Synthesis and Purification of Silicon Nanocrystals

All reagents and solvents were purchased from Sigma-Aldrich Ltd. and used as received. All glassware used was cleaned by thoroughly soaking in a base bath overnight, followed by immersion in piranha solution (3:1 concentrated sulphuric acid: 30 % hydrogen peroxide) for 20 min. The synthesis of the silicon nanocrystals was adapted from the method reported by Tilley and co-workers, see Scheme 2.1.[19] All reactions were carried out in an inert atmosphere glove-box. For example, for the synthesis of Si NCs using cationic surfactant templates, 2.74 mmol of the surfactant was dissolved in 100 mL anhydrous toluene. 0.1 mL (0.87 mmol) $SiCl_4$ was then added to the solution and left to stir for 30 min. Silicon nanocrystals were formed by the dropwise addition of 6 mL of 1 M lithium aluminium hydride in THF over a period of 2 min. CAUTION: Small amounts of silane gas, which is pyrophoric, could be evolved at this stage of the reaction and care should be taken to prevent exposure to air.[20]

The solution was then left to react for 2.5 h. The excess reducing agent was then quenched with the addition of 60 mL methanol, upon which the dispersion became transparent. At this stage of the reaction the Si NCs are terminated by hydrogen and encapsulated within the inverse micelle. Chemically passivated nanocrystals were formed by modifying the silicon-hydrogen bonds at the surface *via* the addition of 200 µL of a 0.1 M H_2PtCl_6 in isopropyl alcohol as a catalyst, followed by 6 mL of 1-heptene. After stirring for 2.5 h, the Si NCs were removed from the glove box and the organic solvent removed by rotary evaporation. The resulting dry powder (consisting mainly of surfactant) was then redispersed in 20 mL hexane and sonicated for 30 min. The solution was then filtered twice using PVDF membrane filters (MILLEX-HV, Millipore, 0.45 µm) to remove the surfactant, after which it was washed with 100 mL of n-methyl formamide (4 times) and then with deionsed water (DI).

Alkyl-terminated Si NCs remain in the hexane phase. The Si NCs were further purified by chromatography. The solution was concentrated down to 1 mL and put into the column (ø =1 cm, 41.0 cm). Sephadex gel LH-20 was used as the stationary phase and eluted with THF. Fractions were collected every 50 drops at a flow rate of one drop every 5 s. A hand held UV lamp (365 nm) was used to check each fraction for Si NCs

luminescence. The fractions were then combined and concentrated down to 1 mL. In addition to synthesizing heptane capped Si NCs, amine terminated Si NCs were synthesized in a similar manner and the resulting Si NCs were dispersed in deionized water. The amine terminated Si NCs were purified by filtering through PVDF membrane filters and column purified using the stationary phase described above and deionized water as the eluent. Overall the synthesis allows for the Si NCs to be dispersed in a variety of polar and non-polar solvents. Table 2.1 shows a summary of the reactions studied in this work and the various synthetic parameters used for the formation of Si NCs.

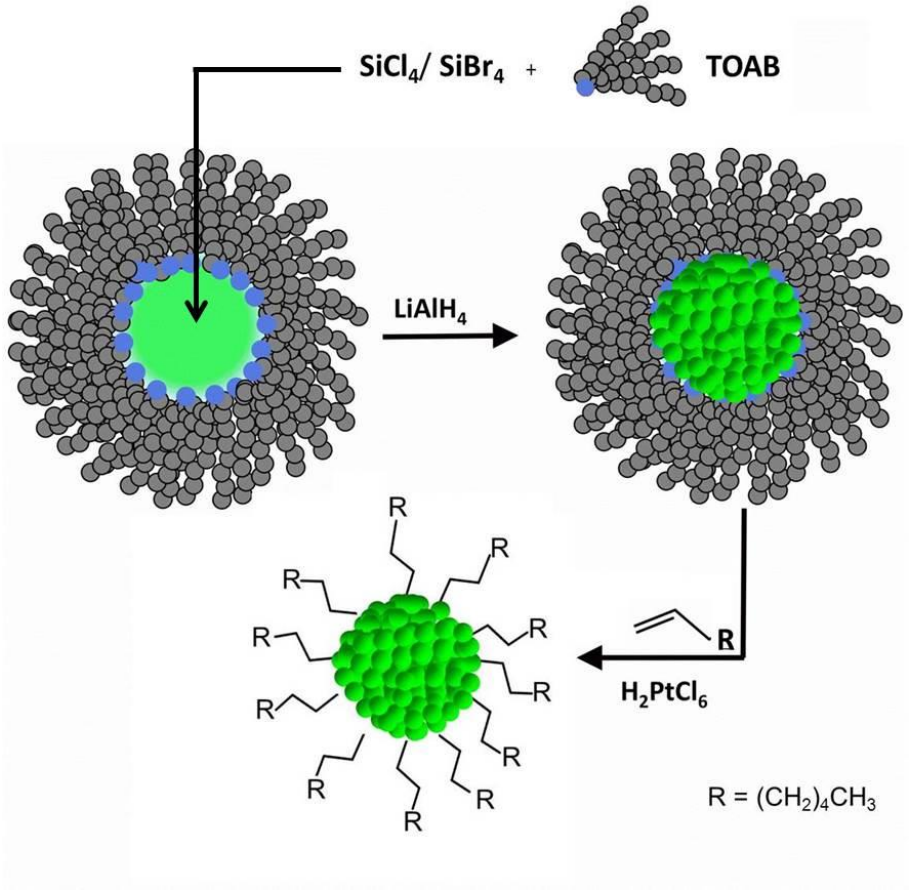

Scheme 2.1. Synthesis of Heptane terminated silicon NCs.

2.2.2 Optical Characterization

Ultraviolet-Visible (UV-Vis) absorption spectra were recorded using a Shimadzu UV PC-2401 spectrophotometer equipped with a 60 mm integrating sphere (ISR- 240A, Shimadzu). Absorption spectra were recorded at room temperature using a quartz cuvette (1 cm) and corrected for the solvent absorption. The cuvette was washed at least twice each with acetone, methanol, DI water and the solvent to be used prior to measurements.

Photoluminescence spectra (PL) of the Si NCs were recorded using a Perkin Elmer LS 50 luminescence spectrophotometer equipped with a pulsed Xenon discharge lamp. An excitation slit width of 10 nm, emission slit width of 2.5 nm and a scan speed of 1000 nm/min was used. Samples were measured directly in a quartz fluorescence cuvette with 4 polished sides, a path length of 10 mm and a volume of 3.5 mL. The cuvette was thoroughly washed at least twice with acetone, methanol, deionised water and the solvent to be used before measurements. The spectra were corrected by measuring emission from the solvent and then subtracting this from the samples.

Quantum yields (QY) were measured using the comparative method described by Williams *et al.*[21] Dilute dispersions of the alkyl terminated Si NCs in hexane were prepared with optical densities between 0.01-0.1 and compared against aqueous tryptophan solutions with similar optical densities as reference emitters. The quantum yield of the tryptophan reference was corrected for temperature using the model described by Robbins *et al.*, see Section 2.3.1.[22] PL spectra of all the Si NCs and tryptophan solutions were acquired using an excitation wavelength of 280 nm, and the total PL intensity integrated over 300-475 nm. Linear regression analysis was employed to determine the relative PL intensities of the sample and reference solutions over the range of concentrations, allowing the quantum yield of the Si NCs. The quantum yields were then calculated using the Equation 2.1:

$$\Phi_x = \Phi_R \left(\frac{m_x}{m_R} \right) \left(\frac{\eta_x^2}{\eta_R^2} \right) \qquad (2.1)$$

Where Φ is the quantum yield, m is the slope from the plot of integrated fluorescence intensity *versus* absorbance and η is the refractive index. The subscript R refers to the reference material of the known standard while x indicates the unknown species to be

calculated. The quantum yield of the amine-capped Si NCs was calculated using 9-10-diphenyl anthracene (literature quantum yield of 90 % at 320 nm) as the reference. [23]

Photoluminescence lifetime measurements were recorded on a scanning confocal fluorescence microscope (MicroTime 200, PicoQuant GmbH) equipped with a TimeHarp 200 TCSPC board. NC samples were excited using a 402 nm pulsed diode laser (10 MHz; 70 ps pulse duration, LDH-P-C-400) that was spectrally filtered using a 405 nm band-pass filter (Z405/10x, Chroma Technology Corp.). A 50X objective (0.5 NA; LM Plan FL, Olympus Corp.) was used for focusing the excitation light onto the NC dispersion and collecting the resultant fluorescence, which was directed onto an avalanche photodiode (APD; SPCM-AQR-14, Perkin-Elmer, Inc.). Backscattered excitation light was blocked with a 410 nm long-pass filter placed in the collection path (3RD410LP, Omega Optical). The excitation power was adjusted to maintain a count rate of $< 10^4$ counts/s at the APD in order to preserve single photon counting statistics. All emission lifetimes were fitted with a weighted multi-exponential model on FluoFit 4.2 software (PicoQuant GmbH). All lifetimes were fitted with a χ^2 value of less than 1.2.

Long-term PL stability measurements on the Alkyl capped Si NCs were carried out using an excitation wavelength of 280 nm, and recorded with a total integration time of 60 s. All spectra were integrated between 300 and 450 nm for comparison. For amine capped Si NCs stability measurements were carried out using an excitation wavelength of 320 nm, and recorded with a total integration time of 60 s. All spectra were integrated between 400 and 550 nm for comparison.

2.2.3 TEM, FTIR and XPS Characterisation

Transmission electron microscopy (TEM) images and selective area electron diffraction patterns (SAED) were acquired using a high-resolution JEOL 2100 electron microscope, equipped with a LAB_6 electron source and Gatan DualVision 600 Charge-Coupled Device (CCD), operating at an accelerating voltage of 200 keV. Energy dispersive x-ray spectra (EDX) spectra were recorded using an Oxford INCA x-sight detection spectrometer. Spectra were obtained from an area of the grid where there was a large amount of nanocrystals. A process time of 3-4 seconds was used and the spectra was obtained using an integration time of 40 s. TEM samples were prepared by depositing 300 μl of Si NC dispersion, onto a holey carbon coated TEM grid (400-mesh, #S147-3H, Agar Scientific). Particle size analysis of TEM images was carried out using the Particle Size Analyzer macro (r12, freely available online at http://code.google.com/p/psa-macro/) running on Image J software.

Fourier Transform Infrared Spectroscopy (FT-IR) spectra were recorded on a Bio Rad Excalibur FTS 3000 spectrometer in steps of 1 cm^{-1} and averaging 20 scans. Samples were formed by placing an aliquot of silicon crystals dispersed in hexane onto 32 mm round, 3 mm thick, drilled NaCl plates, after which the sample was allowed to evaporate to dryness. For amine terminated Si NCs, CaF_2 windows were used in the liquid cell.

X-ray photoelectron spectroscopy (XPS) measurements of the alkyl terminated Si NCs were carried out using a Kratos Axis-165 photoelectron spectrometer. The narrow scan spectra were obtained under high vacuum conditions by using a monochromatic Al Kα x-ray radiation at 15 kV and 10 mA with an analyzer pass energy of 20 eV. For amine terminated Si NCs a Kratos Ultra DLD photoelectron spectrometer was used with the parameters outlined above. Substrates were cleaned for 20 min in piranha solution, rinsed with water and dried with nitrogen. A few drops of the Si NC solution dissolved in chloroform were dropped on a clean gold surface substrate. All spectra were acquired at room temperature and binding energies were referenced to the Au $4f_{7/2}$ line. All spectra were corrected using a Shirley background.

Table 2.1. A list of the chemical reactions undertaken and the experimental parameters used for the formation of silicon nanocrystals.

Entry	Precursor	Surfactant	Solvent (anhydrous)	Reducing agent	Chemical Quencher (anhydrous)	Catalyst	Ligand
1	$SiCl_4$ (0.1 mL)	TOAB (1.5 g)	Toluene (100 mL)	1 M Lithium Aluminium Hydride in THF (6 mL)	Methanol (60 mL)	0.1 M Chloroplatinic acid in IPA (0.2 mL)	1-heptene (6 mL)
2	$SiCl_4$ (0.1 mL)	TBAB (0.9 g)	Toluene (100 mL)	1 M Lithium Aluminium Hydride in THF (6 mL)	Methanol (60 mL)	0.1 M Chloroplatinic acid in IPA (0.2 mL)	1-heptene (6 mL)
3	$SiCl_4$ (0.1 mL)	CTAB (1.0 g)	Toluene (100 mL)	1 M Lithium Aluminium Hydride in THF (6 mL)	Methanol (60 mL)	0.1 M Chloroplatinic acid in IPA (0.2 mL)	1-heptene (6 mL)
4	$SiCl_4$ (0.1 mL)	DDAB (1.3 g)	Toluene (100 mL)	1 M Lithium Aluminium Hydride in THF (6 mL)	Methanol (60 mL)	0.1 M Chloroplatinic acid in IPA (0.2 mL)	1-heptene (6 mL)
5	$SiCl_4$ (0.1 mL)	DTAB (0.8 g)	Toluene (100 mL)	1 M Lithium Aluminium Hydride in THF (6 mL)	Methanol (60 mL)	0.1 M Chloroplatinic acid in IPA (0.2 mL)	1-heptene (6 mL)
6	$SiCl_4$ (0.1 mL)	TDAB (2.1 g)	Toluene (100 mL)	1 M Lithium Aluminium Hydride in THF (6 mL)	Methanol (60 mL)	0.1 M Chloroplatinic acid in IPA (0.2 mL)	1-heptene (6 mL)

Table 2.1. (continued) A list of the chemical reactions undertaken and the experimental parameters used for the formation of silicon nanocrystals.

Entry	Precursor	Surfactant	Solvent (anhydrous)	Reducing agent	Chemical Quencher (anhydrous)	Catalyst	Ligand
7	$SiCl_4$ (0.1 mL)	C12E5 (1.1 g)	Hexane (100 mL)	1 M Lithium Aluminium Hydride in THF (6 mL)	Methanol (60 mL)	0.1 M Chloroplatinic acid in IPA (0.2 mL)	1-heptene (6 mL)
8	$SiCl_4$ (0.1 mL)	No surfactant	Toluene (100 mL)	1 M Lithium Aluminium Hydride in THF (6 mL)	Methanol (60 ml)	0.1 M Chloroplatinic acid in IPA (0.1 mL)	1-heptene (6 mL)
9	$SiBr_4$ (1.0 mL)	TOAB (1.5 g)	Toluene (100 mL)	1 M Lithium Aluminium Hydride in THF (6 mL)	Methanol (~ 60 mL)	0.1 M Chloroplatinic acid in IPA (0.1 mL	1-heptene (6 mL)
10	$SiCl_4$ (0.1 mL)	TOAB (1.5 g)	Toluene (100 mL)	1 M Lithium Aluminium Hydride in THF (2-3 mL)	Methanol (20ml)	0.1 M Chloroplatinic acid in IPA (0.1 mL	Allylamine (1.8 mL)
11	$SiCl_4$ (1.0 mL)	TOAB (3.0 g)	Toluene (100 mL)	1 M Lithium tri-sec-butylborohydride in THF (6 mL)	Methanol (~ 60 mL)	0.1 M Chloroplatinic acid in IPA (0.5 mL	Allylamine (4-5 mL)

$SiCl_4$ stands for silicon tetrachloride, $SiBr_4$ stands for silicon tetrabromide, TOAB stands for tetraoctylammoniumbromide, TBAB stands for tetrabutyl ammonium bromide, CTAB stands for cetyltrimethylammonium bromide. DDAB stands for didodecyldimethylammonium bromide, DTAB stands for dodecyltrimethylammonium bromide, TDAB stands for tetradodecylammonium bromide, mL stands for millilitre, M stands for Molar, THF stands for Tetrahydrofuran, g stands for gram, IPA stands for isopropyl alcohol, "~" stands for approximately.

2.3 Results and Discussion

2.3.1 Size Control Synthesis of Silicon Nanocrystals using Cationic Surfactants

Alkyl-terminated Si NCs were synthesized by room temperature reduction of silicon tetrachloride by lithium aluminium hydride under inert atmosphere; see Experimental Section 2.2.1 and Table 2.1 (entries 1-6) for further details. Figure 2.1 shows the chemical structures of the surfactants used in this study to form inverse micelles. Low magnification transmission electron microscope images of Si NCs prepared in the presence of the cationic quaternary ammonium salts tetraoctyl ammonium bromide (TOAB), tetrabutyl ammonium bromide (TBAB), cetyltrimethyl ammonium bromide (CTAB), didodecyldimethyl ammonium bromide (DDAB), dodecyltrimethyl ammonium bromide (DTAB) and tetradodecyl ammonium bromide (TDAB) are shown in Figure 2.2.

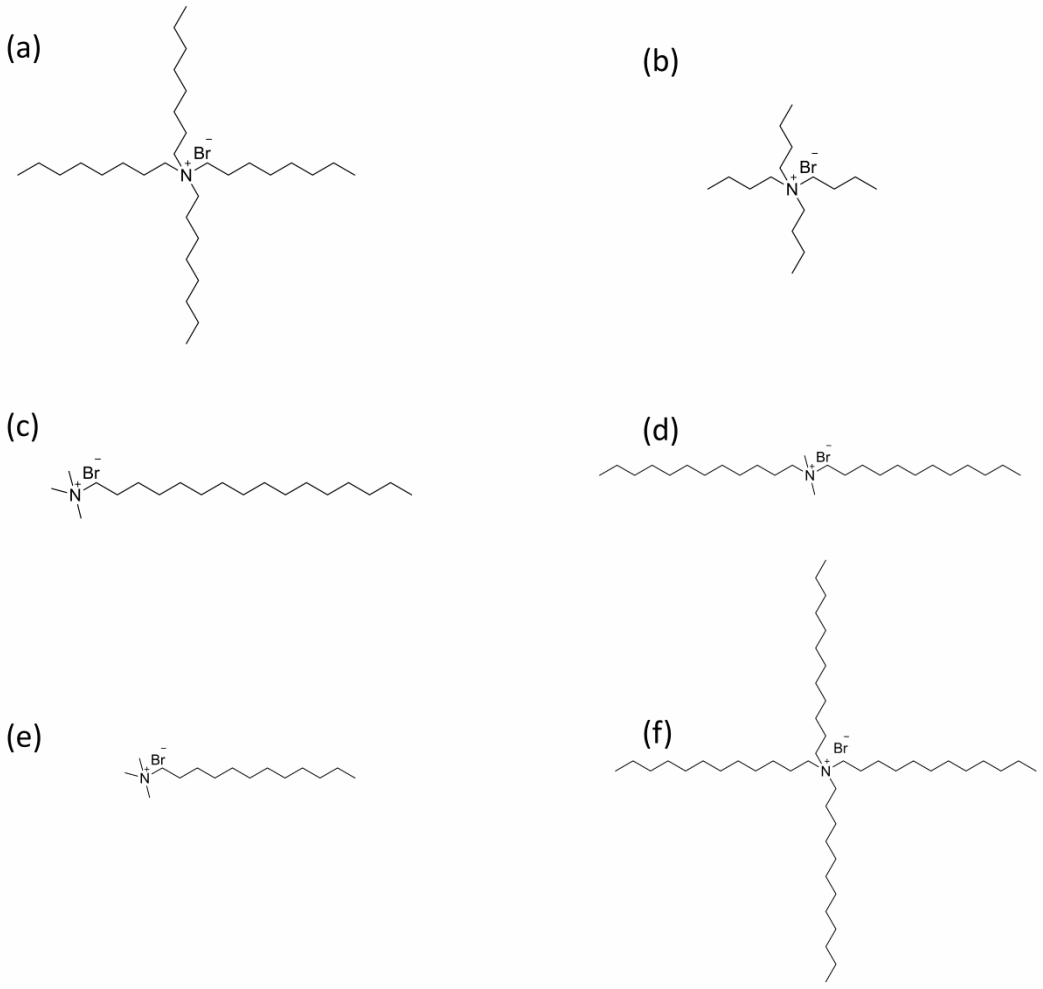

Figure 2.1: Molecular structure of the different surfactants (a) TOAB, (b) TBAB, (c) CTAB (d) DDAB (e) DTAB and (f) TDAB.

TEM imaging of Si NCs synthesized in the presence of TOAB as the surfactant template (Figure 2.2(a)) show that the Si NCs are highly size and shape monodisperse, with no evidence of aggregation. Inset in Figure 2.2(a) is a histogram of NC diameters, determined by analysis of TEM images of *ca.* 200 NCs located at random locations on the grid. Fitting the histogram to a Gaussian model yielded a mean diameter of 1.9 nm, with a standard deviation of 0.3 nm, closely matching with the (111) interplanar spacing of bulk silicon, emphasizing the highly size monodisperse nature of the NCs. This is in good agreement with reports published by both Tilley[19] and Zuilhof and co-workers, [24] who both used TOAB as the surfactant for the synthesis of Si NCs.

Replacing TOAB with either TBAB or CTAB resulted in an increase in the mean NC diameter to 2.5 ± 0.3 nm and 2.6 ± 0.3 nm respectively, without a concomitant increase in size dispersity, see Figures 2.2(b) and 2.2(c). Si NCs synthesized in the presence of DDAB (3.0 nm) and DTAB (4.0 nm) were found to be larger in size and more irregular in shape, with a standard deviation of 0.9 nm, see Figures 2.2(d-e). The largest NCs (5.8 ± 1.8 nm) were obtained when TDAB was employed as the surfactant, though this was accompanied by a significant increase in size and shape polydispersity.

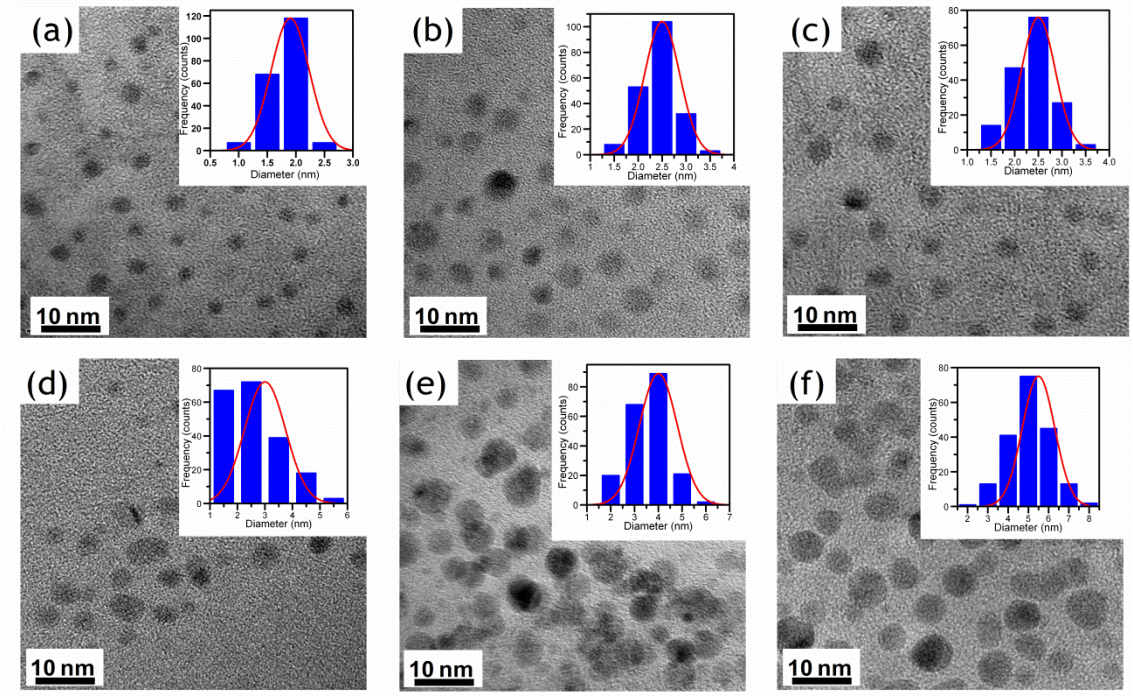

Figure 2.2: Representative TEM images of the Si NCs synthesized in the presence of the following surfactants: (a) TOAB, (b) TBAB, (c), CTAB, (d) DDAB, (e) DTAB, and (f) TDAB. Inset: Size histograms of the Si NCs with curves fit to the data using a Gaussian model.

High-resolution TEM (HR-TEM) imaging was used in conjunction with selective area diffraction to confirm the crystallinty and establish the crystal phase of the as-synthesized NCs; see Figures 2.3(a-b)), respectively. HR-TEM imaging of Si NCs produced using DTAB (Figure 2.3(a)) as the surfactant showed that the Si NCs form a single contiguous crystalline phase, without the presence of packing defects. The lattice fringes shown in Figure 2.3(a) correspond to a *d* spacing of 1.2 Å, matching the (331) spacing reported for the silicon unit cell. Selected area electron diffraction patterns of the Si NCs, see Figure 2.3(b), shows rings consistent with the diamond lattice of Si; (111) at 3.14 Å, (200) at 1.92 Å, (311) at 1.68 Å and (400) at 1.31 Å, see Table 2.2.[25]

It is noted that while figures 2.3(a-b) are explicative of TEM images and SAED patterns obtained for NCs fabricated using other cationic surfactants, it was not possible to obtain SAED patterns of the smallest Si NCs synthesized using TOAB as a template, due to the small scattering cross section of silicon. Figure 2.3(c) shows the energy dispersive X-ray spectrum, where the Si peak corresponding to the presence of the NCs is evident.

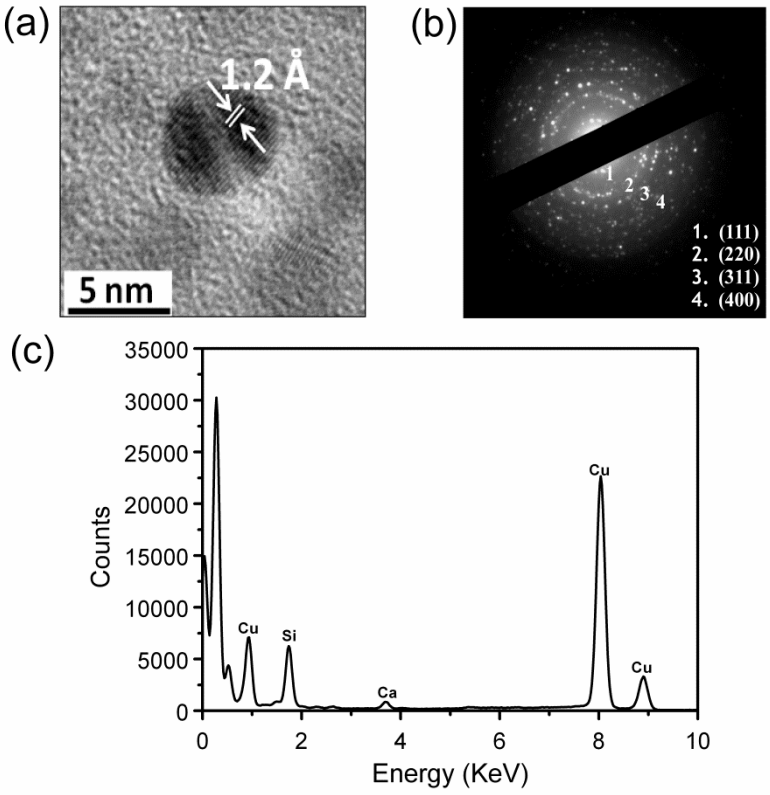

Figure 2.3: (a) HR-TEM, (b) SAED pattern, and (c) EDX profile of the silicon nanocrystals synthesized with DTAB as the surfactant.

Table 2.2. *d* spacing calculated from selected area electron diffraction pattern of the silicon nanocrystals.

d spacing calculated from SAED, Å	*d* spacing in bulk Si,[26] Å	(hkl) assignment
3.14	3.13	(111)
1.92	1.92	(220)
1.68	1.63	(311)
1.31	1.35	(400)

Other elemental peaks assigned to the presence Cl and Ca are probably due to solvent artefacts, while C and Cu peaks are due to the carbon-coated copper grid. The surface chemistry of the Si NCs was characterized by FTIR spectroscopy see Figure 2.4, to identify the terminal moieties on the nanocrystal surface. Figure 2.4 shows the spectrum obtained for Si NCs synthesized using TOAB as the surfactant, although similar spectra were obtained for all the nanocrystals reported here. The Si NCs exhibit clear C-H stretching signals, with symmetric CH_2, asymmetric CH_2, and the asymmetric C-CH_3 stretching vibrations at 2856, 2926, and 2959 cm^{-1}, respectively. The peak at 1378 cm^{-1} is assigned to the C-CH_3 symmetrical bending mode, while the peaks at 1260 and 1460 cm^{-1} are attributed to the symmetric bending and scissoring vibration of the Si-C bond, respectively. The absence of the CH=CH_2 peaks at 1640 and 3080 cm^{-1}, combined with the formation of the Si-C bond at 1460 cm^{-1}, confirms covalent attachment of the 1-heptene to the NC surface.[19, 24, 26]

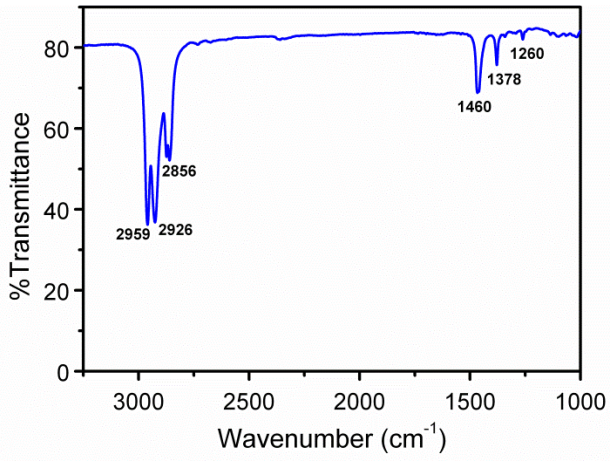

Figure 2.4: Fourier transform infrared spectrum of alkyl-terminated silicon nanocrystals using TOAB as the surfactant.

The absence of peaks between 1000–1100 cm^{-1}, corresponding to Si–OR stretching vibrations, highlights that the silicon nanocrystals are well passivated, with minimal surface oxidation. The surface chemistry of the Si NCs was also investigated by using high resolution XPS spectroscopy, see Figure 2.5. The Si 2p spectra in Figure 2.5 (a) shows a strong peak centred at 102.2 eV, in good agreement with previous reports for alkyl-capped silicon nanocrystals.[27] The main peak at 102.2 eV is assigned to Si-C bonding, confirming covalent attachment of alkyl groups to the Si NC surface, while the presence of the peak at 103.0 eV is indicative of some surface oxidation ($Si\text{-}O_x$) that was not observed in the FTIR spectrum (Figure 2.4). The C1s spectrum in Figure 2.5(b) has three peaks at 284.1, 284.8 and 285.6. The first two peaks are assigned to C-Si and C-C/C-H bonding, while the peak at 285.6 corresponds to C-O. The existence of a C–Si component agrees with the FTIR spectra indicating covalent attachment of the alkyl ligands to the nanocrystal surface.

The O1s spectrum in the Figure 2.5(c) is fitted with two components at binding energies of 532.2 and 533.0 eV, due to $Si–O_x$ groups at the nanocrystal surface. Figure 2.6 (a) shows the UV-Vis absorption spectra of the silicon nanocrystals in hexane prepared using the different surfactants. The spectrum of the smallest nanocrystals (1.9 nm), synthesized when TOAB was employed as the surfactant, showed a broad absorption band centred at *ca.* 260 nm with an onset of absorbance located at 350 nm. This is in excellent agreement with previous reports for similarly sized alkyl-terminated Si NCs, which have assigned this feature to the direct Γ-Γ band gap transition.[28, 29] Increasing the mean NC diameter to *ca.* 2.5 nm by using TBAB or CTAB as the surfactant resulted in a distinct red-shift in the wavelength position of the absorption band to 266 and 267 nm, respectively. Further red shifts in the absorption spectrum were observed for increasing nanocrystal sizes, with the largest size nanocrystals (5.8 nm) showing a strong peak centred at 272 nm, corresponding to a 12 nm shift compared to the smallest (1.9 nm) nanocrystals.

Interestingly, the changes in size distribution do not significantly affect the onset of absorbance, located at *ca*. 350 nm (3.5 eV), which is considerably blue shifted from that of bulk silicon. The absence of vibrational features in the absorption spectra, which have been observed for Si NCs prepared using a similar approach and assigned to the presence of trace amounts of toluene,[30] indicates the utility of the column

chromatography purification of the as-synthesized nanocrystals,[31] see Experimental Section and Figure 2.6(b) for further details.

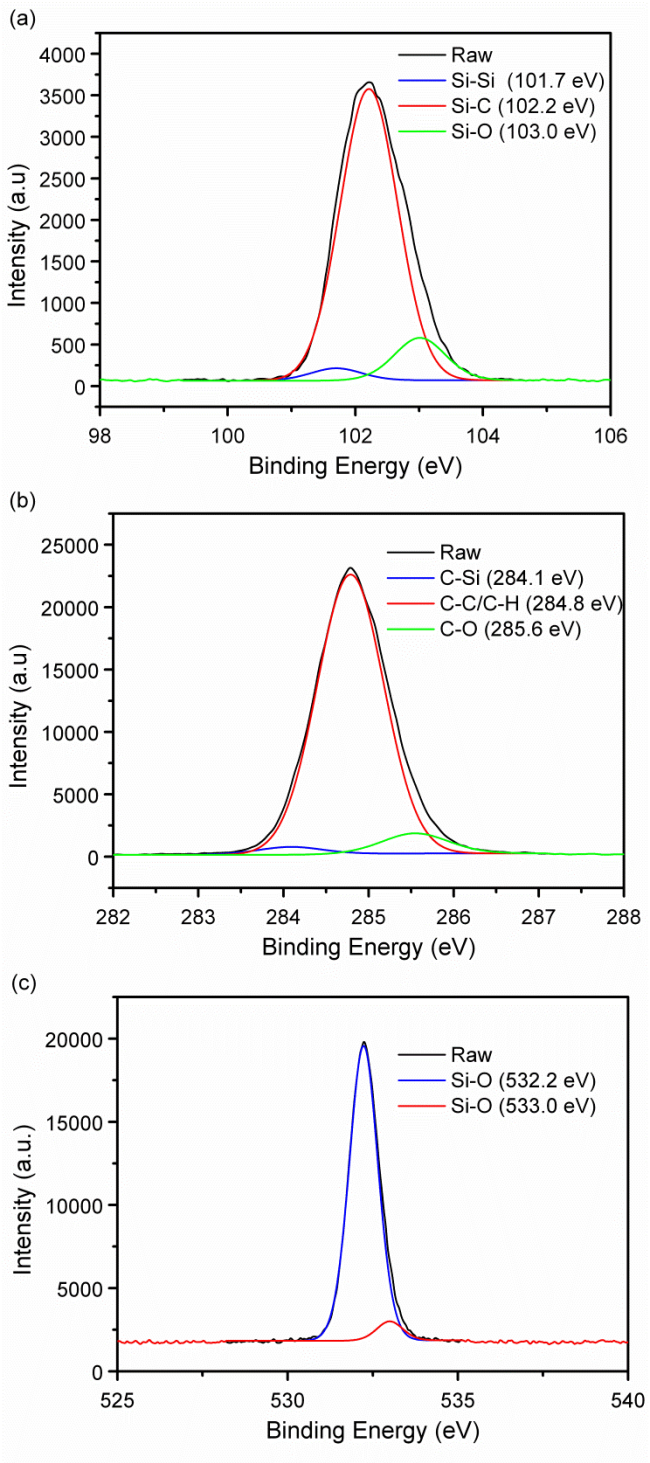

Figure 2.5: XPS spectra of alkyl-terminated silicon nanocrystals.

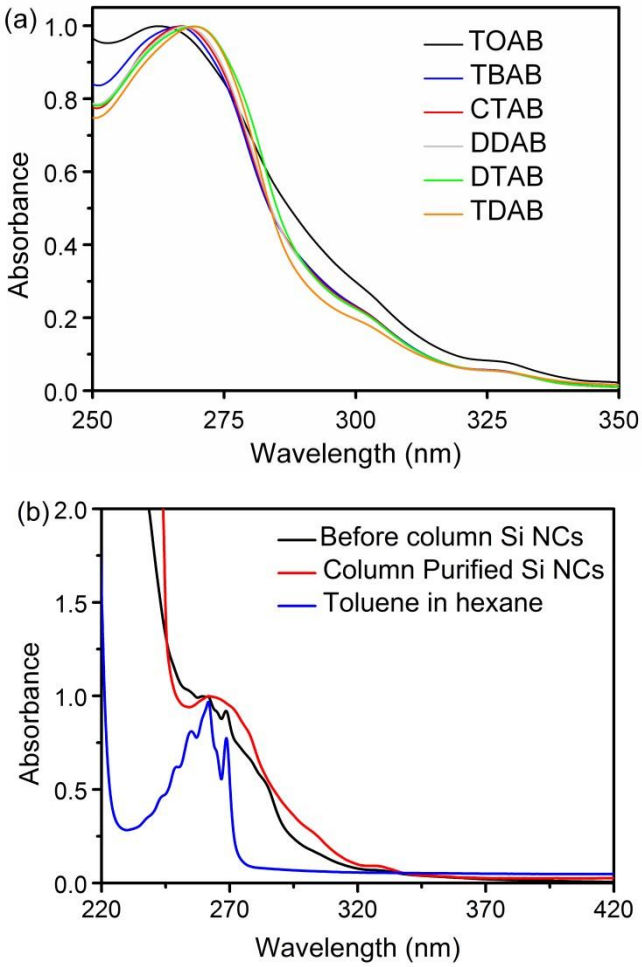

Figure 2.6: (a) Normalized UV-Vis absorption spectra of the silicon nanocrystals synthesized in the presence of the various surfactants. (b) UV-Vis absorbance spectra of the as-synthesized silicon nanocrystals (black line), column purified silicon nanocrystals (red line), and dilute solution of toluene in hexane (blue line). All spectra were recorded using an integrating sphere to eliminate artefacts due to scattering.

Figure 2.7 shows the photoluminescence spectra (280 nm excitation) of the Si NCs synthesized using the different surfactants measured at room temperature. Dilute dispersions of the Si NCs in hexane were prepared with the same optical densities for comparison. Luminescence from the Si NC dispersions is observed over a narrow spectral range between 300 – 420 nm, with a wavelength maximum at *ca.* 330 nm, similar to that reported for other alkyl terminated silicon nanocrystals.[19, 32, 33] The full width at half maximum (FWHM) was found to be *ca.* 60 nm, emphasizing the monodispersity of the nanocrystals.[19] While the luminescence intensity decreases monotonically with increasing nanocrystal diameter, there is no change in the PL spectra of the Si NCs with core diameters ranging from 2 to 6 nm. Despite extensive

investigation over the last 10-15 years, the exact origin of PL from nanocrystalline silicon remains a divisive topic, complicated by presence of both direct and indirect band gap transitions.[34, 35] The wide variety of synthetic strategies reported, together with broad particle size distributions, different ligand passivation schemes and surface oxidation, have all contributed to the lack of consensus.[35, 36] The underlying mechanism is usually described in terms of either a quantum confinement model based on quantum size effects in the nanocrystalline silicon core, or a surface chemistry model that emphasizes the importance of surface phenomena at the interface between the crystalline core and the host matrix.[37] Both models present extreme viewpoints, and other theories combining elements of both models have also been presented.[38]

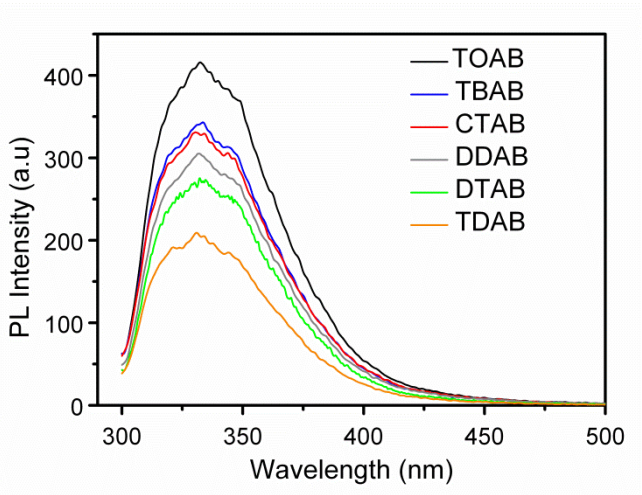

Figure 2.7: Photoluminescence spectra of the silicon nanocrystals synthesized in the presence of the various surfactants. Spectra were recorded on samples with the same optical density at an excitation wavelength of 280 nm.

The marked size dependency observed in the UV-Vis absorption spectra shown in Figure 2.6 (a) agrees well with the quantum confinement model, supporting the assignment to direct transitions within the nanocrystal core. In contrast, the PL spectra shown in Figure 2.7 exhibit a blue emission that is independent of nanocrystal size, implying that exciton recombination is not confined within the nanocrystal core, and that the nanocrystal surface must be involved in the emission process. The uniformity of the luminescence observed from Si NCs (the normalized PL spectra are entirely superimposable) suggests that a limited number of surface or near-interface states are involved. This interpretation is in agreement with studies on hydrogen-terminated Si NCs by Yang *et al.*, who concluded the most plausible mechanism is that excitons are

first formed within Si NCs by direct transitions at Γ or X point, which transfer to and recombine at states close to the interface between the nanocrystal and the surrounding matrix.[38] Further evidence for the role of surface states in the luminescence process was recently provided by Dasog *et al.*,[32] who demonstrated tuning of the emission colour of Si NCs from red to blue by titration with trace amounts of nitrogen-containing compounds. Figure 2.8(a) shows the photoluminescence spectra of TOAB-synthesized 1.9 nm Si NCs in hexane, obtained using excitation wavelengths ranging from 280 to 400 nm in 20 nm intervals. The photoluminescence spectra display small features within the main peak at different excitation wavelengths, in agreement with previous results.[29]

Excitation energies for maximum PL intensity (4.4 eV) significantly exceed the absorption edge (3.5 eV), with PL intensity that depends sensitively on excitation energy. The wavelength position of the PL maximum ranges from 330 nm for excitation at 280 nm, to 438 nm for 400 nm excitation. This corresponds to an overall red shift in the PL peak position of 108 nm, as the excitation wavelength is increased by 120 nm, see Figure 2.8(b). This marked dependency on excitation wavelength has been widely reported for silicon nanocrystals, prepared using different synthetic methods and surface functionalities.[9, 29, 39] PL excitation spectra (PLE) were recorded using excitation wavelengths ranging from 280 to 400 nm as shown in Figure 2.8(c). Several closely spaced discrete features appear in the PLE spectra, with optimal excitation wavelengths still significantly above the energy of the absorption edge (3.5 eV).

The PLE spectra are seen to decrease in intensity and red-shift in position when recorded at longer emission wavelengths, again suggesting a combination of factors involving the nanocrystal core and the surface states. This wavelength dependence is usually attributed to sample polydispersity, with the smaller NCs being selectively excited at shorter wavelengths, and larger NCs at longer wavelengths.[39, 40] However, the narrow size distributions in the Si NCs reported here precludes the shift in peak position being caused by polydispersity.[9, 34] Considering that the optimal excitation energies are considerably greater than the band gap energy, the sharp decrease in PL intensity at excitation wavelengths close to the absorption edge, the most plausible interpretation is that excitation at shorter wavelengths results in efficient generation of excitons, which readily transfer to and recombine at shallow surface trap states to give blue emission. Excitation at longer wavelengths may result in less efficient generation

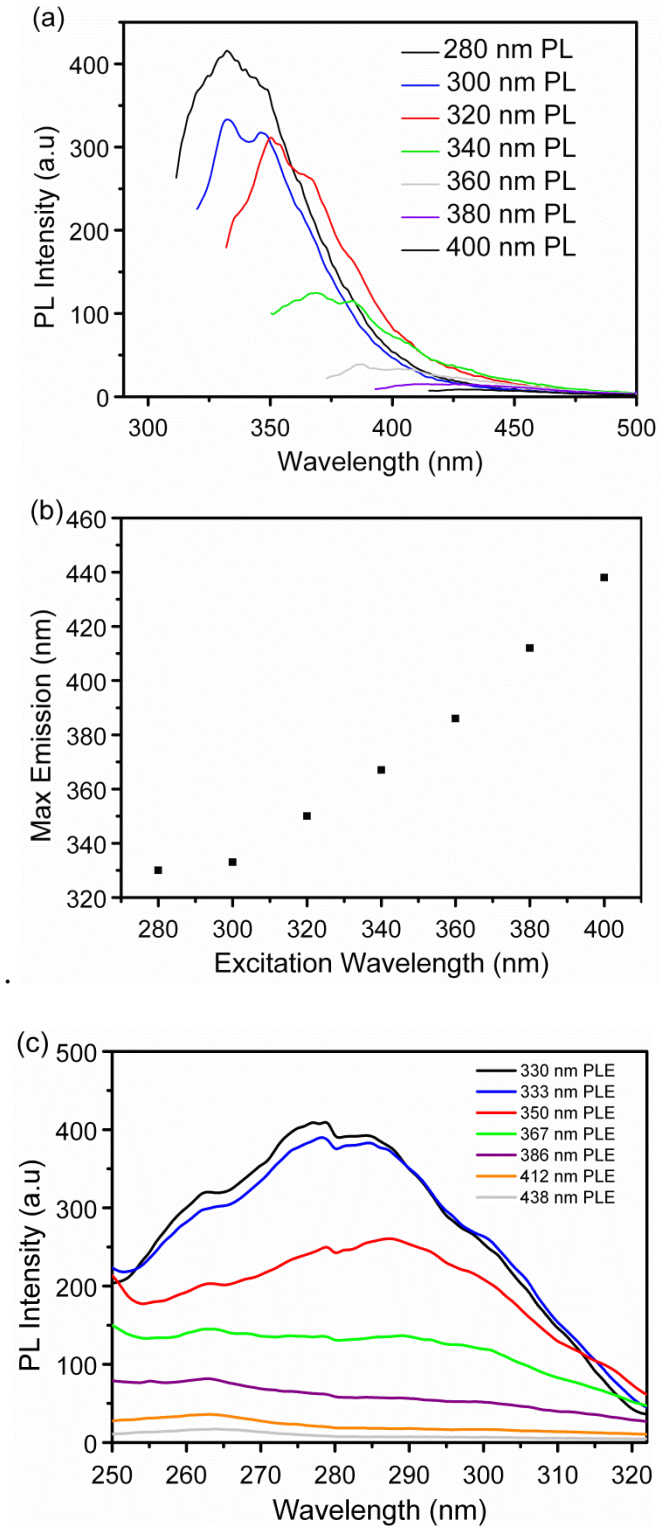

Figure 2.8: (a) Photoluminescence spectra of 1.9 nm silicon nanocrystals recorded at different excitation wavelengths. (b) Wavelength position of the luminescence maximum as a function of excitation wavelength. (c) Photoluminescence excitation (PLE) spectra of 1.9 nm silicon nanocrystals. Wavelength positions refer to maximum emission positions shown in Figure 2.8(b).

of excitons, which transfer to deeper trap states, resulting in less intense emission. There may also be increased transfer of excitons to nonradiative centres,[41] which would also contribute to the overall decrease in PL intensity.

The Quantum Yield (QY) of the silicon nanocrystals was determined using the comparative method described by Williams *et al*.[21] The fluorescence standard L-Tryptophan (Reagent grade, ≥98 %) was selected as the reference material as 98% of its luminescence spectrum overlaps that of the silicon nanocrystals. The QY of L-Tryptophan is dependent on the temperature, pH, concentration and solvent. Robbins *et al.*[22] previously determined the temperature dependence of the L-Tryptophan QY at pH 7. The fluorescence lifetime (τ^{-1}) of L-Tryptophan at pH 7 is expressed as:

$$\tau^{-1}(pH\ 7) = k_f + k_t + k_{eaq^-} + k_i \qquad (2.2)$$

Where k_f is the fluorescence, k_t is intersystem crossing, k_{eaq}^- is photoionization and k_i is intramolecular quenching. The work carried out by Robbins *et al* was replicated to calculate the quantum yield of L-Tryptophan at any temperature. Figure 2.9 shows the modelling of the dependence of the QY of Tryptophan on temperature for all the different processes involved at pH 7. From the raw data, the QY of fluorescence, at a certain temperature (19 ºC, 15.9%) can be determined and therefore the QY of the silicon NCs can be calculated extremely accurately.

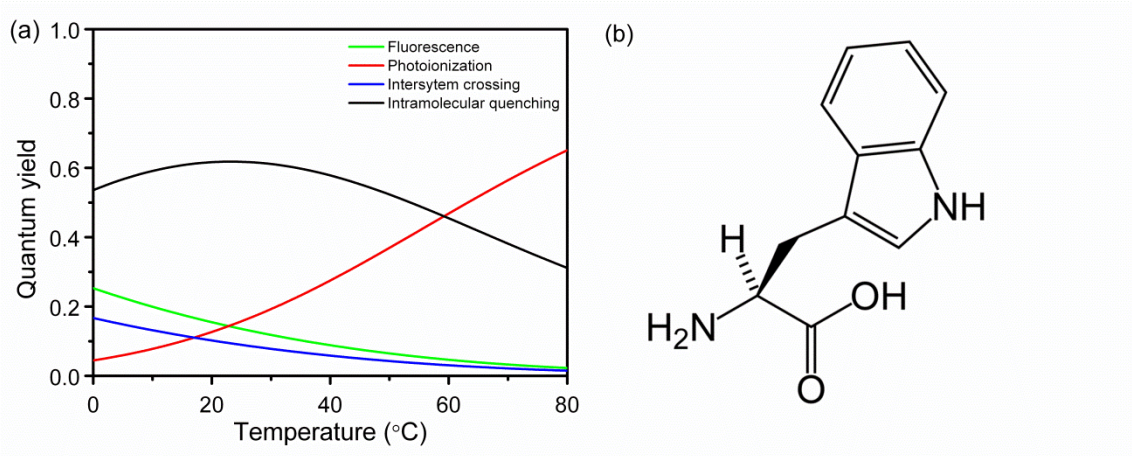

Figure 2.9: (a) Calculated quantum yields of fluorescence, intersystem crossing, photoionization and intramolecular quenching for tryptophan at pH 7, as a function of temperature. (b) Molecular structure of L-Tryptophan.

It was shown in Figure 2.7 above that the photoluminescence intensity of the Si NCs decreases monotonically with increasing nanocrystal diameter. Figure 2.10 (a) shows the integrated PL intensity (280 nm excitation) of diluted dispersions of 1.9 nm diameter Si NCs in hexane and aqueous solutions of tryptophan (pH 7.0) recorded under identical excitation conditions. Linear regression analysis was employed to determine the relative PL intensities of the sample and reference solutions over the range of concentrations, see also Figure 2.11 and Table 2.3 for plots and analysis of Si NCs synthesized using the other various surfactants. The quantum yield of the 1.9 nm Si NCs was found to be 12 % at the optimal excitation wavelength of 280 nm, comparable with values reported for Si NCs of similar sizes.

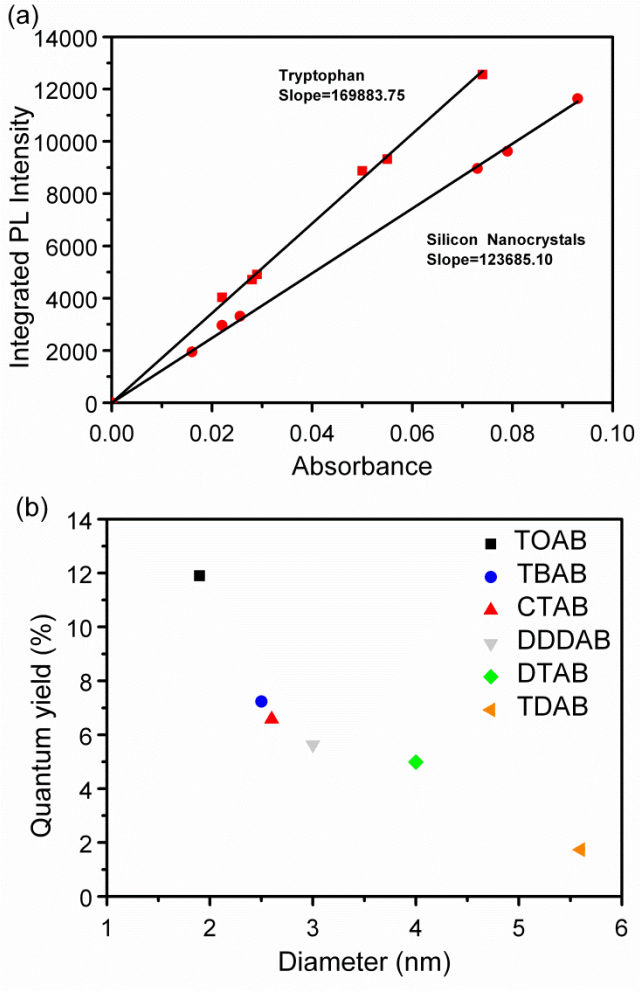

Figure 2.10: (a) Integrated PL intensity versus absorbance for various dilute dispersions of 1.9 nm diameters Si NCs in hexane and aqueous solutions of tryptophan (pH 7.0) recorded under identical excitation conditions. (b) Quantum yields of the Si NCs *versus* average core diameter.

reported in the literature.[24, 42, 43] The quantum yields of the Si NCs exhibit an inverse relationship with the mean NC diameter, decreasing to *ca.* 7% for 2.5 nm nanocrystals, with a minimum of less than 2% recorded for 5.8 nm NCs, see Figure 2.10 (b). The observed trend in the quantum yields of the Si NCs may be accounted for by a combination of less efficient generation of excitons and the presence of greater number of nonradiative traps and recombination pathways with increasing size. To further understand the photoluminescence properties, photoluminescence lifetimes of the Si NCs synthesised in the presence of TOAB were acquired using time-correlated single photon counting methods at an excitation wavelength of 402 nm for all Si NC sizes, see Figure 2.12. The photoluminescence decay required a three-component exponential fit with time constants of approximately 0.8, 3.76 and 11.59 ns, see Table 2.4. entry 1. [29, 30, 42]

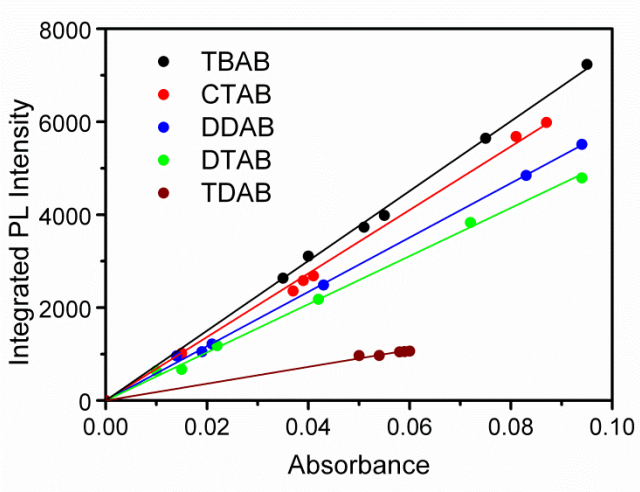

Figure 2.11: Integrated PL intensity versus absorbance for dilute dispersions of silicon nanocrystals synthesized using different surfactants in hexane.

Surfactant	Slopes	Quantum Yield (Φ)
TBAB	75168.74	7.2
CTAB	68372.39	6.6
DDAB	58491.82	5.6
DTAB	51828.39	5.0
TDAB	17939.17	1.7

Table 2.3. Fitted slopes and calculated quantum yields from linear regression analysis of data shown in Figure 2.11 above.

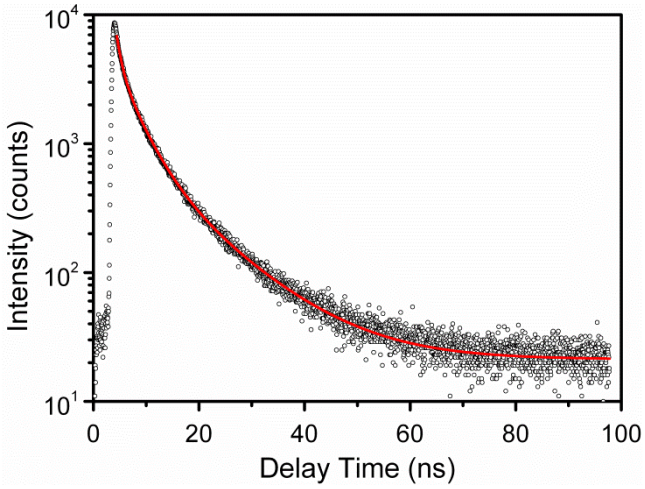

Figure 2.12: Time resolved photoluminescence spectra of 1-heptane capped silicon nanocrystals in hexane.

This suggests that there exist multiple de-excitation processes in the Si NCs consistent with report in the literature. The rapid rates observed in Figure 2.12 provide strong evidence that the observed emission results from dipole-allowed recombination across the direct bandgap transition in Si NCs with an alkyl terminated functional group. In order to determine if the solvent has any effect on the fluorescence properties for Si NCs, the Si NCs were exposed to different organic solvents of varied polarity, see Figure 2.13 (a). The Si NCs were excited at 280 nm and kept at the same concentration for direct comparison. A red shift of ~ 50 nm was observed in PL emission maximum by increasing the solvent polarity from hexane to chloroform, see Figure 2.13 (b) and Table 2.5; demonstrating that the PL properties were sensitive to the medium surrounding the nanocrystals.

This is in agreement with the work reported by Dasog *et al*,who also observed similar results attributing the effect to an energy transfer excited state.[32] Figure 2.14 (a) show the long term stability of the Si NCs synthesised when TOAB was used as the surfactant using UV-Vis absorption spectroscopy. The spectrum was recorded over a period of 90 days. The spectra show a broad absorption band featured at *ca.* 260 nm with an onset of absorbance located at 350 nm. Notably, there is no decrease or shifting in the absorption spectrum, demonstrating the physical stability of the Si NCs. Figure 2.14 (b) shows that the Si NCs exhibit excellent long term term PL stability, decreasing by less than 15 % continuous illumination for 12 hours. The Si NCs show no significant

Table 2.4. Summary of the amplitudes and time constants for three-component exponential fits for time-resolved PL spectra of Si NCs used in this study.

Entry	Excitation Wavelength (nm)	A1(%)	τ1 (ns)	A2(%)	τ2 (ns)	A3(%)	τ3(ns)	χ^2
1	402	10	0.8	48	3.76	41	11.59	1.08
2	402	9	0.8	37	3.9	54	16.5	1.15
3	402	9	1.3	49	4.5	41	12.58	1.21
4	402	13	1.0	49	4.2	39	12.1	1.00

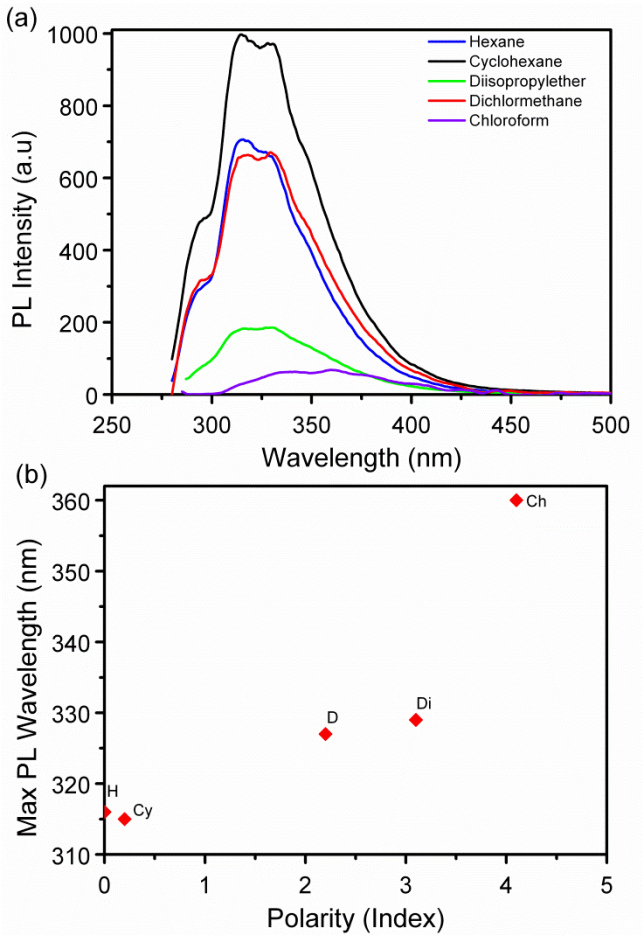

Figure 2.13: (a) Comparison of the photoluminescence emission spectra of silicon nanocrystals in various non-polar solvents. (b) PL maximum *versus* solvent polarity for different Si NCs at excitation of 280 nm.

Table 2.5. A list of the non-polar solvents used in this study and their respective polar index constants.

Solvent	Symbol	Polarity Index
Hexane	H	0
Cyclohexane	Cy	0.2
Diisopropylether	D	2.2
Dichloromethane	Di	3.1
Chloroform	Ch	4.1

photobleaching compared to other organic fluorphores and polysilanes. For example, rhodamine 6G, a common organic dye completely bleaches in ~ 10 min,[44] and polysilane derivatives photobleach quickly upon exposure to UV light.[45] Figure 2.14 (c) show the FTIR spectra of the Si NCs recorded at 1 week (blue lines) and 26 weeks (red line) after storage under ambient atmospheric conditions. Both spectra show C-H stretching signals due to the presence of the alkyl ligands at the nanocrystal surface, with symmetric CH_2, asymmetric CH_2, and the asymmetric C-CH_3 stretching vibrations at 2851, 2922, and 2959 cm^{-1}, respectively. The peak at 1378 cm^{-1} is assigned to the C-CH_3 symmetrical bending mode, while the peaks at 1261 and 1462 cm^{-1} are attributed to the symmetric bending and scissoring vibration of the Si-C bond, respectively.

The absence of the CH=CH_2 peaks at 3080 and 1640 cm^{-1}, combined with the formation of the Si-C bond at 1460 cm^{-1}, confirms covalent attachment of the alkyl groups to the NC surface.[3,10,16] Two additional peaks at 1099 and 1018 cm-1, attributed Si–OR stretching vibrations, are clearly seen in the spectrum recorded after 26 weeks, indicating oxidation of the nanocrystal surface.[10,16] The low intensity of these peaks recorded after 1 week indicates that only minimal oxidation of the silicon core has taken place, indicating that the surface of as-synthesized Si NCs are well passivated.

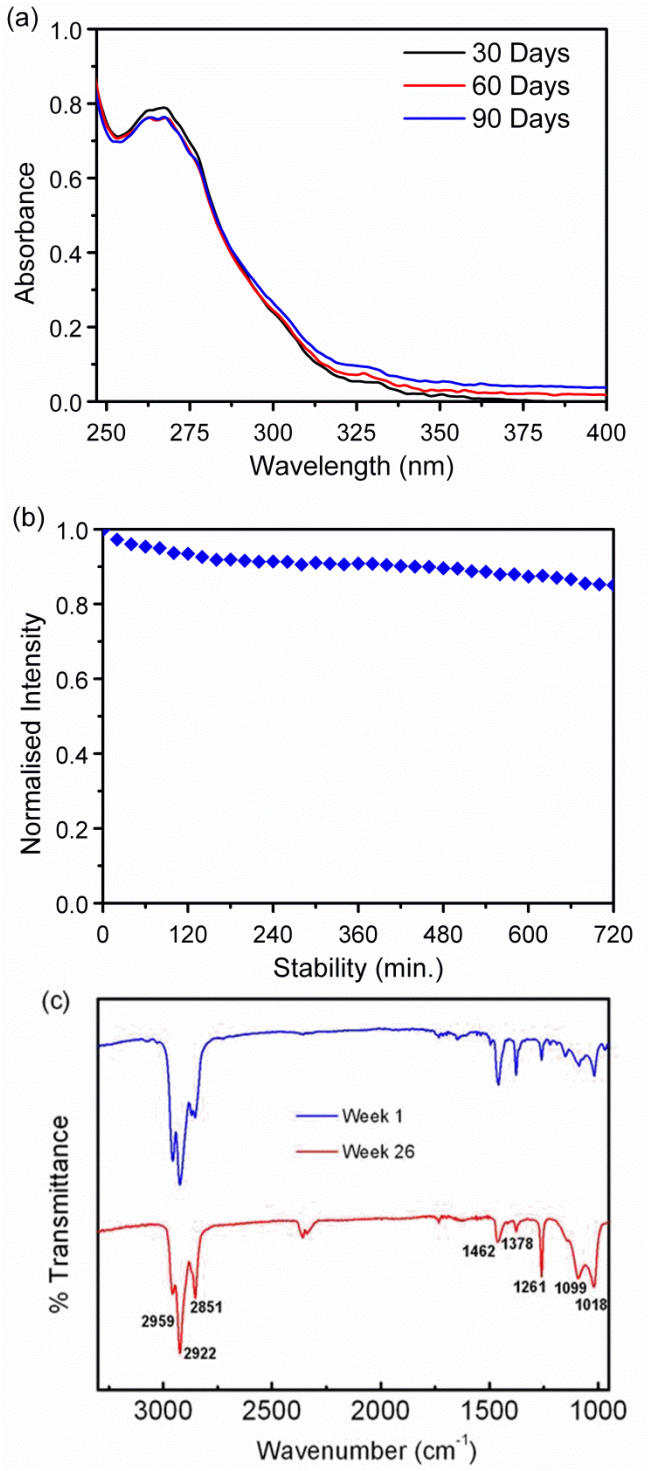

Figure 2.14: (a) UV-Vis spectra of the silicon nanocrystals monitored over a period of 90 days. (b) Long term photoluminescence stability of the alkyl capped silicon nanocrystals recorded using 12 hours using a 280 nm excitation. (c) FT-IR spectra of alkyl-terminated silicon nanocrystals recorded 1 week (blue lines) and 26 weeks (red line) after storage under ambient conditions.

2.3.2 Synthesis of Silicon Nanocrystals using Non-Ionic Surfactant

The use of inverse micelle templates for the preparation of metals and quantum dots is important as the nucleation and growth kinetics of the nanocrystal may be controlled depending on the molecular structure of the surfactant and reaction conditions used. Reports have demonstrated that the shapes of micelles formed by functionalized surfactants in solutions or solvents, and the selective adsorption of surfactant molecules and their respective counter ions on certain crystallographic facets, can provide control over the particle morphology during nanoparticle growth.[46] Previously in section 2.3.1, size controllable Si NCs were synthesised using a variety of cationic surfactants. Although our primary work focused on the synthesis of Si NCs in the presence of cationic surfactants, the use of non-ionic surfactants templates in the formation of Si NCs was also explored.

The main reason for this was to see if there was a change in the nanocrystals size, shape and optical properties. Alkyl terminated Si NCs were formed by reduction of silicon tetrachloride by lithium aluminium hydride under inert atmosphere. Pentaethylene glycol monododecyl ether (C12E5) was used as the surfactant template (see Figure 2.15 (a) for the molecular structure) instead of tetraoctyl ammonium bromide and all the other reaction conditions were kept the same, see Table 2.1 Entry 7. C12E5 is a soapy surfactant and prior to TEM imaging and optical measurements the Si NCs had to be put through a column twice in order to remove the majority of surfactant. The difference of the purity was apparent from the TEM imaging with samples after column chromatrography being much clearer to image. Figure 2.15 (b) shows a representative TEM image of the silicon nanocrystals. The Si NCs are spherical in shape, highly size and shape monodisperse with no evidence of aggregation.

The inset shown in Figure 2.15 (b) shows histrogram of the nanocrystal diameter. Fitting a Guassian to the histogram yields a mean diameter of 1.9 nm, with a standard deviation of 0.35 nm. This is in excellent aggreement with the Si NCs produced when tetraoctylammonium bromide was employed as the surfactant; see Section 2.3.1. The optical properties of the Si NCs were studied using UV-Vis absorption, photoluminescence (PL), photoluminescence excitation (PLE) and quantum yield measurements, see Figure 2.16 (a). The Si NCs exhibit a strong absorbance band centred at ~273 nm with an onset of absorbance at 360 nm, consistent with reports of Si

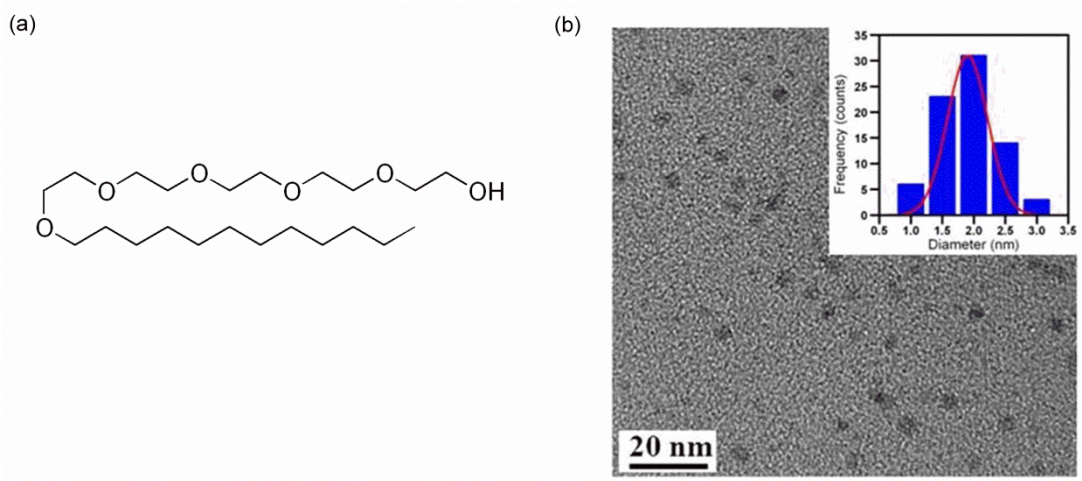

Figure 2.15: (a) Molecular structure of Pentaethylene glycol monododecyl ether (C12E5) non-ionic surfactant. (b) TEM image of alkyl capped silicon nanocrystal synthesised using C12E5 as the surfactant.

NCs synthesised using cationic surfactants. The photoluminescence spectrum was obtained using an excitation at 280 nm. The emission has a peak at *ca.* 330 nm (3.75 eV), a Stokes shift of 50 nm from the absorbance maximum, in good agreement with previous reports of Si NCs of similar size.[19, 29, 33] The shift in the photoluminescence from 1.1 eV in bulk silicon to 3.75 eV in these small Si NCs is direct evidence of the presence of quantum confinement in these structures. Luminescence from the Si NCs is observed over a narrow spectral range, similar to the cationic surfactants reported in Section 2.3.1.

The PL spectrum of the Si NCs synthesised in the presence of C12E5 exhibits peaks at 315 nm and 455 nm corresponding to excitation at 280 nm and 400 nm respectively. This corresponds to an overall red shift in the PL peak position of 125 nm, as the excitation wavelength is increased by 140 nm; see Figure 2.16(b). This clear dependency on excitation wavelength has also been widely observed for Si NCs prepared using different methods of preparation and surface functionalities.[9, 29, 39] PLE spectra shows a narrow peak at 275 nm, considerably above the band gap energy of the Si NCs, suggesting radiationless transfers and recombination at states close to the nanocrystal surface. The quantum yield of the Si NCs were calculated using L-tryptophan as the standard. Comparsion of the slopes of the linear fit to the two sets of data, shown in Figure 2.16 (c) yields a quantum efficiency of ~ 7%. The fluorescence lifetime values were found to be 0.8, 3.9 and 16.5 ns; see Table 2.4 entry 2, consistent with our studies using cationic surfactants see Table 2.4 entry 1.

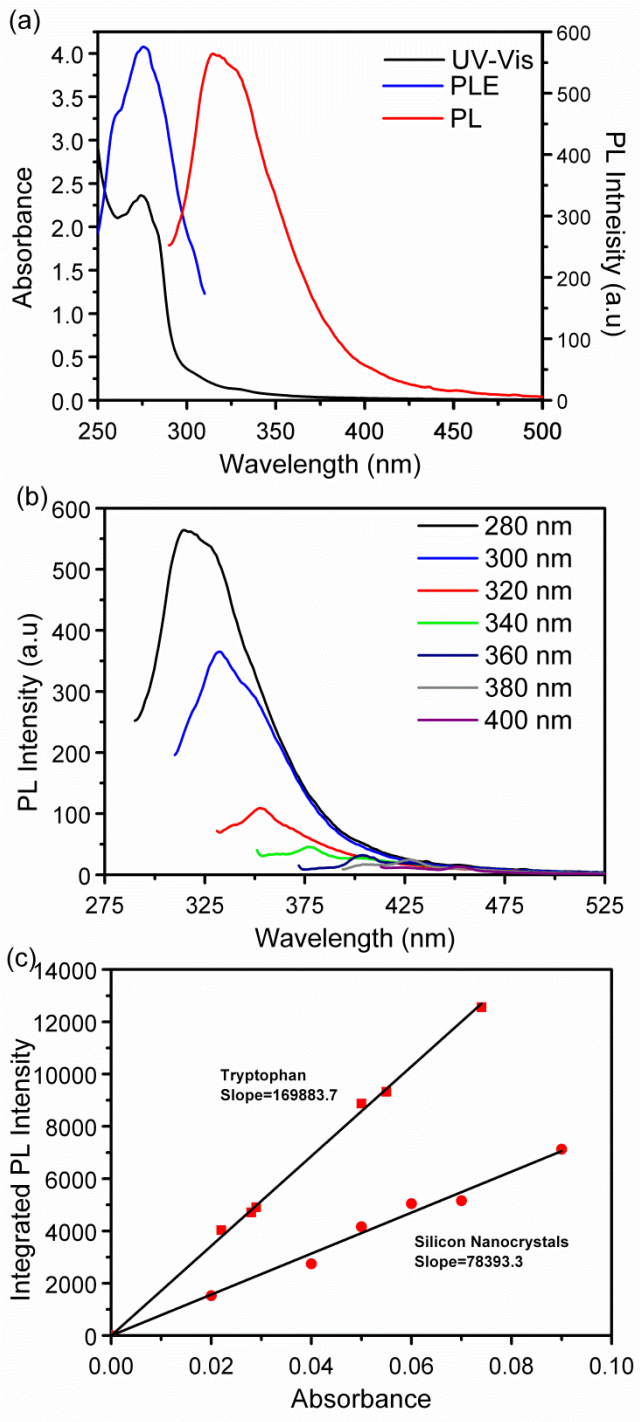

Figure 2.16: (a) UV-Vis absorption, photoluminescence excitation and photoluminescence emission spectra of the silicon nanocrystals. (b) Photoluminescence spectra of the silicon nanocrystals in hexane at a excitation wavelength of 280 – 400 nm. (c) Integrated PL intensity *versus* absorbance for various dilute dispersions of Si NCs in hexane and aqueous solutions of tryptophan (pH 7.0) recorded under identical excitation conditions.

2.3.3 Surfactant Free Synthesis of Silicon Nanocrystals

The use of cationic and non-ionic surfactants in controlling the nucleation and growth kinetics of the Si NCs has been successfully demonstrated in both Sections 2.3.1 and 2.3.2. Having established the role of the surfactant in the reaction, it was decided to synthesise the Si NCs without the presence of a cationic or non-ionic surfactant; see Table 2.1 entry 8 for experimental reaction conditions. A surfactant free synthesis for the preparation of Si NCs is appealing for applications ranging from bioimaging to optoelectronics as it would facilitate the bio application of Si NCs, and moreover ease the integration within flexible polymers in bulk heterojunction architectures.

Figure 2.17 shows a representative TEM image of the Si NCs synthesised without a surfactant. The Si NCs are larger in size, more irregular in shape compared to the Si NCs synthesised in the presence of cationic or non-ionic surfactants. The inset shown in Figure 2.17 is a histogram of the nanocrystal diameter. Fitting a Gaussian to the histogram yields a mean diameter of 3.8 nm, with a standard deviation of 0.7 nm.

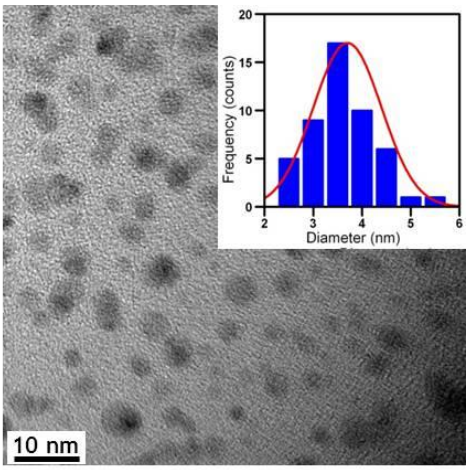

Figure 2.17: TEM image of alkyl capped silicon nanocrystal synthesised without the presence of a surfactant.

The optical properties of the surfactant free Si NCs were investigated using UV-visible, photoluminescence (PL) and photoluminescence excitation (PLE) spectroscopy, see Figure 2.18. The UV-Vis spectrum of the Si NCs dispersed in hexane gives an absorption peak at 262 nm with an onset of absorbance at 320 nm, see Figure 2.18 (a). A photoluminescence excitation (PLE) spectrum, which was collected by fixing the detection at 330 nm shows a peak maximum at 280 nm, a Stokes shift of ~ 20 nm from the absorbance maximum. The photoluminescence spectra in Figure 2.18 (a) shows a

peak maximum at ~ 325 nm, for 280 nm excitation; red shifting by ~ 65 nm from the absorbance maximum. The photoluminescence emission spectra of the Si NCs were measured using excitation wavelengths ranging from 280-440 nm in 20 nm intervals, see Figure 2.18 (b). The Si NCs show excitation dependent emission spectra in agreement with reports from the literature and also Section 2.3.1 and 2.3.2. [9, 29]

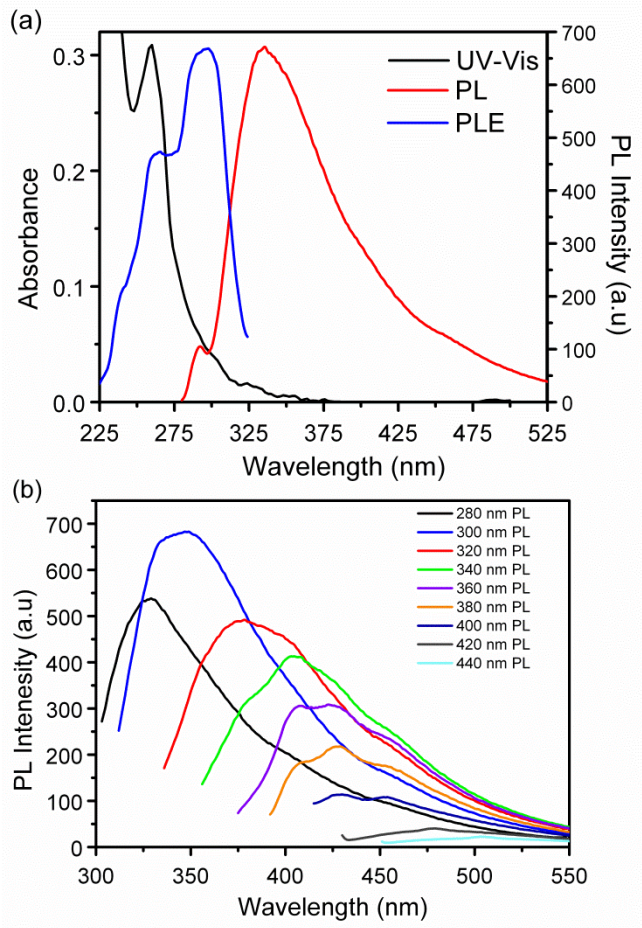

Figure 2.18: (a) UV-Vis absorption, photoluminescence excitation and photoluminescence emission spectra of the silicon nanocrystals. (b) Photoluminescence spectra of the silicon nanocrystals in hexane at a excitation wavelength of 280 – 440 nm.

Photo-luminescent quantum yields were determined using a comparative method which employed L-tryptophan as the emission standard. PL emission spectra of L-tryptophan and hexyl-capped Si NCs were collected for various dilutions. The integrated emission intensity for each sample is plotted *versus* the corresponding UV-Vis absorbance at the same excitation wavelength. The quantum yield of hexyl-capped Si NCs at 280 nm excitation was calculated to be 6% at room temperature, see Figure 2.19 (a), obtained from the ratio of the slopes of the linear fits to L-tryptophan and Si NCs, and the known

quantum yield of L-tryptophan (15.9%) at 280 nm. The resultant quantum yield is in excellent agreement with the quantum yield values reported in Sections 2.3.1 and 2.3.2, obtained when a surfactant was employed during the synthesis. Figure 2.19 (b) shows the time resolved photoluminescence decays of the Si NCs with time constants of 1.3, 4.5 and 12.58. see Table 2.4 entry 3. The results from the TEM imaging and optical measurements confirm that the micelle is not vital to the reaction. Silicon nanocrystals can be prepared by following reaction.

$$SiCl_4 + LiAlH_4 \longrightarrow Si_{diam} + LiCl + AlCl_3 \qquad (2.3)$$

Although the Si NCs suffer from large size distribution, size separation techniques such as size selective precipitation and centrifugation may be used to narrow the size distribution.

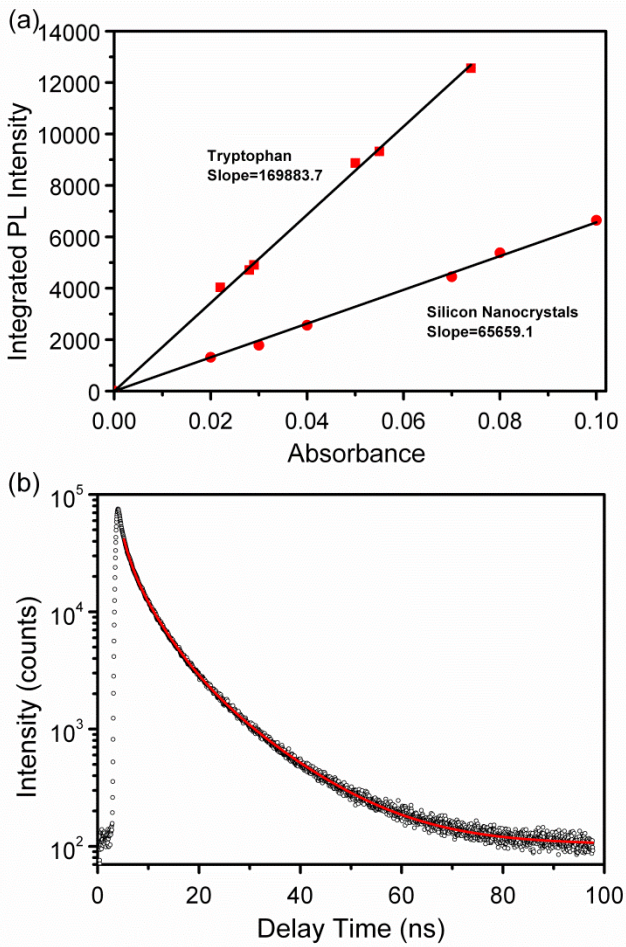

Figure 2.19: (a) Integrated PL intensity *versus* absorbance for various dilute dispersions of Si NCs in hexane and aqueous solutions of tryptophan (pH 7.0) recorded under identical excitation conditions. (b) Photoluminescence decays of 1-heptane capped silicon nanocrystals in hexane.

2.3.4 Scaled Synthesis of Silicon Nanocrystals

Alkyl capped Si NCs have previously been synthesised on a small scale using the inverse micelle procedure reported in Section 2.2.1. However, for active and passive photonic device applications, and the fluorescent ion sensing described in Chapter 4, it is necessary to produce Si NCs in larger quantities to prevent batch to batch variations. To this end, we carried out detailed examination of Si NCs obtained by scaling the synthetic recipes developed by a factor of 10 (gram scale), for reaction conditions, see Table 2.1, Entry 9. Figure 2.20(a) shows a representative TEM image of the heptene-capped Si NCs, showing the range of NC sizes observed when the precursor is scaled from 0.092 ml to 1 ml (~ten times). From the image, it is clear that the Si NCs were relatively monodisperse, with no evidence of aggregation. Inset in Figure 2.20 (a) is the histogram of the Si NCs diameters, determined by analysis of TEM images of *ca*. 120 NCs located at different regions of the grid. The average NCs diameter is 3.0 ± 0.4 nm (0.4 nm being the standard deviation), which highlights the highly monodisperse size distribution synthesized.

The Si NCs were further characterised by IR spectroscopy, see Figure 2.20 (b), which exhibits clear C-H stretching signals, with the symmetric CH_2, asymmetric CH_2 and the asymmetric C-CH_3 stretching vibrations at 2860, 2926 and 2960 cm^{-1}, respectively. The presence of the peak at 1462 cm^{-1}, assigned to the Si-C scissoring vibration, shows the covalent attachment of 1-heptene molecules to the surface of the H-terminated Si NPs. The peak at 1379 cm^{-1} is assigned to the C-CH_3 symmetrical bending mode. The absence of peaks between 1000–1100 cm^{-1}, corresponding to Si–OR stretching vibrations, highlights that the Si NCs are well passivated, with minimal surface oxidation.

Figure 2.20 (c) presents the absorbance and photoluminescence spectra (280 nm excitation) of the 1-heptene capped Si NCs dispersed in hexane. The absorption spectrum shows a broad absorbance band centred at 264 nm, consistent with other reports. The photoluminescence spectrum was obtained using an excitation at 280 nm. The emission has a peak at *ca.* 340 nm (3.65 eV), in good agreement with Si NCs synthesised in section 2.3.1. Interestingly it was also observed that the rate of reduction of the precursor plays an important role in the final size and size distribution of the Si

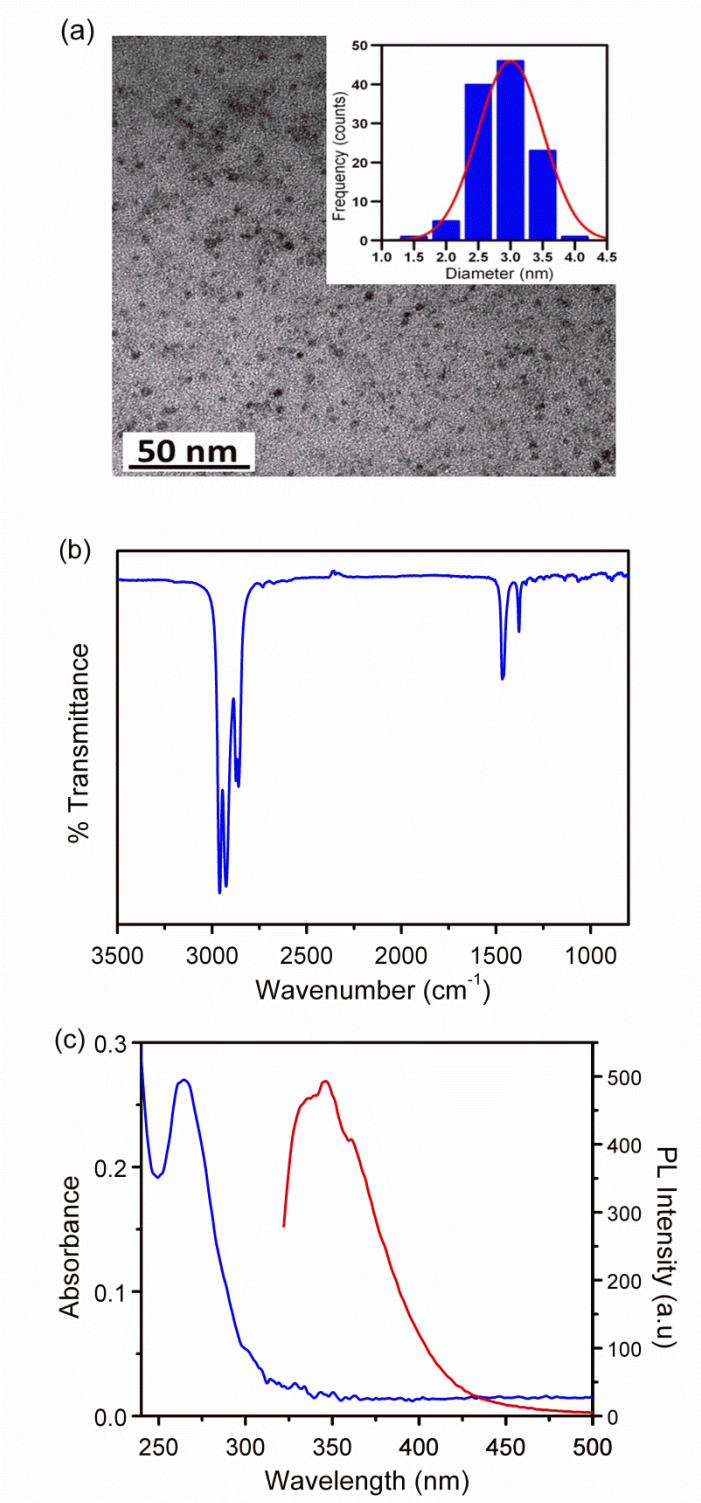

Figure 2.20: (a) TEM image of Heptane-terminated silicon nanoparticles and inset a histogram of Si NC diameters. (b) FTIR spectrum of Heptane-terminated silicon nanoparticles. (c) UV-Vis absorbance and photoluminescence spectra of silicon nanoparticles dispersed in hexane.

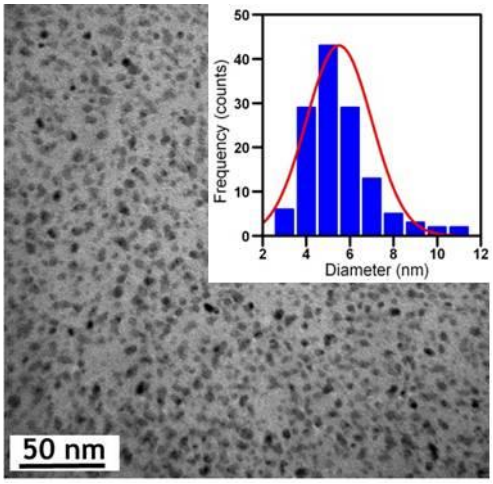

Figure 2.21: TEM image of Heptane-terminated silicon nanoparticles with rapid addition of precursor.

NCs. When the reducing agent was added in one rapid injection the mean size and size distribution of the nanocrystals changed dramatically, see Figure 2.21. The reason for the large dispersity in TEM image is because by changing the rate of addition of the reducing agent, the concentration of Si(0) is also altered. This confirms that the concentration of Si(0) in the solution at the initial stages of nanocrystals formation is critical in determining the ultimate size and size distribution of the Si NCs.

Scaling of the Si NC synthesis was carried out in collaboration with Sigma Aldrich Ltd as part of project requirements of the EC project SNAPSUN (grant agreement no. 246310), who performed DSC and TGA measurements of the scaled reaction process and the as-synthesised Si NCs, see Figures 2.22 and 2.23. The reaction calorimetry profile for the Heptane capped Si NCs was determined by an automated laboratory reactor, see Figure 2.22. Small exotherms were observed at ~ 3 °C and 7.5 °C during the addition of the hydride reducing agent ($LiAlH_4$) and the quencher methanol. Interestingly, the solvent toluene acts as a heat sink making the energy output difficult to calculate accurately. Figure 2.23 shows the Thermogravitic analysis of the silicon NCs. The weight loss occurs in two steps, starting at ~110 °C with a plateau at ~300 °C, with all weight loss completed at 500 °C.

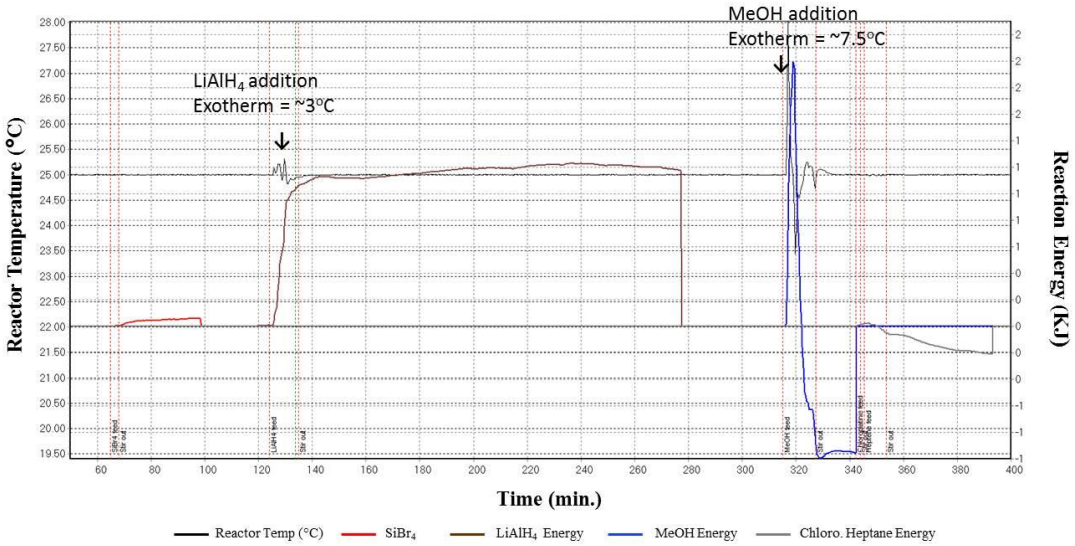

Figure 2.22: Reaction calorimetry profile for Heptane capped Si NCs as determined by automated laboratory reactor. (Graph courtesy of Sigma Aldrich)

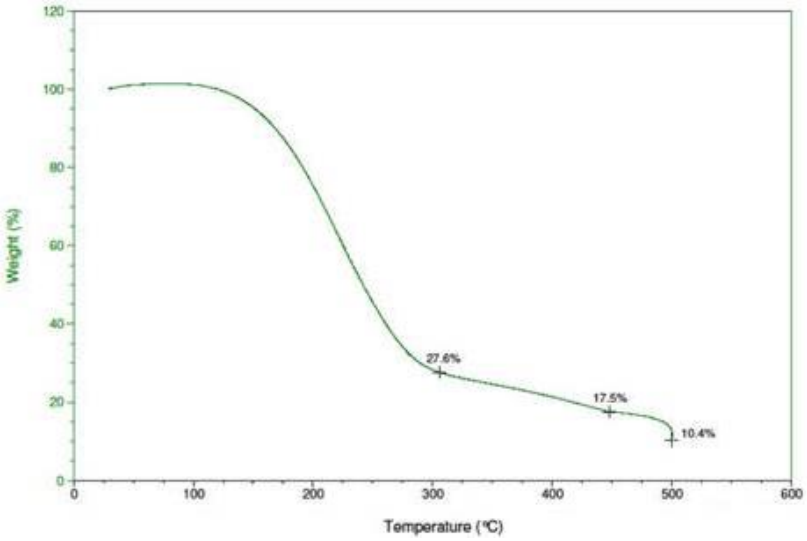

Figure 2.23: Thermogravametic analysis of the Heptane capped Si NCs. (Graph courtesy of Sigma Aldrich)

2.3.5 Allylamine Capped Silicon Nanocrystals

Amine terminated Si NCs were synthesised at room temperature by reduction of silicon tetrachloride using lithium aluminium hydride, see Table 2.1, Entry 10. Capping the Si NCs with an amine ligand allows the nanocrystals to be dispersed in variety of polar solvents. Figure 2.24 (a) shows the ligand passivation scheme procedure used to change the surface chemistry of the silicon quantum dots from hydrogen to allylamine. Figure 2.24(b) shows a low magnification TEM image of the allylamine capped Si NCs. The nanocrystals are highly size and shape monodisperse with no evidence of aggregation. Inset in Figure 2.24 (b) shows lattice fringes of 1.9 Å corresponding to 220 interplanar spacing of bulk silicon.

The low atomic weight of silicon relative to other metallic and semiconductor quantum dots combined with their extremely small dimensions resulted in low contrast in the HRTEM images. Figure 2.24 (c) shows a histogram of the nanocrystals diameter. Fitting a Gaussian model to the histogram yields a mean diameter of 2.0 ± 0.3 nm, agreeing well with the synthesis of alkyl capped Si NCs reported in section 2.3.1. Only by removing almost all of the surfactant (TOAB) could such small (1–2 nm) silicon quantum dots be imaged by HRTEM. Removal of surfactant is critical in achieving a high level of purification.

The surface chemistry of the Si NCs was characterized by infrared spectroscopy, see Figure 2.25. The spectrum was obtained from a fresh sample dissolved in chloroform. The peaks between *ca.* 3700-3500 cm^{-1} are assigned to the N-H stretching of the amine, while the peaks observed between 3000-2850 are attributed to C-H stretching modes. The features observed around 1604 to 1685 cm^{-1} are attributed to the N−H deformation modes of the amine. The peak at 1386 cm^{-1} is attributed to C-H bending signals. The peak at 1261 cm^{-1} is assigned to vibrational scissoring of the Si-CH_2 and highlights the strength and stability of the Si−C bond formed between the silicon nanoparticles and the allylamine.[34, 47] The features between 1000-1110 cm^{-1} are attributed to the vibrational stretching of Si-OR molecular components. The absence of bending band at *ca.* 1430 cm^{-1}, assigned to the quaternary ammonium ion (NR_4^+), indicates that the surfactant has been removed.[51]

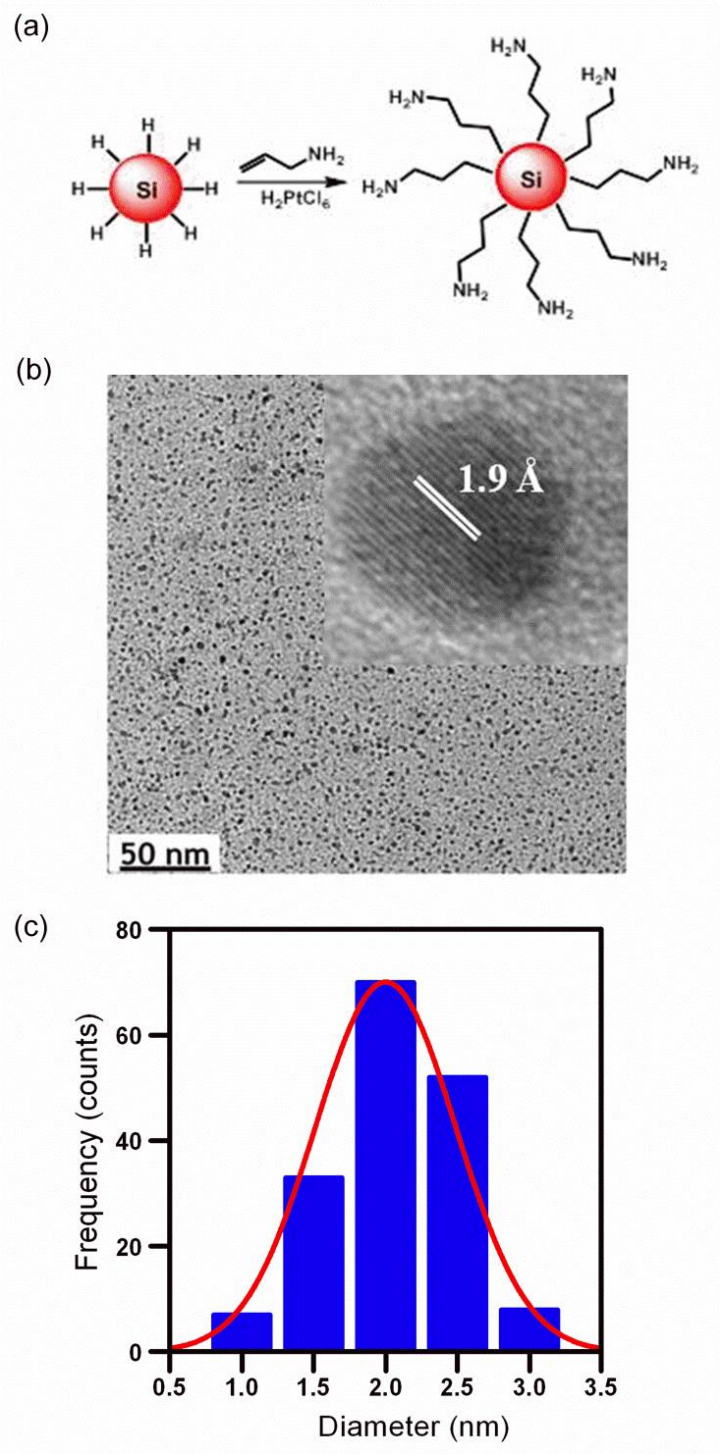

Figure 2.24: (a) Schematic procedure used to change the surface chemistry of the silicon quantum dots from hydrogen to allylamine (b) TEM images of allylamine capped silicon quantum dot. Inset shows high-resolution TEM image of a single nanocrystal. (c) Size histogram distribution of allylamine silicon.

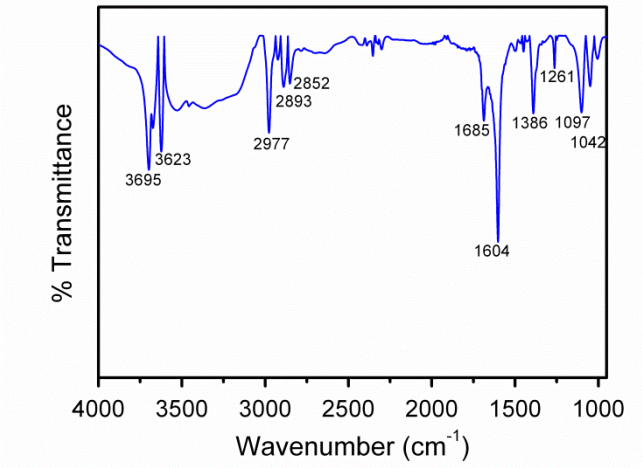

Figure 2.25: Fourier transform infrared spectrum of amine-terminated silicon nanocrystals.

The UV-Vis in Figure 2.26 (a), shows a peak at ~ 260 nm which is in good agreement with reports from Tilley *et al*.[29, 31] The allylamine capped Si NCs exhibit absorption over a range of 240- 350 nm with an onset of absorbance of 370 nm, attributed to direct band gap position. Interestingly the absorbance spectra shown in Figure 2.26 (a) is featureless in comparison to the alky terminated spectra observed in Section 2.3.1. Inset in Figure 2.26 (a) shows fluorescence from a vial of amine-capped silicon nanocrystals when excited with a UV lamp (365 nm). Figure 2.26(b) shows the photoluminescence spectra of the allylamine silicon nanocrystals.

Photoluminescence spectra were obtained using excitation wavelengths ranging from 320 to 400 nm in 20 nm intervals. The photoluminescence spectra of the allylamine-capped Si NCs have an emission peak at 400 nm for the 320 nm excitation and 460 nm for the 400 nm excitation. The photoluminescence spectra of the allylamine Si NCs differ from that of the heptane capped Si NCs. The spectra of the allylamine is much broader than that of the alkyl terminated, see Section 2.3.1. The allylamine Si NCs also displayed emission with lower energy emission than that of the heptane capped Si NCs. Further insights into the optical behaviour of the allylamine capped Si NCs can be obtained using time-resolved photoluminescence spectroscopy.

Photoluminescence quantum yield of the allylamine capped Si NCs in water were determined using the comparative method by Williams *et al;* see Figure 2.26 (c). The quantum yield was determined to be *ca.* 11% at an excitation wavelength of 320 nm.

The QY value is comparable to values obtained for Si NCs reported in the literature. [42, 43] Figure 2.27 shows the photoluminescence decay of the amine capped Si NCs in water. The photoluminescence decay required a three exponential fit with time constants of 1.0, 4.2 and 12.1 ns in agreement with report from the literature, [29] see Table 2.4, entry 4. The lifetimes of the amine Si NCs appear to be larger in comparison to the alkyl capped Si NCs. The difference in the dynamics of the PL decays and photoluminescence provides further evidence for different radiative recombination pathways for the allylamine and 1-heptene-capped Si NCs. The combination of all these optical measurements clearly indicates that the surface-capping molecule and environment strongly affect the optical properties of 1-2 nm Si NCs. Both the allylamine and 1-heptene-capped Si NCs have a Si-C surface bond and have photoluminescence in the blue region of the visible spectrum in agreement with the theoretical predictions of Zhou *et al*.[48]

The difference in the optical spectra of the Si NCs capped with allylamine as compared to 1-heptene may be related to the difference in the end termination group of the surface capping molecules. Allylamine is a short-chain polar molecule with an NH_2 termination at one end, whereas 1-heptene is a short-chain nonpolar molecule with a CH_3 termination. It is possible that the electronic charge distribution in the allylamine-capped Si NCs is modified by the polar nature of the allylamine in a similar way to that of a Si-O surface bond in 1-2 nm Si NCs. This may explain why the band gap of the allylamine-capped Si NCs is also slightly lower than that of the 1-heptene-capped Si NCs.

The Si NCs also exhibit excellent long-term PL stability, decreasing by less than 8 % after continuous illumination for 12 hours; see Figure 2.28(a). We also investigated the PL emission from the Si NCs dispersed in different organic solvents of varied polarity. The Si NCs were excited at 320 nm and kept at the same concentration for direct comparison. A red shift of ~ 10 nm was observed in PL emission maximum by increasing the solvent polarity from isopropanol to water, see Figure 2.28(b-c) and Table 2.6; demonstrating that the PL properties were sensitive to the medium surrounding the nanocrystals. This is in agreement with the work reported by Dasog *et al*, attributing the effect to an energy transfer excited state. [32]

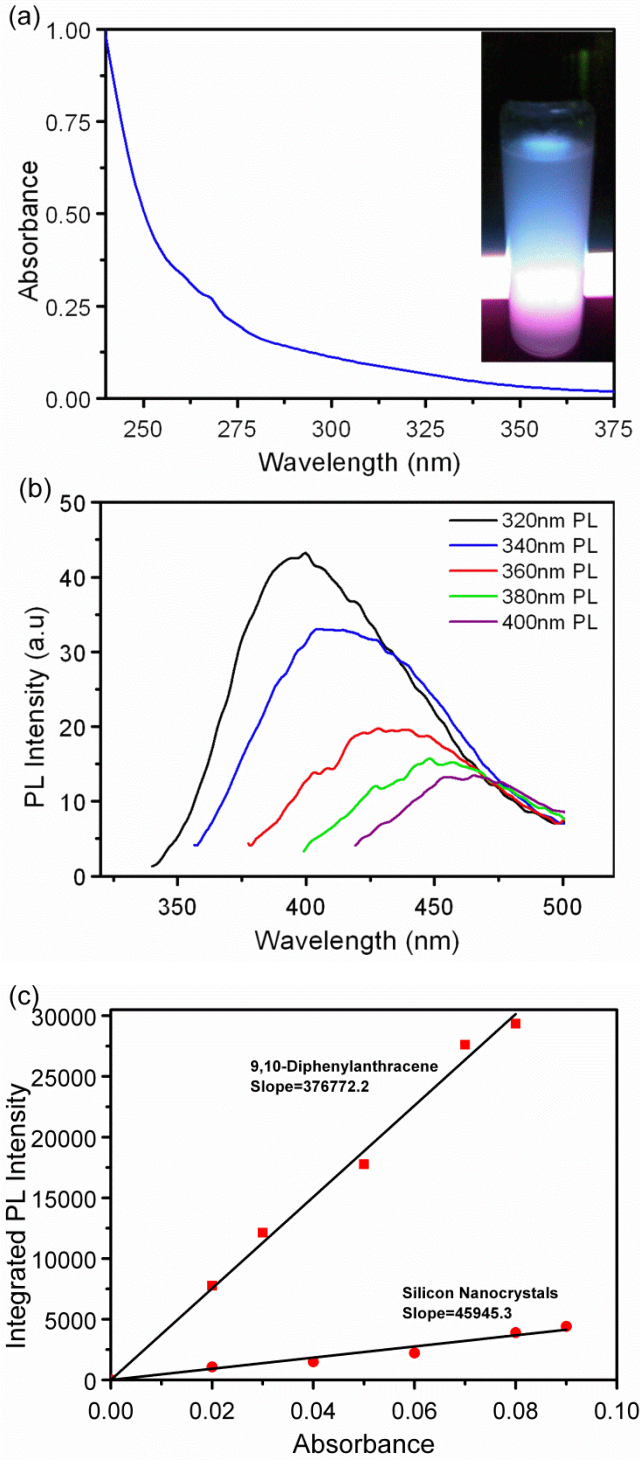

Figure 2.26: (a) UV-Vis absorption spectrum of allylamine capped silicon nanocrystals. Inset: show fluorescence from a vial of amine-capped silicon nanocrystals when excited with a UV lamp. (b) Photoluminescence spectra of allylamine capped silicon nanocrystals. (c)Integrated PL intensity *versus* absorbance for various dilute dispersions

of Si NCs in water and solutions of 9,10 diphenylanthracene recorded under identical excitation conditions.

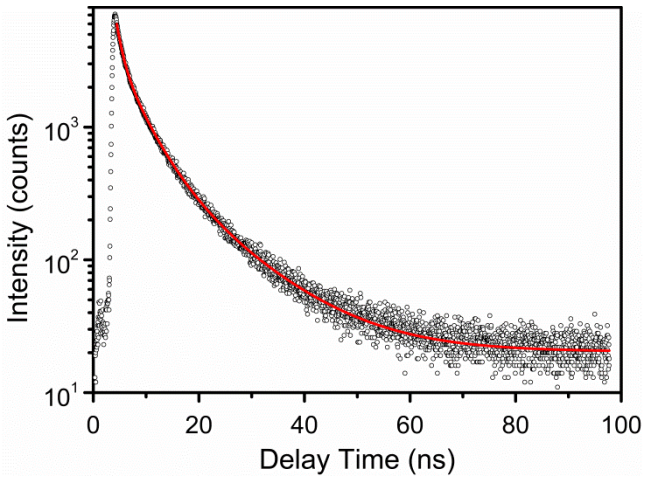

Figure 2.27: Photoluminescence decays of allylamine capped silicon nanocrystals in water.

It is well-known that the amine moiety can strongly quench the emission of semiconductor quantum dots under certain pH values[49], so it is interesting to investigate this phenomenon to determine the effect of pH upon the emission characteristics of amine-terminated Si NCs. This can be easily achieved *via* a variation of the pH, since this effectively transforms an $–NH_2$ moiety with a lone electron pair, available for electron donation, into an $–NH_3^+$ group that lacks this capability. With this in mind, we obtained PL spectra from Si NCs over a range of different pH values environments (4−14), and observed that the maximum emission peak position is independent of the pH, see Figure 2.29. This implies that the synthesized Si NCs remain stable in extremely acidic or in basic conditions and that the emission with protonated (nonquenching) and non-protonated (quenching) amine groups originates from the same state. At low pH the amine group is protonated, and electron transfer from the amine moieties to the Si core is prohibited, yielding higher emission intensity.[50] At higher pH, protonation is either incomplete or absent, which allows involvement of the nitrogen lone pair in relaxation processes and yields a reduced emission.[50]

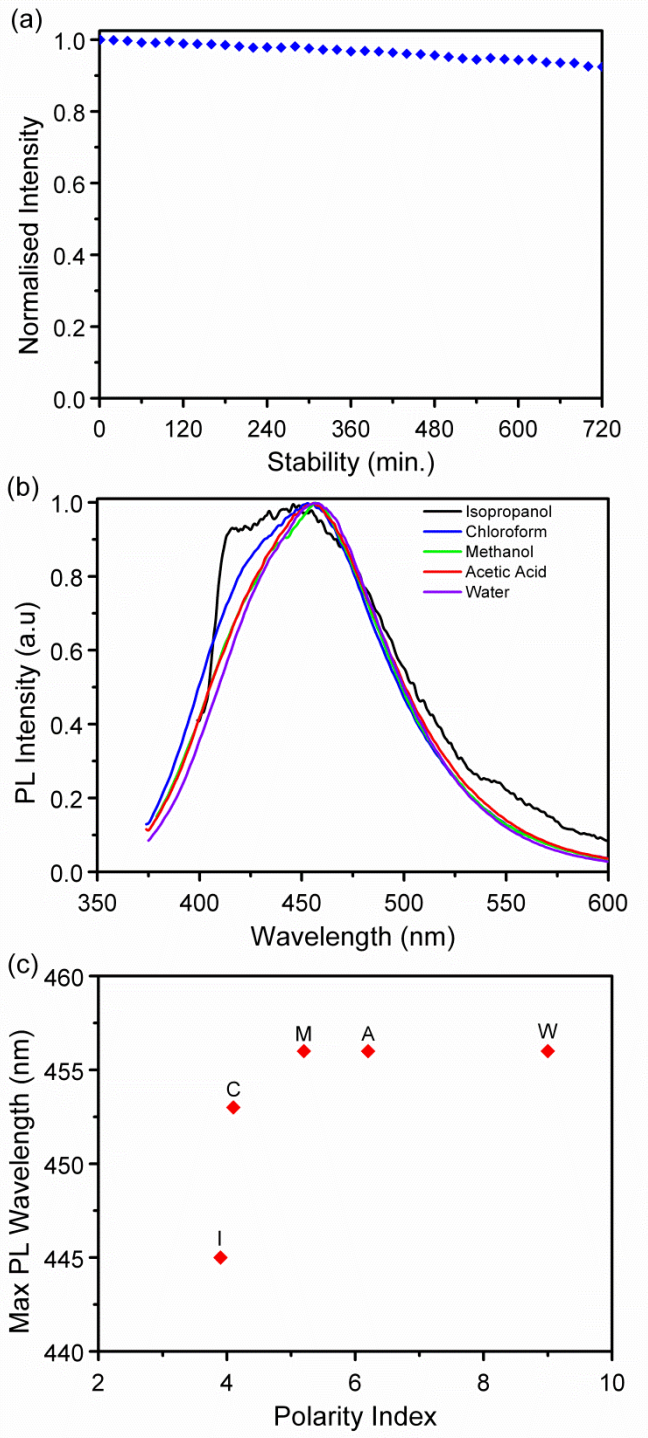

Figure 2.28: (a) Long term photoluminescence stability of amine-capped Si Ncs recorded over 12 hours using a 320 nm excitation. (b) Comparsion of the photoluminescence emission spectra of silicon nanocrystals in various polar solvents. (c) Normalised PL maximum *versus* Solvent polarity for different Si NCS at excitation 320 nm.

Table 2.6. A list of the polar solvent used in this study and their polar index constants.

Solvent	Symbol	Polarity Index
Isopropanol	I	3.9
Chloroform	C	4.1
Methanol	M	5.1
Acetic acid	A	6.2
Water	W	9.0

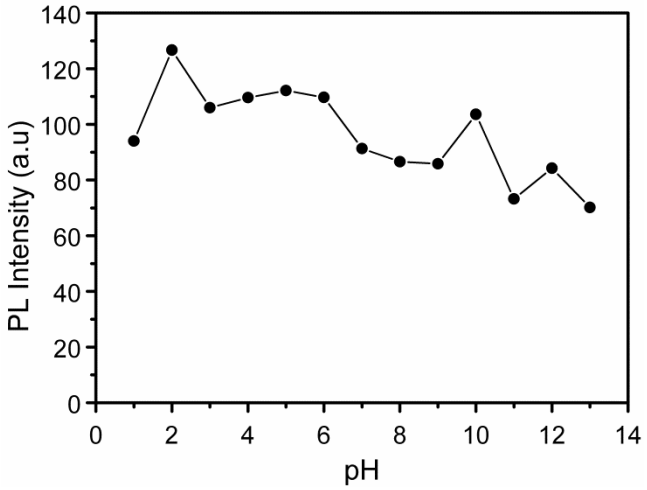

Figure 2.29: Integrated PL intensity of allylamine-terminated Si NCs recorded in different pH environments.

2.4 Conclusions

Size monodisperse silicon nanocrystals have been synthesized using a simple, room–temperature microemulsion synthesis method, with well-defined core diameters controlled between 2 to 6 nm by variation of the cationic quaternary ammonium salts used to form the inverse micelles. TEM imaging confirmed that the NCs are highly size and shape monodisperse, with no evidence of aggregation. High resolution TEM showed that the as-synthesised NCs were highly crystalline, while the crystal structure of Si was confirmed by selected area electron diffraction (SAED). FTIR and XPS spectroscopy confirmed that the Si NCs may be readily functionalised using a platinum-catalysed concerted coupling reaction, with minimal surface oxidation. UV-Vis and PL spectroscopy showed significant quantum confinement, with significant involvement of NC surface states in exciton recombination, demonstrated by absorption in the UV spectral range, and a strong blue emission with a marked dependency on excitation wavelength. Determination of the photoluminescence quantum yield (Φ) of the Si NCs showed an inverse relationship with the NC core diameter, with a maximum of 12 % measured for 2 nm NCs. The Si NCs exhibited lifetimes in the nanosecond regime with long term resistance to oxidation and excellent photostability.

The advantage of using this synthetic approach is that is an inherently scalable method, which does not require rapid mixing of chemical precursors or high reaction temperature. It was shown that a ten-fold increase in precursor concentration had no effect on the properties of the Si NCs. NCs formed using non-ionic surfactants, also showed narrow size distributions and similar optical properties, indicating that the surfactant type does not affect the quality of the NCs. Complete removal of the surfactant resulted in only a slight increase in NC size, with no change in the optical spectra, indicating that the photophysical characteristics of the Si NCs are determined by their surface chemistries. In contrast, PL spectra of similarly sized Si NCs prepared with allylamine terminated surfaces exhibited significant differences in their optical spectra, indicating strong involvement of surface states in NC exciton generation and recombination processes.

2.5 References:

1. Green, M., Semiconductor Quantum Dots as Biological Imaging Agents. *Angewandte Chemie International Edition* **2004**, *43*, 4129-4131.

2. Bruchez, M.; Moronne, M.; Gin, P.; Weiss, S.; Alivisatos, A. P., Semiconductor nanocrystals as fluorescent biological labels. *Science* **1998**, *281*, 2013-2016.

3. Anikeeva, P. O.; Halpert, J. E.; Bawendi, M. G.; Bulovic, V., Quantum dot light-emitting devices with electroluminescence tunable over the entire visible spectrum. *Nano Letters* **2009**, *9*, 2532-2536.

4. Coe, S.; Woo, W. K.; Bawendi, M.; Bulovic, V., Electroluminescence from single monolayers of nanocrystals in molecular organic devices. *Nature* **2002**, *420*, 800-803.

5. Brus, L. E., Electron–electron and electron-hole interactions in small semiconductor crystallites: The size dependence of the lowest excited electronic state. *Journal of Chemical Physics* **1984**, *80*, 4403-4409.

6. Talapin, D. V.; Lee, J.S.; Kovalenko, M. V.; Shevchenko, E. V., Prospects of colloidal nanocrystals for electronic and optoelectronic applications. *Chemical Reviews* **2009**, *110*, 389-458.

7. Cullis, A. G.; Canham, L. T.; Calcott, P. D. J., The structural and luminescence properties of porous silicon. *Journal of Applied Physics* **1997**, *82*, 909-965.

8. Pavesi, L.; Dal Negro, L.; Mazzoleni, C.; Franzo, G.; Priolo, F., Optical gain in silicon nanocrystals. *Nature* **2000**, *408*, 440-444.

9. Ding, Z.; Quinn, B. M.; Haram, S. K.; Pell, L. E.; Korgel, B. A.; Bard, A. J., Electrochemistry and electrogenerated chemiluminescence from silicon nanocrystal quantum dots. *Science* **2002**, *296*, 1293-1297.

10. Nirmal, M.; Brus, L., Luminescence Photophysics in Semiconductor Nanocrystals. *Accounts of Chemical Research* **1998**, *32*, 407-414.

11. Holec, T.; Chvojka, T.; Jelínek, I.; Jindřich, J.; Němec, I.; Pelant, I.; Valenta, J.; Dian, J., Determination of sensoric parameters of porous silicon in sensing of organic vapors. *Materials Science and Engineering: C* **2002**, *19*, 251-254.

12. Sailor, M. J.; Lee, E. J., Surface chemistry of luminescent silicon nanocrystallites. *Advanced Materials* **1997**, *9*, 783-793.

13. Cheng, K. Y.; Anthony, R.; Kortshagen, U. R.; Holmes, R. J., Hybrid silicon nanocrystal−organic light-emitting devices for infrared electroluminescence. *Nano Letters* **2010**, *10*, 1154-1157.

14. Cheng, K. Y.; Anthony, R.; Kortshagen, U. R.; Holmes, R. J., High-Efficiency silicon nanocrystal light-emitting devices. *Nano Letters* **2011**, *11*, 1952-1956.

15. Maier-Flaig, F.; Rinck, J.; Stephan, M.; Bocksrocker, T.; Bruns, M.; Kübel, C.; Powell, A. K.; Ozin, G. A.; Lemmer, U., Multicolor Silicon light-emitting diodes (SiLEDs). *Nano Letters* **2013**, *13*,475-480.

16. Mastronardi, M. L.; Henderson, E. J.; Puzzo, D. P.; Chang, Y.; Wang, Z. B.; Helander, M. G.; Jeong, J.; Kherani, N. P.; Lu, Z.; Ozin, G. A., Silicon nanocrystal oleds: effect of organic capping group on performance. *Small* **2012**, *8*, 3647-3654.

17. Puzzo, D. P.; Henderson, E. J.; Helander, M. G.; Wang, Z.; Ozin, G. A.; Lu, Z., Visible colloidal nanocrystal silicon light-emitting diode. *Nano Letters* **2011**, *11*, 1585-1590.

18. Tu, C.C.; Tang, L.; Huang, J.; Voutsas, A.; Lin, L. Y., Visible electroluminescence from hybrid colloidal silicon quantum dot-organic light-emitting diodes. *Applied Physics Letters* **2011**, *98*, 213102-3.

19. Tilley, R. D.; Warner, J. H.; Yamamoto, K.; Matsui, I.; Fujimori, H., Micro-emulsion synthesis of monodisperse surface stabilized silicon nanocrystals. *Chemical Communications* **2005**, 1833-1835.

20. Huber, D. L.; Wilcoxon, J. P.; Samara, G. A., Erratum: Tailorable, visible light emission from silicon nanocrystals. *Applied Physics Letters* **2008**, *92*, 029902-1.

21. Williams, A. T. R.; Winfield, S. A.; Miller, J. N., Relative fluorescence quantum yields using a computer-controlled luminescence spectrometer. *Analyst* **1983**, *108*, 1067-1071.

22. Robbins, R. J.; Fleming, G. R.; Beddard, G. S.; Robinson, G. W.; Thistlethwaite, P. J.; Woolfe, G. J., Photophysics of aqueous tryptophan: pH and temperature effects. *Journal of the American Chemical Society* **1980**, *102*, 6271-6279.

23. Hamai, S.; Hirayama, F., Actinometric determination of absolute fluorescence quantum yields. *The Journal of Physical Chemistry* **1983**, *87*, 83-89.

24. Rosso-Vasic, M.; Spruijt, E.; van Lagen, B.; De Cola, L.; Zuilhof, H., Alkyl-functionalized oxide-free silicon nanoparticles: synthesis and optical properties. *Small* **2008**, *4*, 1835-1841.

25. Germanenko, I. N. D., M.; Pithawalla,Y. B.; El-Shall M.S.; Carlisle, J. A., Effect of atmospheric oxidation on the electronic and photoluminscence properties of silicon nanocrystals. *Pure and Applied Chemistry* **2000**, *72*, 245-255.

26. Perraud, S.; Quesnel, E.; Parola, S.; Barbé, J.; Muffato, V.; Faucherand, P.; Morin, C.; Jarolimek, K.; Van Swaaij, R. A. C. M. M.; Zeman, M.; Richards, S.; Kingsley, A.; Doyle, H.; Linehan, K.; O'Brien, S.; Povey, I. M.; Pemble, M. E.; Xie, L.; Leifer, K.; Makasheva, K.; Despax, B., Silicon nanocrystals: Novel synthesis routes for photovoltaic applications. *Physica Status Solidi (a)* **2013**, *210*, 649-657.

27. Chao, Y.; Siller, L.; Krishnamurthy, S.; Coxon, P. R.; Bangert, U.; Gass, M.; Kjeldgaard, L.; Patole, S. N.; Lie, L. H.; O'Farrell, N.; Alsop, T. A.; Houlton, A.; Horrocks, B. R., Evaporation and deposition of alkyl-capped silicon nanocrystals in ultrahigh vacuum. *Nature Nanotechnology* **2007**, *2*, 486-489.

28. Wilcoxon, J. P.; Samara, G. A.; Provencio, P. N., Optical and electronic properties of Si nanoclusters synthesized in inverse micelles. *Physical Review B* **1999**, *60*, 2704.

29. Warner, J. H.; Rubinsztein-Dunlop, H.; Tilley, R. D., Surface morphology dependent photoluminescence from colloidal silicon nanocrystals. *Journal of Physical Chemistry B* **2005**, *109*, 19064-19067.

30. Rosso-Vasic, M.; Spruijt, E.; Lagen, B. v.; Cola, L. D.; Zuilhof, H., Alkyl-functionalized oxide-free silicon nanoparticles: synthesis and optical properties. *Small* **2009**, *5*, 2637.

31. Shiohara, A.; Prabakar, S.; Faramus, A.; Hsu, C. Y.; Lai, P. S.; Northcote, P. T.; Tilley, R. D., Sized controlled synthesis, purification, and cell studies with silicon quantum dots. *Nanoscale* **2011**, *3*, 3364-3370.

32. Dasog, M.; Yang, Z.; Regli, S.; Atkins, T. M.; Faramus, A.; Singh, M. P.; Muthuswamy, E.; Kauzlarich, S. M.; Tilley, R. D.; Veinot, J. G. C., Chemical insight into the origin of red and blue photoluminescence arising from freestanding silicon nanocrystals. *ACS Nano* **2013**, *7*, 2676-2685.

33. Yang, C. S.; Bley, R. A.; Kauzlarich, S. M.; Lee, H. W. H.; Delgado, G. R., Synthesis of alkyl-terminated silicon nanoclusters by a solution route. *Journal of the American Chemical Society* **1999**, *121*, 5191-5195.

34. Shiohara, A.; Hanada, S.; Prabakar, S.; Fujioka, K.; Lim, T. H.; Yamamoto, K.; Northcote, P. T.; Tilley, R. D., Chemical Reactions on Surface Molecules Attached to Silicon Quantum Dots. *Journal of the American Chemical Society* **2010**, *132*, 248-253.

35. Veinot, J. G. C., Synthesis, surface functionalization, and properties of freestanding silicon nanocrystals. *Chemical Communications* **2006**, 4160-4168.

36. Shirahata, N., Colloidal Si nanocrystals: a controlled organic-inorganic interface and its implications of color-tuning and chemical design toward sophisticated architectures. *Physical Chemistry Chemical Physics* **2011**, *13*, 7284-7294.

37. Saar, A., Photoluminescence from silicon nanostructures: The mutual role of quantum confinement and surface chemistry. *Journal of Nanophotonics* **2009**, *3*, 032501-032501.

38. Yang, S.; Li, W.; Cao, B.; Zeng, H.; Cai, W., Origin of Blue Emission from Silicon Nanoparticles: Direct Transition and Interface Recombination. *Journal of Physical Chemistry C* **2011**, *115*, 21056-21062.

39. Pradhan, S.; Chen, S.; Zou, J.; Kauzlarich, S. M., Photoconductivity of langmuir−blodgett monolayers of silicon nanoparticles. *Journal of Physical Chemistry C* **2008**, *112*, 13292-13298.

40. Siekierzycka, J. R.; Rosso-Vasic, M.; Zuilhof, H.; Brouwer, A. M., Photophysics of n-butyl-capped silicon nanoparticles. *Journal of Physical Chemistry C* **2011**, *115*, 20888.

41. Yang, S.T.; Wang, X.; Wang, H.; Lu, F.; Luo, P. G.; Cao, L.; Meziani, M. J.; Liu, J.H.; Liu, Y.; Chen, M.; Huang, Y.; Sun, Y. P., Carbon Dots as nontoxic and high-performance fluorescence imaging agents. *Journal of Physical Chemistry C* **2009**, *113*, 18110-18114.

42. Lin, S. W.; Chen, D. H., Synthesis of Water-Soluble Blue Photoluminescent Silicon Nanocrystals with Oxide Surface Passivation. *Small* **2009**, *5*, 72-76.

43. Warner, J. H.; Hoshino, A.; Yamamoto, K.; Tilley, R. D., Water-Soluble photoluminescent silicon quantum dots. *Angewandte Chemie International Edition* **2005**, *44*, 4550-4554.

44. Gerion, D.; Pinaud, F.; Williams, S. C.; Parak, W. J.; Zanchet, D.; Weiss, S.; Alivisatos, A. P., Synthesis and properties of biocompatible water-soluble silica-coated cdse/zns semiconductor quantum dots. *The Journal of Physical Chemistry B* **2001**, *105*, 8861-8871.

45. Miller, R. D.; Michl, J., Polysilane high polymers. *Chemical Reviews* **1989**, *89*, 1359-1410.

46. Pileni, M. P., The role of soft colloidal templates in controlling the size and shape of inorganic nanocrystals. *Nature Materials* **2003**, *2*, 145-150.

47. Ahire, J. H.; Wang, Q.; Coxon, P. R.; Malhotra, G.; Brydson, R.; Chen, R.; Chao, Y., Highly luminescent and nontoxic amine-capped nanoparticles from porous silicon: synthesis and their use in biomedical imaging. *ACS Applied Materials & Interfaces* **2012**, *4*, 3285-3292.

48. Zhou, Z.; Brus, L.; Friesner, R., Electronic structure and luminescence of 1.1- and 1.4-nm silicon nanocrystals: oxide shell *versus* hydrogen passivation. *Nano Letters* **2003**, *3*, 163-167.

49. Landes, C. F.; Braun, M.; El-Sayed, M. A., On the nanoparticle to molecular size transition: fluorescence quenching studies. *The Journal of Physical Chemistry B* **2001**, *105*, 10554-10558.

50. Rosso-Vasic, M.; Spruijt, E.; Popovic, Z.; Overgaag, K.; van Lagen, B.; Grandidier, B.; Vanmaekelbergh, D.; Dominguez-Gutierrez, D.; De Cola, L.; Zuilhof, H., Amine-terminated silicon nanoparticles: synthesis, optical properties and their use in bioimaging. *Journal of Materials Chemistry* **2009**, *19*, 5926-5933.

51. Silverstein, R. M.; Webster, F. X.; Kiemle, D. J. Spectrometric Identification of Organic Compounds, Seventh Ed., *Wiley & Sons*, **2005**.

Chapter 3

Synthesis and Characterisation of Carbon Quantum Dots

3.1 Introduction

The recent emergence of carbon quantum dots (CQDs) as a versatile fluorescence nanomaterial has garnered widespread interest due to their attractive photo-physical properties, high quantum yield, low toxicity and biocompatibility.[1-3] Compared to conventional organic dyes and semiconductor quantum dots, CQDs possess several advantages in terms of chemical inertness, easy functionalisation, high resistance to photobleaching, an absence of fluorescence intermittency and the potential for low cost production. As a result, much attention has been paid to their potential application in areas ranging from biological labelling and imaging to fluorescence nanosensors and optoelectronic devices.[2, 4, 5] Despite the great potential of this material, size and shape control for CQDs remains less developed than those for II-VI, IV-VI and III-V semiconductors.

The ability to control the size and tailor the surface chemistry of the CQDs would facilitate in the understanding of size dependent phenomena and quantum confinement behaviour. Biological applications such as bio-sensing and cell imaging require tuning the optoelectronic and surface properties, thus controlling the size distribution is of the utmost importance. Moreover, for CQDs to be used effectively in many biological applications, it is essential that the quantum dots are water-soluble, stable against aggregation and precipitation within a biological system, possess a high photoluminescence quantum yield in the visible region and exhibit excellent photo stability under typical illumination conditions. A number of different synthetic strategies have been developed and reported for the preparation of CQDs, which may be divided into both physical and chemical methods.

Physical methods include arc discharge,[6] laser ablation/passivation[7, 8] and plasma treatment.[9] Chemical methods include electrochemical synthesis,[10-12] combustion and acidic oxidation,[13, 14] hydrothermal and pyrolysis routes,[15] supported synthesis[16-18] and microwave/ultrasonic synthesis.[19, 20] However, some drawbacks associated these methods include extensive post-synthetic purification, lack of control of CQD surface chemistry and sample polydispersity.[1]Although a large variety of methods exists in the literature for the preparation of CQDs, very few report exists for simultaneously controlling the size and tailoring the surface chemistry of the CQDs. Kang *et al*.

developed a current density controlled electrochemical method to control the size of the CQDs, however the size distribution of the CQDs remained broad.[21] Jana *et al.* developed a chemical method to synthesis highly fluorescence carbon nanoparticles which exhibited size dependent and tunable emission in the visible region at temperatures ranging from 80 – 300°C.[22] Whilst some of these methods have had some varying degree of success at controlling the size, key aspects such as tailoring the surface chemistry still needs to be improved. The use of microemulsion based synthetic methods have been the most promising due to their ability to control the size, shape and surface chemistry of the CQDs. Rhee and co-workers reported the solution-phase synthesis of CQDs using reverse micelles as nanoscale reactors *via* condensation polymerisation and subsequent carbonization of glucose within sodium di-2-ethylhexyl sulfosuccinate reverse micelles at 160 ºC. [23]

Control of the water-surfactant ratio within the micelle allowed the CQD diameter to be tuned from 1.8 to 4.1 nm, but with increasing polydispersity at larger diameters. Recently, Rhee *et al* reported the synthesis of size tunable CQD using a soft template method. The size of the CQDs was controlled by regulating the amount of the emulsifier.[24] Gao *et al.* reported on the hydrothermal synthesis of CQDs by oxidation of C_{60} by hydrogen peroxide under alkaline conditions within cetyltrimethylammonium bromide (CTAB) reverse micelles at 150 ºC.[25] With this in mind, our aim was to develop a synthetic method that permits both control over the size and surface, and allows for the high crystallinity and monodispersity within the material.

In this chapter†, we report a simple solution phase synthesis of size monodisperse CQDs using a room temperature microemulsion strategy. The CQDs are synthesized in reverse micelles *via* the reduction of carbon tetrachloride using a hydride reducing agent. The hydrogen-terminated CQDs are functionalised using a platinum-catalysed concerted reaction to covalently attach either a alkyl or amine monolayer, rendering the CQDs dispersible in wide range of polar or non-polar solvents. The CQDs possess a high photoluminescence quantum yield in the visible region and exhibit excellent photostability. In addition, we also report a method for the size controlled synthesis of CQDs within reverse micelles having well defined core diameters ranging from 2 to 6 nm. The CQDs are chemically passivated and made water soluble using an allylamine

ligand. Regulation of the CQDs size was achieved by utilizing hydride reducing agents of different strengths. Through controlling the size of the CQDs, their resulting photoluminescence properties could be tuned.

† Publications arising from this work are:

(i) "Efficient one pot synthesis of highly monodisperse alkyl functionalized CQDs dots," *RSC Advances*, **2014**, 4, 18-21.

(ii) "Solution reduction synthesis of amine terminated carbon quantum dots," *RSC Advances* **2014**, 4, 12094-12097.

(iii) "Size controlled synthesis of carbon quantum dots using hydride reducing agents," *Journal of Material Chemistry C* **2014**, 2, 6025-6031.

3.2 Experimental

3.2.1 Synthesis and Purification of Carbon Quantum Dots

All glassware used was cleaned by thoroughly soaking in a base bath overnight, followed by immersion in piranha solution (3:1 concentrated sulphuric acid: 30 % hydrogen peroxide) for 20 min. All reagents and solvents were purchased from Sigma-Aldrich Ltd. and used as received. In an inert atmosphere glove-box, 5.49 mmol of tetraoctyl ammonium bromide (TOAB) was dissolved in 100 mL anhydrous toluene. 0.2 mL (2.07 mmol) CCl_4 was then added to the solution and left to stir for 30 min. Carbon quantum dots (CQDs) were then formed by the dropwise addition of 4 mL of 1 M lithium aluminium hydride in THF over a period of 5 min. The solution was then left to stir for 30 min. The excess reducing agent was quenched with the addition of 30 mL of methanol, upon which the dispersion became transparent. At this stage of the reaction the CQDs are terminated by hydrogen and encapsulated within the reverse micelle.

Chemically passivated CQDs were formed by modifying the carbon-hydrogen bonds at the surface *via* the addition of 200 µL of a 0.1 M H_2PtCl_6 in isopropyl alcohol as a catalyst, followed by 3 mL of 1-dodecene, see Scheme 3.1. After stirring for 30 min, the CQDs were removed from the glove box and the organic solvent removed by rotary evaporation. The resulting dry powder (consisting mainly of surfactant) was then re-dispersed in 50 mL hexane and sonicated for 30 min. The solution was then filtered twice using both filter paper and PVDF membrane filters (MILLEX-HV, Millipore, 0.45 µm) to remove the surfactant, after which it was washed with 100 mL of deionised water (3 times).

Alkyl-terminated CQDs remain in the hexane phase. In addition to synthesizing dodecane capped CQDs, amine terminated CQDs were synthesised in a similar manner and the resulting CQDs were dispersed in deionised water. Amine capped CQDs were purified by filtering twice using both filter paper and PVDF membrane filters (MILLEX-HV, Millipore, 0.45 µm) to remove the surfactant. Overall the synthesis allows for the CQDs to be dispersed in a variety of polar and non-polar solvents. Table 3.1 shows a summary of the reactions studied in this work and the various synthetic parameters used for the formation of Si NCs.

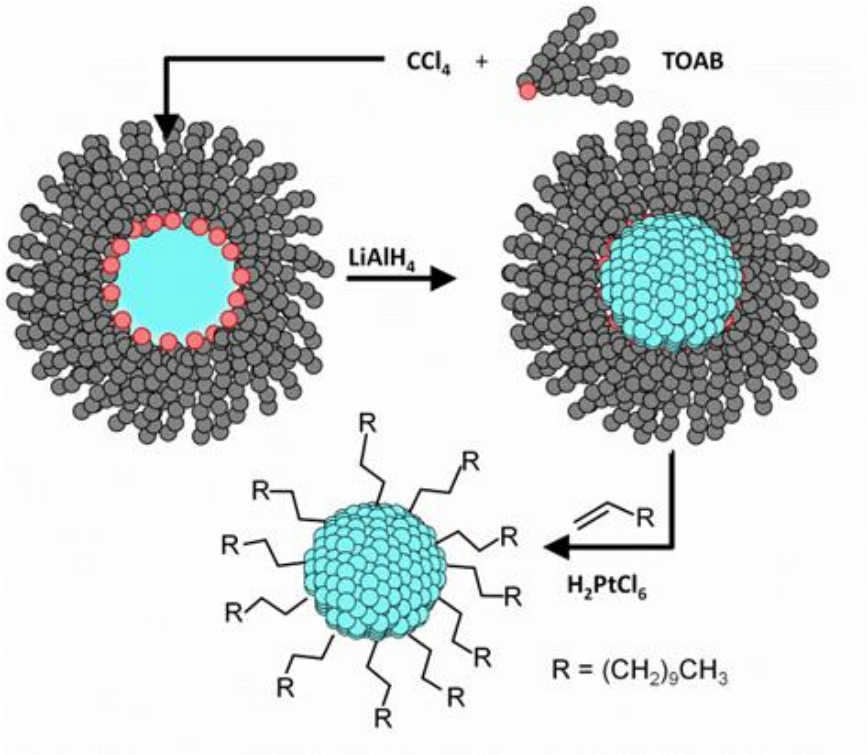

Scheme 3.1. Synthesis of 1-dodecane terminated carbon quantum dots.

3.2.2 Optical Characterization

Ultraviolet-Visible (UV-Vis) absorption spectra were recorded using a Shimadzu UV PC-2401 spectrophotometer equipped with a 60 mm integrating sphere (ISR- 240A, Shimadzu). Absorption spectra were recorded at room temperature using a quartz cuvette (1 cm) and corrected for the solvent absorption.

Photoluminescence (PL) spectra of optically dilute solutions (optical density 0.01 - 0.1) were acquired on a Cary Eclipse luminescence spectrophotometer equipped with a pulsed Xenon discharge lamp. Samples were measured directly in a quartz fluorescence cuvette with 4 polished sides, a path length of 10 mm and a volume of 3.5 mL. The cuvette was thoroughly washed at least twice each with acetone, methanol, deionized water and the solvent to be used before measurements. The spectra were corrected by measuring emission from the solvent and then subtracting this from the samples. Long-term PL stability measurements on alkyl terminated CQDs were carried out using an excitation wavelength of 290 nm, and recorded with a total integration time of 50 s, with a “dark” interval of 10 s between successive measurements (83 % duty cycle). All

spectra were integrated between 300 and 475 nm for comparison. For amine terminated quantum dots, long-term PL stability measurements were carried out using an excitation wavelength of 380 nm, and recorded with a total integration time of 60 s. All spectra were integrated between 400 and 550 nm for comparison.

Photoluminescence lifetime measurements were recorded on a scanning confocal fluorescence microscope (MicroTime 200, PicoQuant GmbH) equipped with a TimeHarp 200 TCSPC board. All CQD samples were excited using a 402 nm pulsed diode laser (10 MHz; 70 ps pulse duration, LDH-P-C-400) that was spectrally filtered using a 405 nm band-pass filter (Z405/10x, Chroma Technology Corp.). A 50X objective (0.5 NA; LM Plan FL, Olympus Corp.) was used for focusing the excitation light onto the NC dispersion and collecting the resultant fluorescence, which was directed onto an avalanche photodiode (APD; SPCM-AQR-14, Perkin-Elmer, Inc.). Backscattered excitation light was blocked with a 410 nm long-pass filter placed in the collection path (3RD410LP, Omega Optical). The excitation power was adjusted to maintain a count rate of $< 10^4$ counts/s at the APD in order to preserve single photon counting statistics. All emission lifetimes were fitted with a weighted multi-exponential model on FluoFit 4.2 software (PicoQuant GmbH). All lifetimes were fitted with a χ^2 value of less than 1.3.

Quantum yields (QY) were measured using the comparative method described by Williams *et al*.[26] The quantum yield of the amine-capped CQDs was calculated using 9, 10 diphenyl anthracene (literature quantum yield of 90 % at 320 nm)[27] as the standard. Dilute dispersions of the CQDs in deionised water were prepared with optical densities between 0.01 – 0.1. Linear regression analysis was employed to determine the relative PL intensities of the sample and reference solutions over the range of concentrations, allowing the quantum yield of the CQDs. The quantum yields were then calculated using the Equation 3.1:

$$\Phi_x = \Phi_R \left(\frac{m_x}{m_R} \right) \left(\frac{\eta_x^2}{\eta_R^2} \right) \tag{3.1}$$

Where Φ is the quantum yield, m is the slope from the plot of integrated fluorescence intensity *versus* absorbance and η is the refractive index. The subscript R refers to the

reference material of the known standard while x indicates the unknown species to be calculated.

3.2.3 TEM, FTIR and XPS Characterisation

Transmission electron microscopy (TEM) images and selective area electron diffraction patterns (SAED) were acquired using a high-resolution JEOL 2100 electron microscope, equipped with a LAB_6 electron source and Gatan DualVision 600 Charge-Coupled Device (CCD), operating at an accelerating voltage of 200 keV. TEM samples were prepared by depositing 100 μl of CQD dispersion onto a holey carbon coated TEM grid (400-mesh, #S147-3H, Agar Scientific). Particle size analysis of TEM images was carried out using the Particle Size Analyzer macro (r12, freely available online at http://code.google.com/p/psa-macro/) running on Image J software.

X-ray photoelectron spectroscopy (XPS) measurements of the amine terminated CQDs were carried out using a Kratos Ultra DLD photoelectron spectrometer. The narrow scan spectra were obtained under high vacuum conditions by using a monochromatic Al Kα x-ray radiation at 15 kV and 10 mA with an analyzer pass energy of 20 eV. Substrates were cleaned for 20 min in piranha solution, rinsed with water and dried with nitrogen. A few drops of the CQD solution dissolved in chloroform were dropped on a clean gold surface substrate. All spectra were acquired at room temperature and binding energies were referenced to the Au $4f_{7/2}$ line. All spectra were corrected using a Shirley background.

FT-IR spectra were recorded using a liquid cell with NaCl windows on a Perkin Elmer Two spectrometer. Samples were formed by placing an aliquot of CQDs dispersed in hexane onto NaCl plates, after which the sample was allowed to evaporate to dryness. For amine terminated CQDs, CaF_2 windows was used in the liquid cell.

Table 3.1. A list of the chemical reactions undertaken and the experimental parameters used for the formation of Carbon Quantum Dots (CQDs).

Entry	Precursor	Surfactant	Solvent (anhydrous)	Reducing agent	Chemical Quencher (anhydrous)	Catalyst	Ligand
1	CCl_4 (0.1 mL)	TOAB (3.0 g)	Toluene (100 mL)	1 M Lithium Aluminium hydride in THF (4 mL)	Methanol (30 mL)	0.1 M Chloroplatinic acid in IPA (0.2 mL)	1-dodecene (3 mL)
2	CCl_4 (0.2 mL)	TOAB (3.0 g)	Toluene (100 mL)	1 M Lithium Aluminium hydride in THF (4 mL)	Methanol (30 mL)	0.1 M Chloroplatinic acid in IPA (0.2 mL)	Allylamine (4 mL)
3	CCl_4 (0.2 mL)	TOAB (3.2 g)	Toluene (100 mL)	1 M Lithium Aluminium hydride in THF 6 mmol)	Methanol (50 mL)	0.1 M Chloroplatinic acid in IPA (0.2 mL)	Allylamine (6 mL)
4	CCl_4 (0.2 mL)	TOAB (3.2 g)	Toluene (100 mL)	1 M Lithium Triethylboro hydride in THF 6 mmol)	Methanol (50 mL)	0.1 M Chloroplatinic acid in IPA (0.2 mL)	Allylamine (6 mL)
5	CCl_4 (0.2 mL)	TOAB (3.2 g)	Toluene (100 mL)	1 M Lithium tri-sec-butylboro hydride in THF (6 mmol)	Methanol (50 mL)	0.1 M Chloroplatinic acid in IPA (0.2 mL)	Allylamine (6 mL)
6	CCl_4 (0.2 mL)	TOAB (3.2g)	Toluene (100 mL)	1 M Lithium Boro hydride in THF 6 mmol)	Methanol (50 mL)	0.1 M Chloroplatinic acid in IPA (0.2 mL)	Allylamine (6 mL)

3.3 Results and Discussion

3.3.1 Synthesis of Alkyl Terminated Carbon Quantum Dots

Alkyl-terminated CQDs were synthesised by room temperature reduction of carbon tetrachloride by lithium aluminium hydride under inert atmosphere; see Experimental Section 3.2.1 and Table 3.1 (entry 1) for synthetic details. Figure 3.1(a) shows a transmission electron microscope (TEM) image of the as-synthesized CQDs. The CQDs are highly size and shape monodisperse with no evidence of aggregation. Inset in Figure 3.1(a) is a high resolution TEM image showing that the CQDs are highly crystalline with a lattice spacing of 2.1 Å, in excellent agreement with the (100) spacing reported for graphitic carbon. Figure 3.1(b) shows a histogram of the CQD diameters, determined by analysis of TEM images of *ca.* 250 CQDs located at different locations on the grid. The mean diameter of the CQDs is 1.5 ± 0.3 nm, based on fitting the histogram to a Gaussian model.

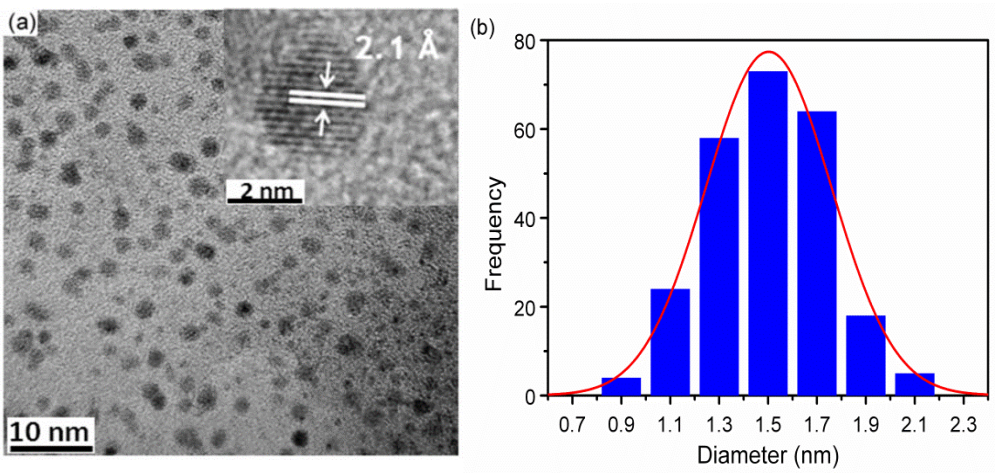

Figure 3.1: (a) Representative TEM image of the carbon quantum dots. Inset: high–resolution TEM image of an individual CQD. (b) Size histogram of the CQDs with curve fitted to the data using a Gaussian model.

The surface chemistry of the CQDs was characterized by infrared spectroscopy; Figure 3.2 shows the FTIR spectra of 1-dodecene and the as-synthesised CQDs. Both spectra exhibit strong C-H vibrational modes with symmetric CH_2, asymmetric CH_2, and the asymmetric C-CH_3 stretching vibrations at 2856, 2922, and 2960 cm^{-1}, respectively. Further peaks at 1457 and 1378 cm^{-1} are attributed to the C-CH_2 vibrational scissoring and C-CH_3 symmetric bending modes. The presence of the vinyl (R-CH=CH_2) group in the spectrum of 1-dodecene is confirmed by the peak at 1640 cm^{-1}, corresponding to the

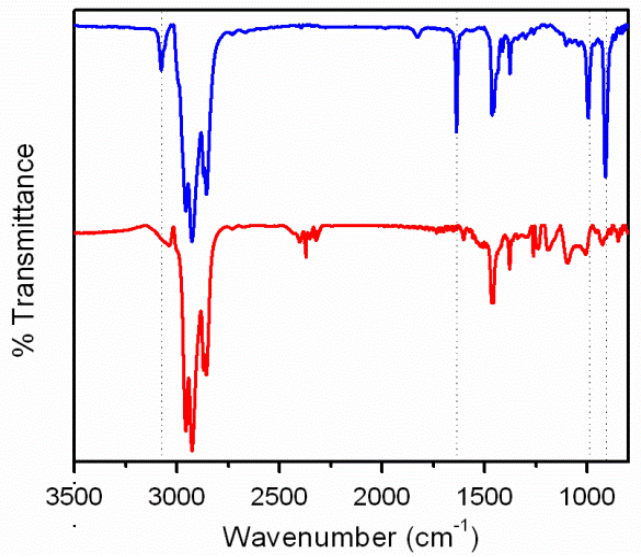

Figure 3.2: FTIR spectra of 1-dodecene (blue line) and the as-synthesised CQDs (red line). The dotted lines indicate the vinyl (R-CH=CH_2) stretching and bending vibrations.

C=C stretching mode. The peaks at 912 and 992 cm^{-1} are due to the =CH out-of-plane deformation and CH_2 out-of-plane wagging, while the small peak at 3081 cm^{-1} is due to the =CH stretch. The presence of strong CH_x peaks in the spectrum of the CQDs, combined with the absence of peaks due to the vinyl group, is consistent with successful binding of the ligand to the quantum dot surface to form dodecane-capped CQDs. The presence of some small peaks between 1300-1000 cm^{-1} is probably due to the presence of oxygenous functional groups such as C=O and C-O. However, the relatively low intensity of these peaks indicates that the CQDs are well passivated with minimal oxidation.

The optical properties of the CQDs were investigated using UV-visible and photoluminescence spectroscopy. Figure 3.3(a) shows the absorbance and photoluminescence spectra of the dodecane-capped CQDs in hexane. The absorption spectrum shows a peak centred at 264 nm with an onset of absorbance at 370 nm. This is in excellent agreement with reports of graphitic CQDs strongly absorbing in the UV region.[1] The photoluminescence spectra were obtained using excitation wavelengths ranging from 280 to 400 nm in 10 nm increments. The wavelength position of the PL maximum ranges from 325 nm for excitation at 280 nm to 450 nm for 400 nm excitation. This corresponds to an overall red shift in the PL peak position of 125 nm, as the excitation wavelength is increased by 120 nm; see Figure 3.3(b). This clear

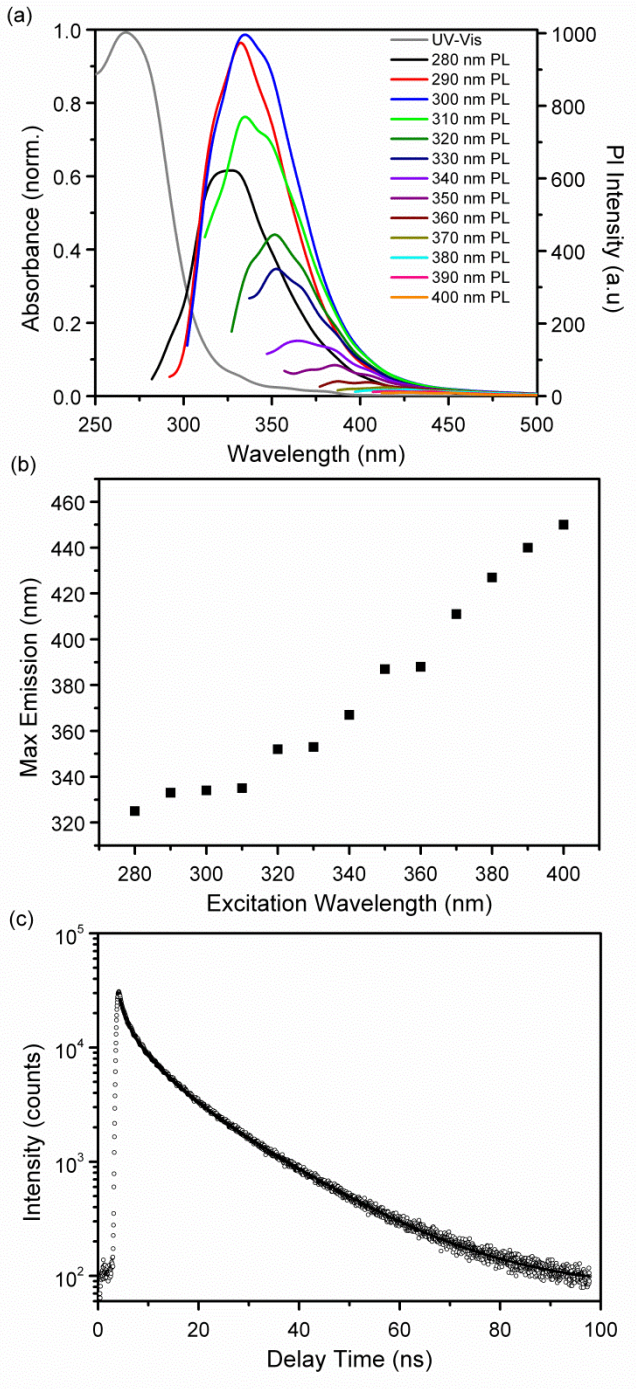

Figure 3.3: (a) UV-Vis absorbance and photoluminescence spectra of CQDs dispersed in hexane. (b) Wavelength position of the luminescence maximum as a function of excitation wavelength. (c) Photoluminescence decay of the alkyl capped CQDs.

dependency on excitation wavelength has also been widely observed for CQDs prepared using different methods of preparation and surface functionalities. [1-3] To date, the origin of luminescence for CQDs remains controversial mainly due to the wide variety of methods reported, surface oxidation and broad particle size distributions. [1-3]

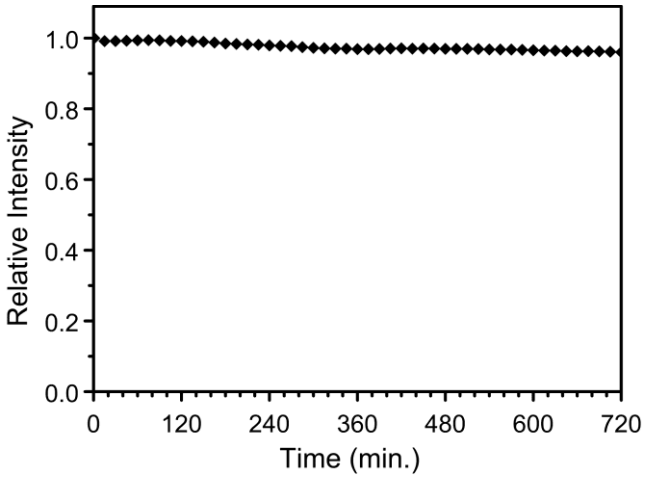

Figure 3.4: Long term photoluminescence stability of alkyl-capped CQDs recorded over 12 hours. Relative intensity was determined by integrating individual PL spectra, recorded at 1 min. intervals, between 300 and 450 nm. Relative intensities for individual spectra are plotted at 15 min. intervals for clarity.

The wavelength dependency has been mainly attributed to optical selection of differently sized nanocrystals (*i.e.* a quantum confinement effect), and/or emissive trap states on the surface but the exact mechanism still remains unresolved. Given the high degree of size monodispersity in the CQDs reported here, the most plausible explanation is that the blue luminescence originates from recombination of excitons at shallow surface trap states.[8, 28] The high degree of surface passivation may also contribute to the narrow PL spectra (FWHM: 60 nm) observed. Further insights into the optical behavior of the dodecane capped carbon quantum dots were obtained using time-resolved photoluminescence spectroscopy, see Figure 3.3 (c). The PL decay required a three-component exponential fit with time constants of approximately 1.1, 5.1, and 15.8 ns. This suggests that there exist multiple de-excitation processes in the CQDS. The CQDs also exhibit excellent long-term PL stability, decreasing by less than 4 % after continuous illumination for 12 hours, see Figure 3.4.

3.3.2 Synthesis of Amine Terminated Carbon Quantum Dots

In section 3.3.1, we reported the synthesis of size monodisperse carbon quantum dots using a room temperature microemulsion strategy. The surface of the CQDs are terminated with a covalently attached alkyl monolayer, rendering the resulting hydrophobic quantum dots dispersible in a wide range of non-polar solvents. However, for carbon quantum dots to be used effectively in many biological applications, it is essential that they are water-soluble and stable against aggregation and precipitation within a biological system, possess a high photoluminescence quantum yield in the visible region and exhibit excellent photostability under typical illumination conditions.

Here, we demonstrate a simple room temperature synthesis of highly monodisperse, amine terminated CQDs that form stable aqueous dispersions and exhibit strong visible emission. The CQDs are synthesized in reverse micelles *via* the reduction of carbon tetrachloride using a hydride reducing agent; see Experimental Section 3.2.1 and Table 3.1 (entry 2) for synthetic details. The hydrogen-terminated CQDs are functionalised using a platinum-catalysed concerted reaction to covalently attach allylamine ligands to the surface, chemically passivating the surface and rendering the CQDs dispersible in polar solvents, see Scheme 3.2.

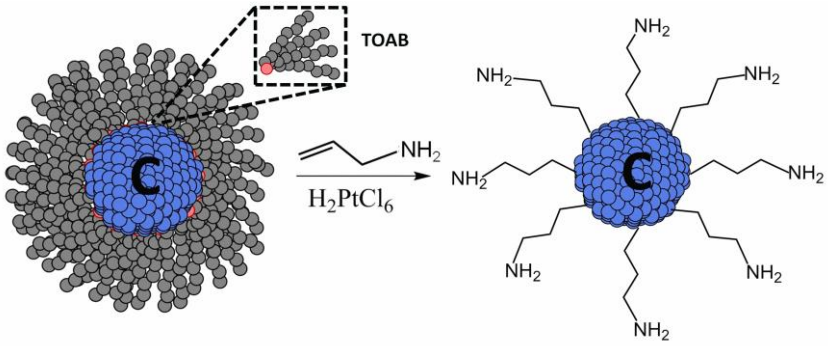

Scheme 3.2. Chemical passivation and functionalisation of the CQDs using a platinum-catalysed concerted reaction. CQDs are synthesized by reduction of CCl_4 within TOAB reverse micelles in toluene.

Figure 3.5(a) shows a TEM image of the as-synthesized CQDs. The CQDs are highly size and shape monodisperse. Figure 3.5(b) shows a high resolution TEM image of a single CQD, illustrating that the quantum dots are highly crystalline and form a single contiguous crystalline phase. The lattice fringes shown in Figure 3.5(b) correspond to a

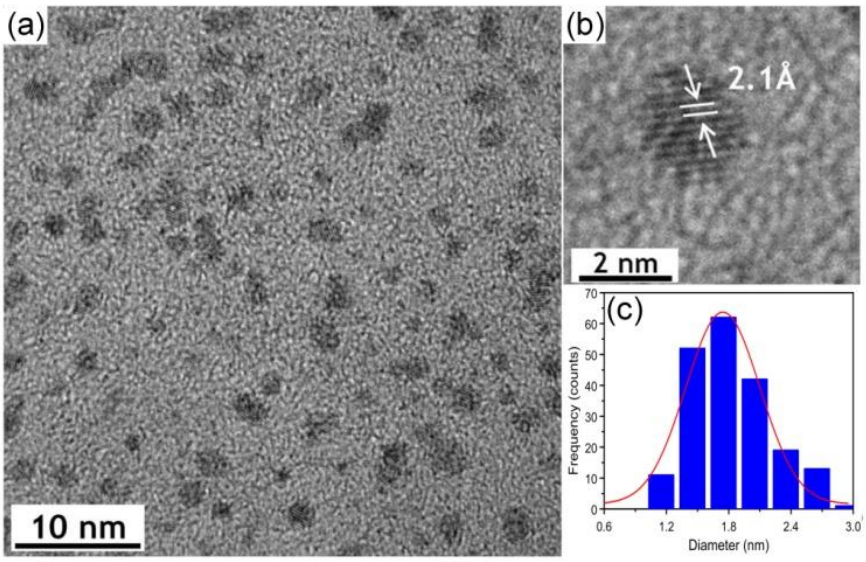

Figure 3.5: (a) Representative TEM image of the carbon quantum dots. (b) High–resolution TEM image of an individual CQD. (c) Size histogram of the CQDs with curve fitted to the data using a Gaussian model.

d spacing of 2.1 Å, matching the (100) spacing reported for graphitic carbon. Figure 3.5(c) shows a histogram of the CQD diameters, determined by analysis of TEM images of *ca.* 200 CQDs located at different locations on the grid. The mean diameter of the CQDs is 1.8 ± 0.3 nm, based on fitting the histogram to a Gaussian model. The surface chemistry of the quantum dots was characterized by infrared spectroscopy; Figure 3.6 shows the FTIR spectra of the allylamine ligand, together with allylamine-capped and uncapped CQDs. Spectra of allylamine-capped CQDs and the allylamine ligand show peaks from *ca.* 3700- 3500 cm^{-1}, assigned to the N-H stretching of the amine, while the peaks observed between 3000-2850 cm^{-1} are attributed to C-H stretching modes. The large feature centred near 1670 cm^{-1} for the allylamine-capped CQDs is consistent with amine N-H deformation modes, but also with stretching modes of carboxylate species caused by surface oxidation.

The peaks observed from 1500 to 1400 cm^{-1} are attributed to C-C bending modes. The absence of the characteristic $CH=CH_2$ peaks at 1640 and 3080 cm^{-1} for the capped CQDs, which is observed in the spectrum of neat allylamine, is consistent with successful binding of the allylamine ligand to the CQD surface. In contrast, the FTIR

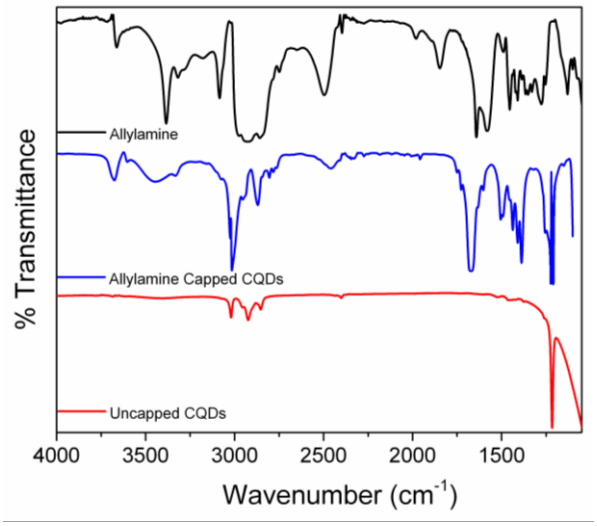

Figure 3.6: FTIR spectra of neat allylamine, allylamine-capped and uncapped CQDs.

spectrum of the uncapped CQDs shows no evidence of peaks that may be assigned to amine groups. The presence of peaks between 3000-2850 cm^{-1} are assigned to C-H stretching modes at the CQD surface, while the additional peaks below 1300 cm^{-1} are due to the presence of oxygenic species, indicating significant surface oxidation.

The optical properties of the CQDs were studied using UV-Vis absorption, photoluminescence (PL), photoluminescence excitation (PLE) and quantum yield measurements. The allylamine capped CQDs exhibit a strong absorption in the UV region, with a shoulder at *ca.* 320 nm and a tail extending into the visible range. The PL spectra were recorded using excitation wavelengths ranging from 300 to 400 nm in 20 nm increments. The CQDs exhibit a primarily blue luminescence, clearly dependent on the excitation wavelength used, with the wavelength position of the PL maximum red-shifting from 441 nm to 465 nm, as the excitation wavelength is increased from 300 nm to 400 nm. This is in good agreement with literature reports for CQDs dispersed in water.[8, 29]

Photoluminescence from CQDs still remains a widely debated topic despite the extensive research carried out in recent years. A number of different interpretations explaining the origin of PL in CQDs have been proposed.[1-3] Sun *et al.* suggested that the PL is due to the presence of energetic trap states near the CQD surface.[8] In contrast, Zhao *et al.* attributed the dependency on excitation wavelength to size differences rather than emissive trap states.[10] Although the exact mechanism still

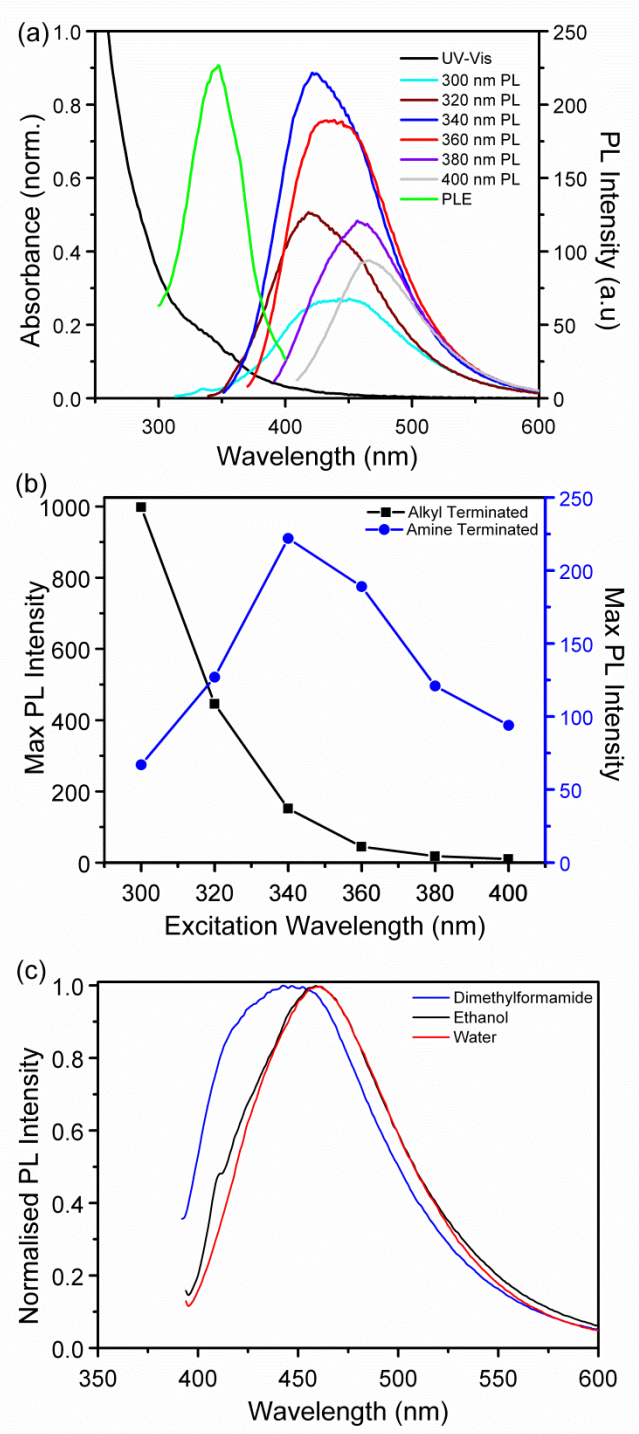

Figure 3.7: (a) UV-Vis absorption, PLE and PL spectra of an aqueous dispersion of the CQDs recorded at different excitation wavelengths. (b) Photoluminescence spectra of alkyl capped (black) and amine capped carbon quantum dots as a function of PL intensity. (c) Normalised photoluminescence spectra of the amine capped carbon quantum dots in dimethylformamide, ethanol and water.

remains unresolved, evidence exists that both mechanisms can contribute to both CQD emission colour and intensity. Given the high degree of size monodispersity in the CQDs reported here, the most plausible explanation is that the blue luminescence originates from recombination of photogenerated excitons at shallow surface trap states. PLE spectra recorded at the PL intensity maximum (423 nm, see Figure 3.7 (a)) show a narrow peak centred at *ca*. 347 nm, considerably above the band gap energy of the CQDs, suggesting radiationless transfer and recombination at states close to the CQD surface.

Interestingly, the relative luminescence intensity of the amine-terminated CQDs at different excitation wavelengths shows a maximum at 340 nm, in contrast to similarly sized CQDs with alkyl-terminated surfaces reported in Section 3.3.1 which exhibit monotonically decreasing luminescence intensity at increasing excitation wavelengths, see Figure 3.7(b) for a comparison of the excitation wavelength dependence of amine- and alkyl-terminated CQDs. This underlines the importance of the surface in determining the photophysical properties of CQDs, which has been widely observed for CQDs prepared using different preparation methods and surface functionalities.[1-3] Carbon quantum dots capped with either ligand show the same red-shift in the position of the PL maximum at increasing excitation wavelengths. The CQDs showed similar emission characteristics when dispersed in different polar solvent media, see Figure 3.7(c).

Photoluminescence quantum yield of the allylamine capped CQDs in water were determined using the comparative method by Williams *et al.*[26] Figure 3.8(a) shows the integrated PL intensity of the amine terminated CQDs compared to the 9,10-diphenylanthracene emission standard used; the quantum yield (QY) was determined to be *ca.* 25% at an excitation wavelength of 320 nm. This QY value is comparable to values obtained for CQDs reported in the literature. The CQDs also exhibit excellent long-term PL stability, decreasing by less than 3.5 % after continuous illumination for 12 hours; see Figure 3.8(b). Inset in Figure 3.8 (b) shows optical images of the CQD dispersion under white (left) and UV (365 nm, right) illumination. PL spectra of allylamine-terminated CQDs recorded in different pH environments (see Figure 3.8 (c)) showed fluctuations in the PL intensity, but no overall trend was observed.

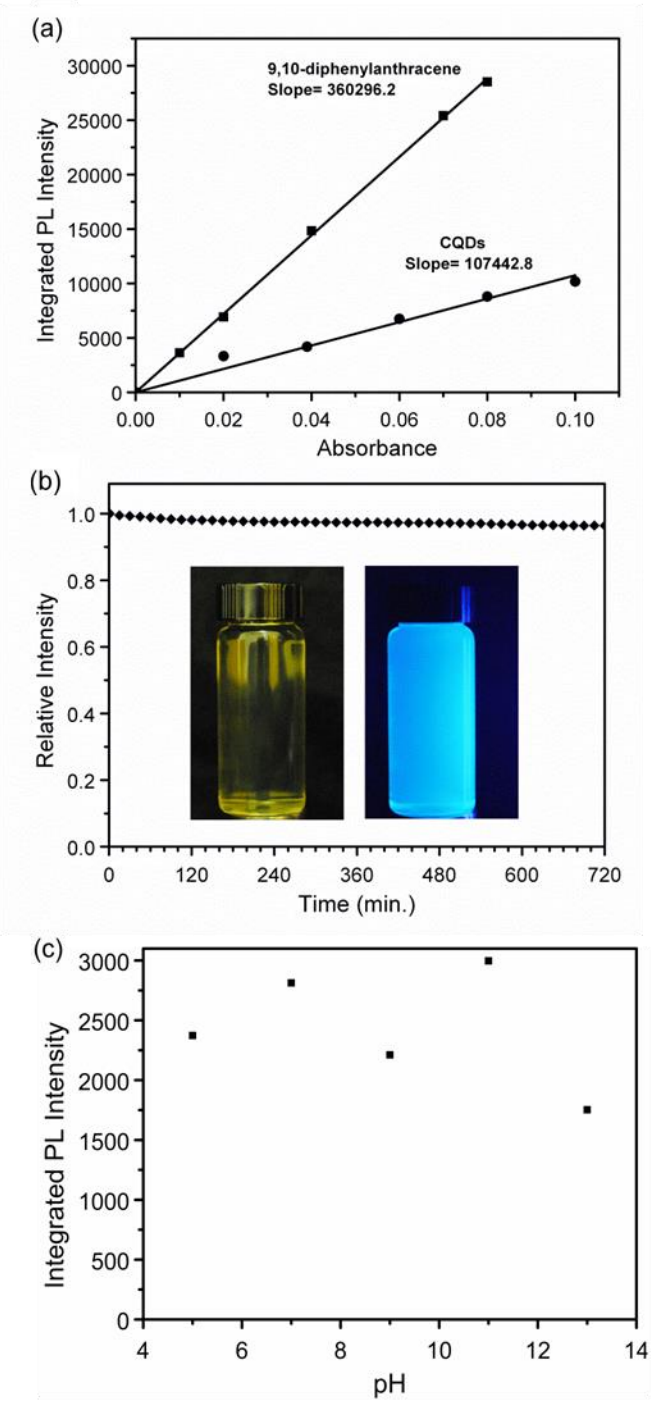

Figure 3.8: (a) Integrated PL intensity *versus* absorbance for an aqueous CQD dispersion and a solution of 9,10-diphenylanthracene in cyclohexane. (b) Long term PL stability recorded over 12 hours. Inset: Optical images of an aqueous CQD dispersion under white (left) and UV (365 nm; right) illumination. (c) Integrated PL intensity of allylamine-terminated CQDs recorded in different pH environments.

3.3.3 Size Control of Carbon Quantum Dots using Hydride Reducing Agents

In section 3.3.1 and 3.3.2, we reported the synthesis of size monodisperse CQDs which could be dispersed in a wide range of non-polar and polar solvents. Here we report a simple room temperature method for the size controlled synthesis of CQDs within inverse micelles having well defined core diameters ranging from 2 to 6 nm. The CQDs are chemically passivated and made water soluble using an allylamine ligand. Regulation of the CQDs size was achieved by utilizing hydride reducing agents of different strengths. Through controlling the size of the CQDs, their resulting photoluminescence properties could be tuned. Amine-terminated CQDs were synthesized by room temperature reduction of carbon tetrachloride under inert atmosphere conditions; see Experimental Section 3.2.1 and Table 3.1 (entries 3-6) for further details. In this study, hydride reducing agents of different reactivity's are compared. Lithium aluminium hydride ($LiAlH_4$), is the strongest reducing agent followed by lithium triethylborohydride (Superhydride®, $Li(C_2H_5)_3BH$), lithium tri-sec-butylborohydride (L-selectride®, $Li(CH(CH_3)CH_2CH_3)_3BH$) and lithium borohydride ($LiBH_4$).

Figure 3.9 (a-d) shows low magnification TEM images of CQDs prepared in the presence of the different hydride reducing agents. TEM imaging of CQDs synthesized in the presence of the strongest reducing agent $LiAlH_4$ (Figure 3.9 (a)) show that the CQDs are highly size and shape monodisperse, with no evidence of aggregation. Inset in Figure 3.9 (a) is a histogram of CQD diameters, determined by analysis of TEM images of 250 CQDs located at random locations on the grid. Fitting the histogram to a Gaussian model yielded a mean diameter of 1.8 nm, with a standard deviation of 0.3 nm, closely matching with the (002) interplanar spacing of graphite, emphasizing the highly size monodisperse nature of the CQD. Figure 3.9 (b) shows a low resolution TEM image of CQDs prepared using Superhydride as the reducing agent.

The CQDs were again found to be predominantly monodisperse and spherical with a mean diameter 2.1 ± 0.4 nm. Replacing superhydride with either L-selectride or $LiBH_4$ resulted in an increase in the mean CQD diameter to 4.5 ± 1.5 nm and 5.5 ± 1.4 nm respectively, see Figure 3.9(c) and 3.9(d). Whilst the mean CQD diameter increased using L-Selectride, the shape of the CQDs remained spherical, however the CQDs

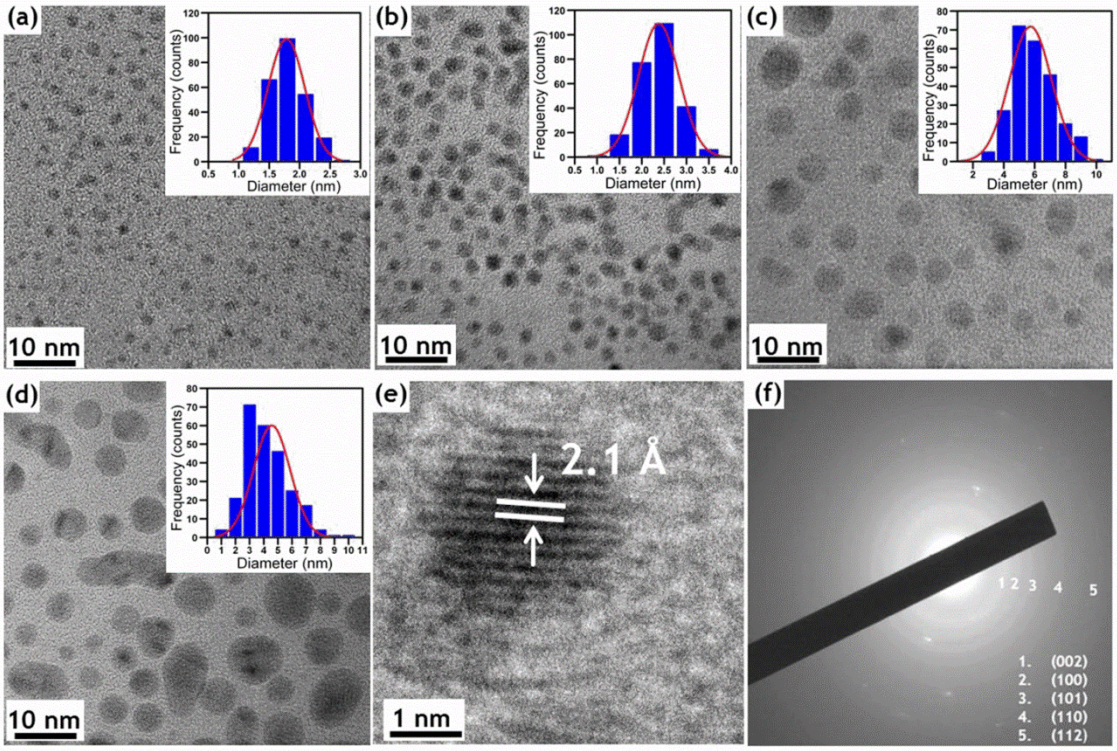

Figure 3.9: Representative TEM images of the CQDs synthesized in the presence of the following hydride reducing agents: a) $LiAlH_4$, b) $Li(C_2H_5)_3BH$, c) $Li(CH(CH_3)CH_2CH_3)_3BH$, and d) $LiBH_4$. Inset: Size histograms of the CQDs with curves fit to the data using a Gaussian model. e) HR-TEM and f) SAED pattern, of the Carbon quantum dots synthesized using $Li(C_2H_5)_3BH$ as the reducing agent.

prepared by the reduction using $LiBH_4$ were found to be larger in size, accompanied by a significant increase in size polydispersity and more irregular in shape. Lithium aluminium hydride is the most powerful reducing agent used in this work due to the weaker bond strength of Al-H compared to B-H. As a result, the reaction occurs rapidly and there is rapid consumption of the CCl_4 precursor during the initial nucleation phase, leaving little precursor material available for subsequent growth in solution. A similar trend is observed for the reduction by $Li(C_2H_5)_3BH$, leading to formation of smaller and more monodisperse quantum dots. However the CQDs formed by the weaker reducing agents L-Selectride or $LiBH_4$ resulted in larger sizes which may be due to less precursor consumption during the initial nucleation burst, and as a result, more unreacted CCl_4 is available for subsequent CQD growth. High-resolution TEM (HR-TEM) imaging was used in conjunction with selective area diffraction (SAED) to confirm the crystallinty and establish the crystal phase of the as-synthesized CQDs; see Figure 3.9(e-f). HR-

TEM imaging of CQDs produced using $Li(C_2H_5)_3BH$ (Figure 3.9(e)) as the reducing agent showed that the CQDs formed a single contiguous crystalline phase, without the presence of packing defects. The lattice fringes shown in Figure 3.9(e) correspond to a *d* spacing of 2.1 Å, matching the (100) spacing reported for the graphite unit cell. The selected area diffraction (SAED) in Figure 3.9(f), exhibited diffraction rings that could be indexed to the (002), (100), (101), (110) and (112) planes of graphite. No higher order graphitic reflections or reflections that could be indexed to the diamond phase were observed. The surface chemistry of the CQDs was investigated using high resolution XPS and FTIR spectroscopy, see Figure 3.10. The C1s spectrum in Figure 3.10(a) has a strong peak at 284.8 eV, assigned to C-C/C-H bonding, and two minor peaks at 286.2 and 287.8 eV are assigned to C-N and C-O bonding, respectively. The O1s spectrum in Figure 3.10 (b) has a single peak at 531.9 eV, assigned to the presence of $C–O_x$ groups at the CQD surface. The N1s spectrum presented in Figure 3.10 (c) is fitted with two components at 399.3 and 401.1 eV, assigned to C-N and N-H bonds, respectively. Figure 3.10 (d) shows the XPS full spectrum of the CQDs showing residual amounts of Cl and Br from the synthesis.

Figure 3.10(e) shows the FTIR spectra of the allylamine-terminated CQDs. The peaks between *ca.* 3700- 3500 cm^{-1} are assigned to the N-H stretching of the amine, while the peaks observed between 3000-2850 cm^{-1} are attributed to C-H stretching modes. The feature centred near 1670 cm^{-1} is consistent with amine N-H deformation modes, but also with stretching modes of carboxylate species caused by surface oxidation consistent with the XPS results. The peaks observed from 1500 to 1400 cm^{-1} are attributed to C-C bending modes. The absence of the characteristic $CH=CH_2$ peaks at 1640 and 3080 cm^{-1}, is consistent with successful binding of the allylamine ligand to the CQD surface, as previously reported. Additional peaks below 1300 cm^{-1} are probably due to the presence of adventitious oxygenic surface species again in agreement with XPS characterisation results.

Figure 3.11 (a) shows the UV-Vis absorption spectra of the CQDs in water prepared using the different hydride reducing agents. The spectrum of the smallest nanocrystals (1.8 nm), synthesized when $LiAlH_4$ was employed as reducing agent, showed a broad absorption band centred at *ca.* 270 nm with an onset of absorbance located at 480 nm. This is in excellent agreement with our previous reports for similarly sized amine-

terminated CQDs. Increasing the mean quantum dot diameter using Superhydride or L-selectride as the hydride reducing agent resulted in a distinct red-shift in the wavelength position of the absorption band to 304 and 306 nm, respectively. A further red shift in the absorption spectrum was observed when $LiBH_4$ was employed as the reducing agent, showing a strong peak centred at 315 nm, corresponding to a 45 nm shift compared to the smallest (1.8 nm) nanocrystals. Interestingly, the changes in CQD size do not significantly affect the onset of absorbance, located at *ca.* 480 nm (3.2 eV). Figure 3.11(b) shows normalized photoluminescence spectra (360 nm excitation) of

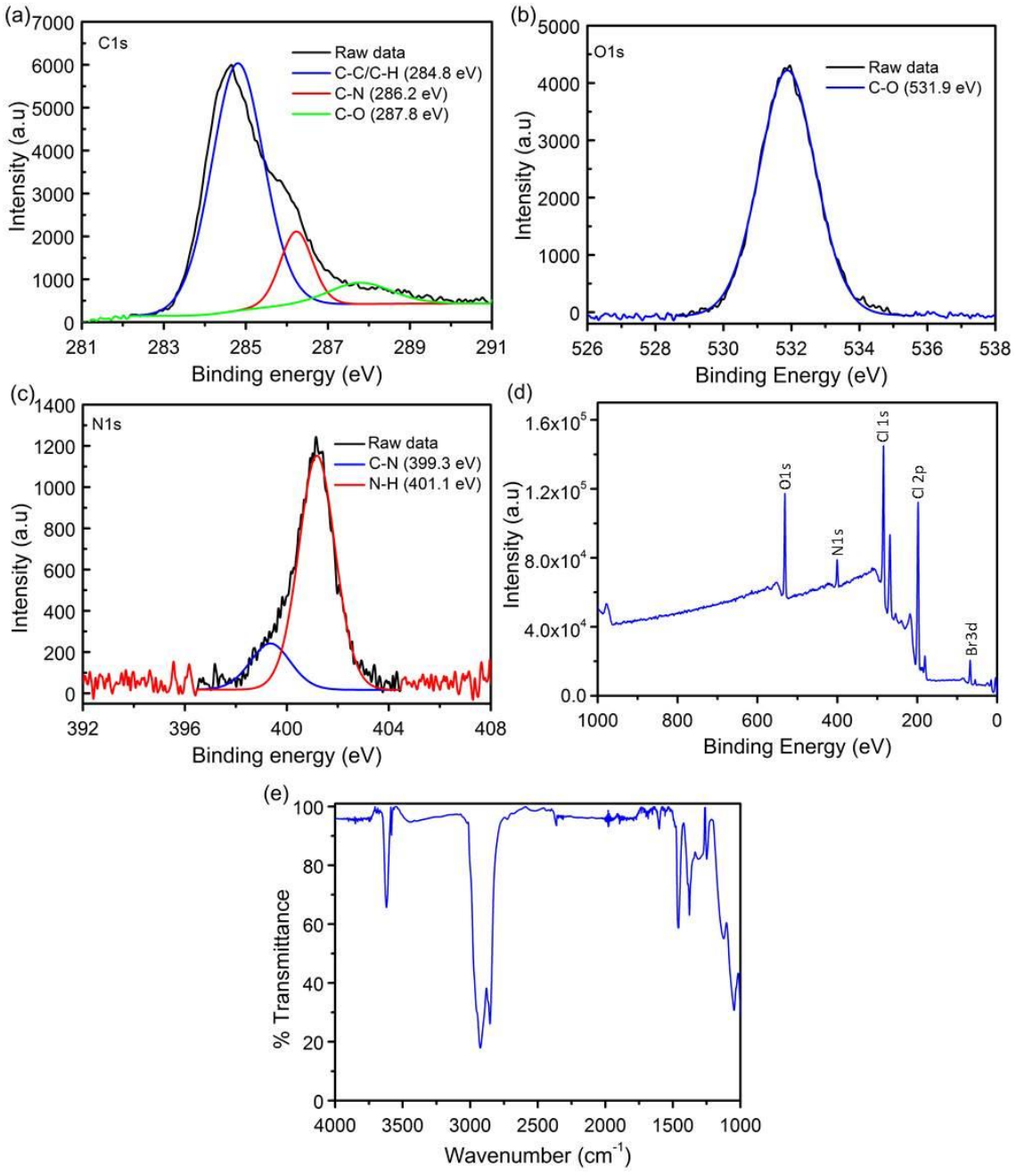

Figure 3.10: (a-d) XPS, (e) FTIR spectra of the amine terminated CQDs.

dilute dispersions of the CQDs in water, prepared with the same optical densities for comparison. Luminescence from the CQDs is observed over a narrow spectral range, with relatively little change as the diameter of the CQDs increases. For the smallest size CQDs the PL maximum emission was found to be at 450 nm, red-shifting with increasing quantum dot size, with the largest quantum dots showing a maximum emission at 462 nm. All the CQDs in this study showed a clear dependence on the excitation wavelength used, with the wavelength position of the PL maximum red-shifting as the excitation wavelength is increased from 300 nm to 440 nm, see Figure 3.12. This is in good agreement with literature reports for CQDs dispersed in water.[9, 18] As previously mentioned in Section 3.3.1, the exact origin of PL from CQDs remains a contentious topic: the wide variety of synthetic strategies reported, together with broad particle size distributions, different ligand passivation schemes and varying degrees of oxidation have all contributed to the lack of consensus. [1, 3] Interestingly, in all reports the PL spectra of CQDs exhibit a clear excitation wavelength dependence for

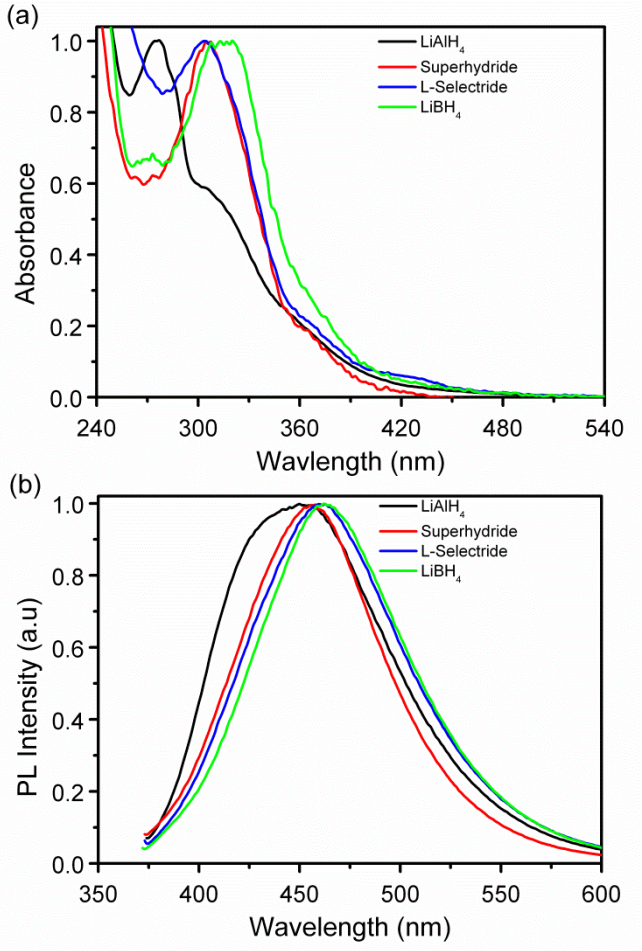

Figure 3.11: (a) Normalized UV-Vis absorption spectra (b) Photoluminescence spectra of the CQDs.

the emission maximum and intensity, which has been attributed to differently sized nanoparticles, different emissive trap states at the carbon dot surface, or other unresolved mechanisms.[1] Although the photophysical properties of CQDs have been demonstrated to depend on nanocrystal size, since graphitic carbon is not a semiconductor,[2] it is problematic to explain this using the bandgap exciton recombination description used for semiconductor QDs.

Sun *et al.* attributed the PL from CQDs to the presence of surface energy traps that become emissive upon surface passivation.[8] They noted that this requirement was shared by CQDs and Si NCs, but that a large surface-to-volume ratio is required in order for the nanocrystal to exhibit strong photoluminescence upon surface passivation. In Section 3.3.1 and 3.3.2, we have demonstrated that similar sized CQDs exhibit

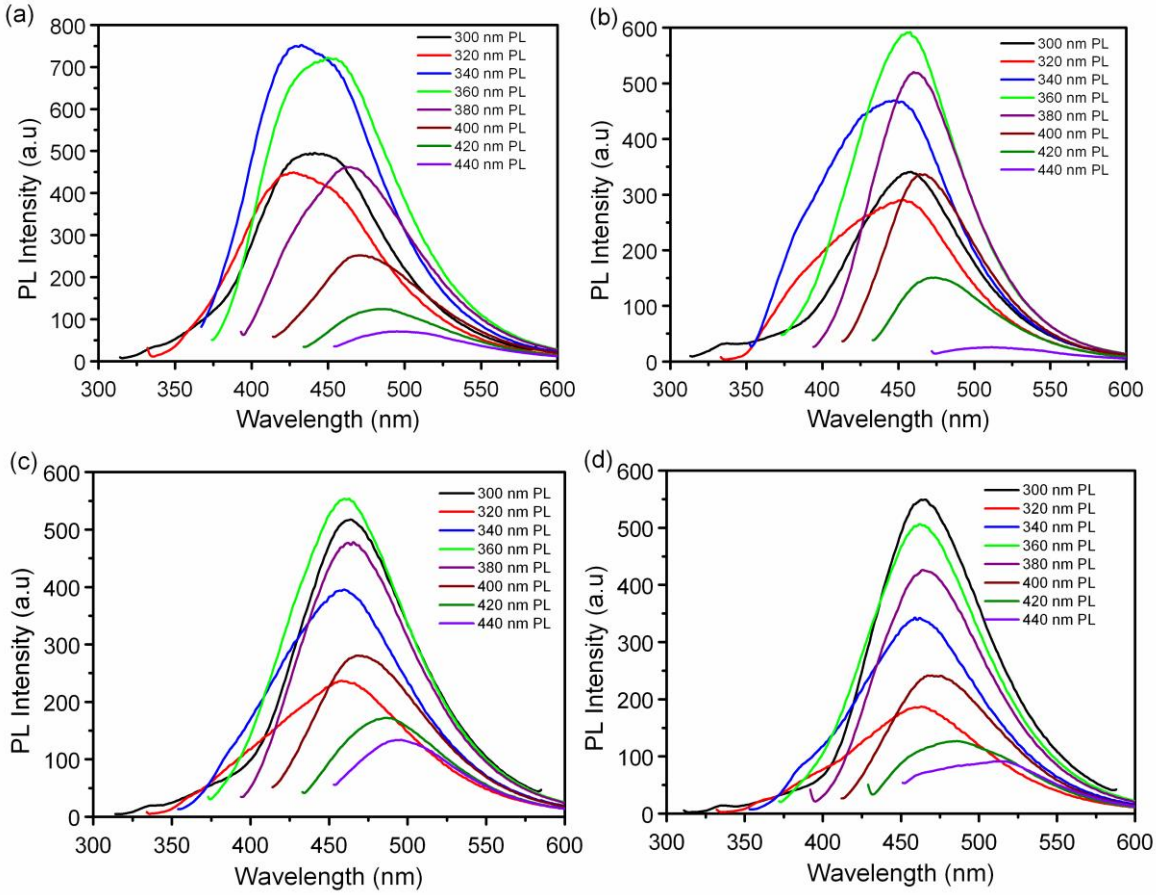

Figure 3.12: Photoluminescence spectra of the amine terminated carbon quantum dots synthesised using the different hydride reducing agents a) lithium aluminium hydride, b) lithium triethylborohydride, c) lithium tri-sec-butylborohydride, and d) lithium borohydride in water.

distinctly different photoluminescence properties when capped with ligands of different polarity, underlining the importance of the surface in determining their photophysical properties. Due to the high degree of monodispersity within those samples, we concluded the most plausible explanation was that the excitation wavelength dependence observed originated from recombination of photogenerated excitons at different surface trap states.

Since the surface of the CQDs were capped using the same ligand functionalisation method, the variations in the PL spectra shown in Figure 3.11(b) should not be due to surface effects, although the increased polydispersity of the larger CQDs would be expected to have some contribution. The similarly of the PL spectra for different sized CQDs observed supports the interpretation that the PL mechanism is dominated by surface trap states. The relative photoluminescence of the CQDs was shown to increase with decreasing diameter (and thus, increasing surface-to-volume ratio), in agreement with reports by Sun *et al*.[8]

Figure 3.13(a) shows the integrated PL intensity of dilute dispersions of 1.8 nm diameter CQDs in water compared to the emission standard used, 9,10-diphenylanthracene in cyclohexane. Linear regression analysis was employed to determine the relative PL intensities of the sample and reference solutions over the range of concentrations; see Figure 3.14 for additional plots and analyses of the CQDs synthesised using the other reducing agents. When $LiAlH_4$ was used as the reducing agent, the quantum yield was found to be *ca.* 27% at an excitation wavelength of 320nm, comparable to values obtained for CQDs reported in the literature. As discussed above, the quantum yields generally decrease with increasing quantum dot diameter, with the largest size quantum dots exhibiting a quantum yield of 19.3%, see Table 3.2.

Further insight into the photophysical behaviour of the CQDs was obtained using time-resolved photoluminescence spectroscopy. Photoluminescence transients of the CQDs were acquired using time-correlated single photon counting methods (λ_{ex} = 402 nm); see Figure 3.13(b) and Figure 3.14. Measured transients were well fitted ($\chi^2 < 1.3$) to the sum of three weighted exponentials; the fitted time constants and relative amplitudes are summarised in Table 3.2. From Table 3.2, it can be seen that the dominant lifetime

component is between 4.5-6.7 ns, while other contributions with time constants of 1-3 ns and 12-16 ns are also present in the PL transients.

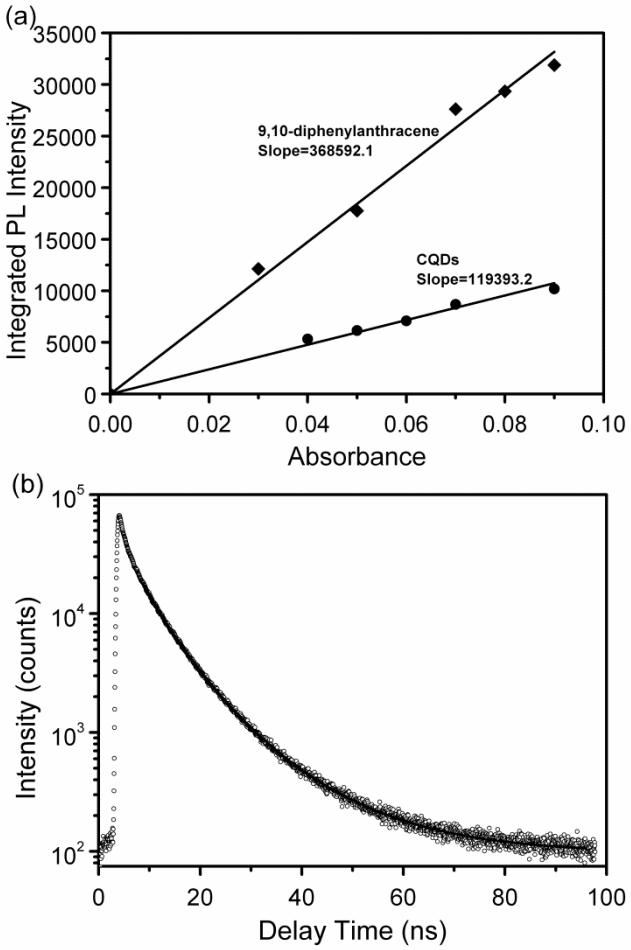

Figure 3.13: Integrated PL intensity *versus* absorbance for an aqueous CQD dispersion and a solution of 9,10-diphenylanthracene in cyclohexane. (b) Time resolved PL spectra of the allylamine capped CQDs.

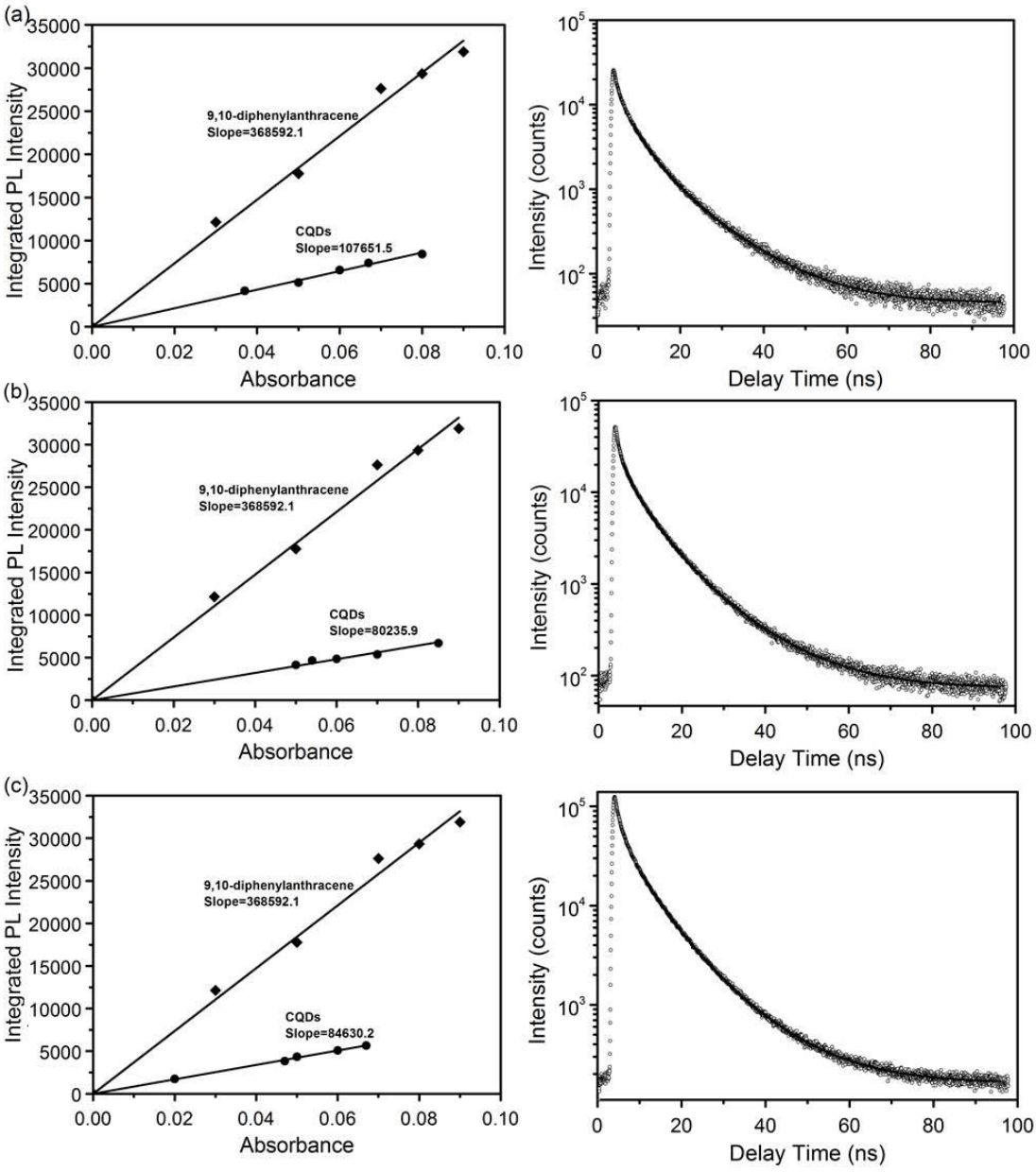

Figure 3.14: (a) Integrated PL intensity *versus* absorbance, and corresponding time resolved PL spectra, of dilute aqueous dispersions of CQDs synthesized using a) Superhydride, b) L-Selectride, and c) lithium borohydride.

Table 3.2. Table of fitted amplitudes and time constants for three-component exponential fitting to PL decays recorded for CQDs.

Reducing agent	**Quantum yield**	**A1 (%)**	**τ1 (ns)**	**A2 (%)**	**τ2 (ns)**	**A3 (%)**	**τ3 (ns)**	χ^2
$LiAlH_4$	27.1	26	3.1 ± 0.1	63	6.7 ± 0.1	11	15.8 ± 0.2	1.24
Superhydride	24.6	6	0.5 ± 0.4	61	4.5 ± 0.1	33	11.8 ± 0.1	1.10
L-Selectride	18.4	26	1.6 ± 0.1	59	5.6 ± 0.1	15	13.0 ± 0.1	1.20
$LiBH_4$	19.4	15	2.6 ± 0.2	63	6.3 ± 0.1	22	13.0 ± 0.1	1.26

3.4 Conclusions

In summary size monodisperse carbon quantum dots have been synthesized using methods adapted from those reported for Si NCs, demonstrating close control of internal structure and surface chemistry. The surfaces of the CQDs are chemically functionalised using a platinum catalysed concerted reaction to covalently attach amine or alkyl ligands, rendering the CQDs dispersible in wide range of polar or non-polar solvents. It was shown that the size of the CQDs can be tuned from by varying the strength of the hydride reducing agent. HR-TEM imaging confirmed that the CQDs are highly crystalline, while lattice fringes recorded by SAED could be indexed to the crystal structure of graphitic carbon. FTIR and XPS spectroscopy confirmed that the CQDs were well passivated, with some evidence of surface oxidation. UV-Vis and PL spectroscopy show absorption in the UV spectral range, with an excitation wavelength dependent blue emission, similar to that previously observed for Si NCs. Time resolved photoluminescence measurements showed nanosecond lifetimes for all CQDs, while determination of the photoluminescence quantum yield (Φ) of showed a maximum of 27% determined for ~1.8 nm CQDs, comparable with the current state of the art for room temperature synthesised nanocrystals. These water-soluble CQDs are highly photostable and resistant to aggregation, allowing their application in areas ranging from biological imaging to fluorescence sensing.

3.5 References:

1. Li, H.; Kang, Z.; Liu, Y.; Lee, S. T., Carbon nanodots: synthesis, properties and applications. *Journal of Materials Chemistry* **2012**, *22*, 24230-24253.

2. Esteves da Silva, J. C. G.; Gonçalves, H. M. R., Analytical and bioanalytical applications of carbon dots. *Trends in Analytical Chemistry* **2011**, *30*, 1327-1336.

3. Baker, S. N.; Baker, G. A., Luminescent Carbon Nanodots: Emergent Nanolights. *Angewandte Chemie, International Edition* **2010**, *49*, 6726-6744.

4. Kwon, W.; Do, S.; Won, D. C.; Rhee, S. W., Carbon quantum dot-based field-effect transistors and their ligand length-dependent carrier mobility. *ACS Applied Materials & Interfaces* **2013**, *5*, 822-827.

5. Wang, F.; Chen, Y.H.; Liu, C.Y.; Ma, D.G., White light-emitting devices based on carbon dots electroluminescence. *Chemical Communications* **2011**, *47*, 3502-3504.

6. Xu, X.; Ray, R.; Gu, Y.; Ploehn, H. J.; Gearheart, L.; Raker, K.; Scrivens, W. A., Electrophoretic analysis and purification of fluorescent single-walled carbon nanotube fragments. *Journal of the American Chemical Society* **2004**, *126*, 12736-12737.

7. Goncalves, H.; Esteves da Silva, J. C. G., Fluorescent Carbon Dots Capped with PEG(200) and Mercaptosuccinic Acid. *Journal of Fluorescence* **2010**, *20*, 1023-1028.

8. Sun, Y. P.; Zhou, B.; Lin, Y.; Wang, W.; Fernando, K. A. S.; Pathak, P.; Meziani, M. J.; Harruff, B. A.; Wang, X.; Wang, H.; Luo, P. G.; Yang, H.; Kose, M. E.; Chen, B.; Veca, L. M.; Xie, S. Y., Quantum-sized carbon dots for bright and colorful photoluminescence. *Journal of the American Chemical Society* **2006**, *128*, 7756-7757.

9. Jiang, H.; Chen, F.; Lagally, M. G.; Denes, F. S., New strategy for synthesis and functionalization of carbon nanoparticles. *Langmuir* **2009**, *26*, 1991-1995.

10. Zhao, Q. L.; Zhang, Z. L.; Huang, B. H.; Peng, J.; Zhang, M.; Pang, D. W., Facile preparation of low cytotoxicity fluorescent carbon nanocrystals by electrooxidation of graphite. *Chemical Communications* **2008**, 5116-5118.

11. Zheng, L.; Chi, Y.; Dong, Y.; Lin, J.; Wang, B., Electrochemiluminescence of water-soluble carbon nanocrystals released electrochemically from graphite. *Journal of the American Chemical Society* **2009**, *131*, 4564-4565.

12. Zhou, J.; Booker, C.; Li, R.; Zhou, X.; Sham, T. K.; Sun, X.; Ding, Z., An electrochemical avenue to blue luminescent nanocrystals from multiwalled

carbon nanotubes (MWCNTs). *Journal of the American Chemical Society* **2007**, *129*, 744-745.

13. Liu, H.; Ye, T.; Mao, C., Fluorescent carbon nanoparticles derived from candle soot. *Angewandte Chemie* **2007**, *119*, 6593-6595.

14. Wang, X.; Cao, L.; Lu, F.; Meziani, M. J.; Li, H.; Qi, G.; Zhou, B.; Harruff, B. A.; Kermarrec, F.; Sun, Y. P., Photoinduced electron transfers with carbon dots. *Chemical Communications* **2009**, 3774-3776.

15. Pan, D.; Zhang, J.; Li, Z.; Wu, C.; Yan, X.; Wu, M., Observation of pH-, solvent-, spin-, and excitation-dependent blue photoluminescence from carbon nanoparticles. *Chemical Communications* **2010**, *46*, 3681-3683.

16. Liu, R.; Wu, D.; Liu, S.; Koynov, K.; Knoll, W.; Li, Q., An aqueous route to multicolor photoluminescent carbon dots using silica spheres as carriers. *Angewandte Chemie* **2009**, *121*, 4668-4671.

17. Zong, J.; Zhu, Y.; Yang, X.; Shen, J.; Li, C., Synthesis of photoluminescent carbogenic dots using mesoporous silica spheres as nanoreactors. *Chemical Communications* **2011**, *47*, 764-766.

18. Bourlinos, A. B.; Stassinopoulos, A.; Anglos, D.; Zboril, R.; Georgakilas, V.; Giannelis, E. P., Photoluminescent carbogenic dots. *Chemistry of Materials* **2008**, *20*, 4539-4541.

19. Zhu, H.; Wang, X.; Li, Y.; Wang, Z.; Yang, F.; Yang, X., Microwave synthesis of fluorescent carbon nanoparticles with electrochemiluminescence properties. *Chemical Communications* **2009**, 5118-5120.

20. Wang, X.; Qu, K.; Xu, B.; Ren, J.; Qu, X., Microwave assisted one-step green synthesis of cell-permeable multicolor photoluminescent carbon dots without surface passivation reagents. *Journal of Materials Chemistry* **2011**, *21*, 2445-2450.

21. Li, H.; He, X.; Kang, Z.; Huang, H.; Liu, Y.; Liu, J.; Lian, S.; Tsang, C. H. A.; Yang, X.; Lee, S.T., Water-Soluble fluorescent carbon quantum dots and photocatalyst design. *Angewandte Chemie International Edition* **2010**, *49*, 4430-4434.

22. Bhunia, S. K.; Saha, A.; Maity, A. R.; Ray, S. C.; Jana, N. R., Carbon nanoparticle-based fluorescent bioimaging probes. *Scientific Reports.* **2013**, *3*. 1473.

23. Kwon, W.; Rhee, S. W., Facile synthesis of graphitic carbon quantum dots with size tunability and uniformity using reverse micelles. *Chemical Communications* **2012**, *48*, 5256-5258.

24. Kwon, W.; Lee, G.; Do, S.; Joo, T.; Rhee, S. W., Size-controlled soft-template synthesis of carbon nanodots toward versatile photoactive materials. *Small* **2014**, *10*, 506-513.
25. Gao, M. X.; Liu, C. F.; Wu, Z. L.; Zeng, Q. L.; Yang, X. X.; Wu, W. B.; Li, Y. F.; Huang, C. Z., A surfactant-assisted redox hydrothermal route to prepare highly photoluminescent carbon quantum dots with aggregation-induced emission enhancement properties. *Chemical Communications* **2013**, *49*, 8015-8017.

26. Williams, A. T. R.; Winfield, S. A.; Miller, J. N., Relative fluorescence quantum yields using a computer-controlled luminescence spectrometer. *Analyst* **1983**, *108*, 1067-1071.

27. Hamai, S.; Hirayama, F., Actinometric determination of absolute fluorescence quantum yields. *The Journal of Physical Chemistry* **1983**, *87*, 83-89.

28. Linehan, K.; Doyle, H., Size controlled synthesis of silicon nanocrystals using cationic surfactant templates. *Small* **2014**, *10*, 584-590.

29. Liu, R.; Wu, D.; Liu, S.; Koynov, K.; Knoll, W.; Li, Q., An aqueous route to multicolor photoluminescent carbon dots using silica spheres as carriers. *Angewandte Chemie, International Edition* **2009**, *121*, 4668-4671.

Appendices

A.1 Abbreviations and Acronyms

APTMS	3-aminopropyltrimethoxysilane
AESAPTMS	3-(2-Aminoethylamino)propyltrimethoxysilane
AFM	Atomic force microscopy
AAS	Atomic absorption spectroscopy
ASV	Anodic stripping Voltammetry
Ag/AgCl	Silver/Silver chloride
$AlCl_3$	Aluminum chloride
APD	Avalanche photodiode
BSA	Bovine serum albumin
CTAB	Cetyltrimethylammonium bromide
C12E5	Pentaethylene glycol monododecyl ether
CVD	Chemical Vapor Deposition
CCD	Charge Coupled Device
CQD	Carbon quantum dot
CdS	Cadmium sulfide
CCl_4	Chloroform
CaF_2	Calcium fluoride
cm	Centimetre
DDAB	Dodecyltrimethylammonium bromide
DTAB	Dodecyltrimethylammonium bromide
DMF	Dimethylforamide
DSC	Differential scanning calorimetry
d	Diameter
DI	Deionized water
ETOH	Ethanol
EDTA	Ethylene diamine tetraacetic acid
EDA	1,2-ethlenediamine
EDX	Energy dispersive x-ray diffraction
EA	Ethyamine
ET	Energy transfer
E_g	Energy gap

eV	Electron Volt
FTIR	Fourier Transform infrared spectroscopy
FWHM	Full width maximum
F-Q	Concentration of the complex
FC	Fluorescence Color
F_0	Fluorescence intensity in the absence of quencher
F	Fluorescence intensity in the presence of quencher
GQDs	Graphene Quantum Dots
g	gram
H_2PtCl_6	Hexachloroplatinic acid
H_20_2	Hydrogen peroxide
HNO_3	Nitric Acid
HCl	Hydrochloric acid
H_2S0_4	Sulphuric acid
HR-TEM	High resolution transmission electron microscopy
H_20	Water
h	Hour
H_2	Hydrogen
HF	Hydrofluoric acid
ICP-ES	Inductively coupled plasma emission spectrometry
ICP-MS	Inductively coupled plasma mass spectrometry
IR	Infrared red
iL	Ionic liquid
Kpa	Kilopascal
K	Kelvin
K_q	Biomolecular quenching constant
K_D	Stern-Volmer quenching constant
KeV	Kilo electron Volt
k_f	Fluorescence
k_t	Intersystem crossing
k_{eaq}^-	Photoionization
kV	Kilovolt
k_i	Intramolecular quenching

$LiAlH_4$	Lithium Aluminum Hydride
Superhydride	Lithium triethylborohydride
$LiBH_4$	Lithium borohydride
L-selectride	Lithium trisecbuyhylborohydride
LAB_6	Lanthanum hexaboride
Ltd	Limited
Mg/Ml	Milligram per milliliter
Mgsi	Magnesium Silicide
ML	Milliliter
Min	Minute
Mn	Maganese
mM	Millimolar
Mg/h	Milligram per hour
mA cm^{-2}	Milliampere per square centimeter
mmol	Millimolar
M	Molar
mm	Millimeter
mg	Milligram
mA	Milliamp
MHz	Megahertz
$Na_2S_20_8$	Sodium persulfate
$NaNH_2$	Sodium Amide
NaOH	Sodium hydroxide
NaCl	Sodium chloride
NaH_2P0_4	Monosodium phosphate
NIR	Near infrared
nm	Nanometer
NPs	Nanoparticles
NCs	Nanocrystals
ns	Nanosecond
nM	Nanomolar
OPPF6	N-octylpyridinumhexafluorophosphate
PEG200	Polyethylene glycol 200
PVDF	Polyvinylidene difluoride

PL	Photoluminescence
PLE	Photoluminescence excitation spectra
P-type	Positive Holes (semiconductor)
PMS	Particle Mass spectrometer
Ps	Picosecond
pH	Potential of hydrogen
QDs	Quantum Dots
QY	Quantum yield
Ref.	Reference
$SiCl_4$	Silicon tetrachloride
$SiBr_4$	Silicon tetrabromide
Si-H	Silicon-hydrogen
Si-O	Silicon oxide
SiO_2	Silicon dioxide
STM	Scanning tunneling microscopy
SAED	Selective Area Electron diffraction
SPR	Surface Plasmon resonance
TEM	Transmission electron microscopy
TEOS	Tetraethoxysilane
TXRF	Total reflection X-Ray fluorimetry
Tris	2-amino-2-hydroxymethyl-propane
TPA	Tripropylamine
TTDDA	4,7,10-trioxa-1,13-tridecanediamine
THF	Tetrahydrofuran
TOAB	Tetraoctylammonium bromide
TBAB	Tetrabutyl ammonium bromide
TDAB	Tetradodecylammonium bromide
TCSPC	Time-Correlated Single Photon Counting
TGA	Thermogravametic analysis
T	Temperature
UV	Ultra violet
UV-VIS	Ultraviolet-Visible
wt%	Weight percent
XPS	X-ray photoelectron spectroscopy

XRD	X-ray diffraction
%	Percent
°C	Degrees Celsius
~	Approximately
µs	Microsecond
µL	Microliter
µM	Micromolar
µm	Microns
/	No information
Δ	Delta
σ	Sigma
Å	Angstrom
τ_0	Lifetime of the fluorophore in the absence of quencher
τ^{-1}	Fluorescence lifetime
Q	Concentration of quencher
Ø	Diameter
χ^2	Chi
Φ	Quantum yield
λ	Wavelength

A.2 Publications

1. **K. Linehan**, H. Doyle, Size Controlled Synthesis of Carbon Quantum Dots using Hydride Reducing Agents. *Journal of Materials Chemistry C* 2014, 2, 6025-6031.

2. **K. Linehan**, H. Doyle, Solution Reduction Synthesis of Amine Terminated Carbon Quantum Dots. *RSC Advances* 2014, 4, 12094-12097.

3. **K. Linehan**, H. Doyle, Efficient One Pot Synthesis of Highly Monodisperse Alkyl Functionalized CQDs Dots. *RSC Advances* 2014, 4, 18 – 21.

4. **K. Linehan**, H. Doyle, Size Control Synthesis of Silicon Nanocrystals using Cationic Surfactants. *Small* 2014, 10, 564-59.

5. **K. Linehan**, H. Doyle Silicon quantum dots as fluorescence sensing probes for detection of heavy metal ions. Nanoscale 2014 (In preparation).

6. **K. Linehan**, H. Doyle Fruit Juice as a natural source of Carbon Quantum Dots Angewandte Chemie 2014 (In preparation).

7. **K. Linehan**, H. Doyle, Size Control Synthesis of Silicon Nanocrystals using Cationic Surfactants. *Material Research Society Symposium Proceedings* 2013, 1546, mrss13-1546-11506-1548.

8. **K. Linehan,** D. Carolan, D. O'Sé H. Doyle, Synthesis and Compositional Control of Size Monodisperse Si_xGe_{1-x} Nanocrystals for Optoelectronic Applications. *Material Research Society Symposium Proceedings* 2013, 1551, mrss13-1551-r02-03.

9. S. Padmanabhan, **K. Linehan**, S. O'Brien, S. Kassim, H. Doyle, I. M. Povey, M. E. Pemble, A bottom-up fabrication method for the production of visible light active photonic crystals. *Journal of Materials Chemistry C* 2014, 2, 1675-1682.

10. P. Faucherand; C. Morin; K. Jarolimek; R. A. C. M. M. Van Swaaij; M. Zeman; S. Richards; A. Kingsley; H. Doyle; **K. Linehan**; S. O'brien; I. M. Povey; M. E. Pemble; L. Xie; K. Leifer; K. Makasheva; B. Despax, F. Heinz, A. Witzky, M. Bellettato, M. Allegrezza, D. Hiller, A. Hartel, S. Gutsch, S. Hernandez, R. Guerra, S. Ossicini, B. Garrido, S. Janz, M. Zacharias, Advanced Concepts for Silicon based Photovolatics. *Physica Status Solidi (a)* 2013, 210, 625-629.

11. S. Perraud; E. Quesnel; S. Parola; J. Barbé; V. Muffato; P. Faucherand; C. Morin; K. Jarolimek; R. A. C. M. M. Van Swaaij; M. Zeman; S. Richards; A. Kingsley; H. Doyle; **K. Linehan**; S. O'brien; I. M. Povey; M. E. Pemble; L. Xie; K. Leifer; K. Makasheva; B. Despax, Silicon nanocrystals: Novel Synthesis Routes for Photovoltaic Applications. *Physica Status Solidi (a)* 2013, 210, 649.

12. S. O'Brien, **K. Linehan**, H. Doyle, A. Kingsley, C. Ashfield, B. Frank, L. Xie, K. Liefer, P. Thony, S. Perraud, M. E. Pemble, I. M. Povey, Indium tin oxide–silicon nanocrystal nanocomposite grown by aerosol assisted chemical vapour deposition, *Journal of Sol-Gel Science and Technology* 2015, DOI 10.1007/s10971-015-3618-3

A.3 Presentations

1. M. E Pemble, M. Bardosova, J. A.M. Delezuk, H.Doyle, **K. Linehan**, S. Kassim, J. McGrath, S. O'Brien, O. N. de Oliveira Jr., S. Padmanabhan, A.Pavinatto, I. Povey, C.Ryan and M. Schmidt, Exploiting Structural Colour: Colloidal Photonic Crystals as Novel Chromogenic Media. 1st International Caparica Conference on Chromogenic and Emissive Materials Lisbon , Portugal, (*Oral Presentation*), September 2014.

2. D. Lordan, A. Miranda, **K. Linehan,** E. Noonan, E. Puicervert, R. Russell, A. Pescaglini, M. Manning, M. Burke, A. Quinn, Molecular Functionalization of Exfoliated Graphene and Transferred CVD graphene, MRS Spring Meeting, San Francisco, California (*Poster*), April 2014.

3. D. Carolan, **K. Linehan,** H. Doyle, Synthesis and Compositional Control of Elemental and Alloy Group IV Nanocrystals for Optoelectronic Applications Tyndall emerging devices and technology day Tyndall National Institute, Cork (*Poster*), September 2013.

4. **K. Linehan,** H. Doyle, Synthesis and Characterisation of group IV nanomaterials for optoelectronic applications. Postgraduate Research Day, University College Cork (*Oral*), August 2013.

5. H. Doyle, S. O'Brien, I. M Povey, S. Rushworth, **K. Linehan**, A. Kingsley, L. Xie, K. Liefer, S. Perraud, M. E Pemble, Indium Tin Oxide Nanocomposites Incorporating Silicon Nanocrystals Grown by Aerosol Assisted CVD" 13th European Conference on Organised Films, Cork, Ireland, (*Oral Presentation*), July 2013.

6. **K. Linehan,** H. Doyle, Synthesis and Characterization of Silicon Nanocrystals for Optoelectronic Applications, Tyndall Internal Conference, Tyndall National Institute (*Poster*), May 2013.

7. S. O'Brien, **K. Linehan**, H. Doyle, M. Pemble, I. Povey, Indium Tin Oxide Grown by Aerosol Assisted CVD and Incorporation of Ligand Stabilized Silicon Nanocrystals, Tyndall Internal Conference, Tyndall National Institute (*Poster*), May 2013.

8. **K. Linehan,** D. Carolan, D**.** O'Sé H. Doyle, Synthesis and Compositional Control of Size Monodisperse Si_xGe_{1-x} Nanocrystals for Optoelectronic Applications, MRS Spring Meeting, San Francisco, California (*Oral Presentation*), April 2013.

9. **K. Linehan,** H. Doyle, Size Controlled Synthesis of Silicon Nanocrystals using Cationic Surfactant Templates, MRS Spring Meeting, San Francisco, California (*Poster*), April 2013.

10. **K. Linehan,** H. Doyle, Size Control Synthesis of Silicon Nanocrystals using Cationic Surfactants, Postgraduate Research Day, University College Cork (*Poster*), August 2012.

11. **K. Linehan,** H. Doyle, Size Control Synthesis of Silicon Nanocrystals Using Cationic Surfactants, Postgraduate Research Day, Tyndall National Institute (*Poster*), July 2012.

12. **K. Linehan,** H. Doyle, Synthesis and Characterization of Size Monodisperse Silicon Nanocrystals for Nanocrystal Light-Emitting Devices, Postgraduate symposium, University of Birmingham (*Poster*), December 2011.

13. **K. Linehan,** H. Doyle, Synthesis and Characterisation of Size Monodisperse Silicon Nanocrystals for High Efficiency Light-Emitting Devices, Postgraduate Research day, Tyndall National Institute (*Poster*), July 2011.

14. **K. Linehan,** H. Doyle, INSPIRE-ICGEE 'Fabrication to Application' Summer School, Tyndall National Institute, Cork, Ireland *(Poster),* October 2010.

15. **K. Linehan,** H. Doyle, Synthesis and Characteriation of Size Monodisperse Platinum Nanospheres, Postgraduate Research Day, Tyndall National Institute, Cork, Ireland *(Poster),* October 2010.

A.4 Awards and Achievements

1. Second place BOC-Tyndall Bursary Award, 2014.

2. First Place, Audience Best Overall *Poster*, Tyndall Internal Conference, Tyndall National Institute, May 2013.

3. Third Place, Tyndall National Institute Postgraduate Research Day (*Poster*), July 2012.

4. Third Place, Tyndall National Institute Postgraduate Research Day (*Poster*), July 2011.